# Feasibility of in-beam MR imaging for actively scanned proton beam therapy

D i s s e r t a t i o n s s c h r i f t

zur Erlangung des akademischen Grades

Doktor der Medizintechnologie

Doctor rerum medicinalium (Dr. rer. medic.)

vorgelegt

der Medizinischen Fakultät Carl Gustav Carus

der Technischen Universität Dresden

von

## Sebastian Thomas Gantz

aus Dresden

Dresden 2022

1. Gutachter:    Prof. Dr. Wolfgang Enghardt

2. Gutachter:    PD Dr. Volker Hietschold


Tag der mündlichen Prüfung:                    01.02.2022


gez.: . . . . . . . . . . . . . . . . . . . . . . . . . . . . . . . . . . .
Prof. Dr. Christian Richter
Vorsitzender der Promotionskommission

# Contents

# List of Figures

# List of Tables

# List of Abbreviations

| | |
|---|---|
| **3D** | Three-dimensional |
| **ACR** | American College of Radiology |
| **Angio** | Angiography |
| **BEV** | Beam's eye view |
| **bSSFP** | Balanced steady-state free precession |
| **CNR** | Contrast-to-noise ratio |
| **CT** | Computed tomography |
| **DSV** | Diameter spherical volume |
| **FA** | Flip angle |
| **FBL** | Horizonal fixed beamline |
| **FE** | Frequency-encoding |
| **FOV** | Field-of-view |
| **FWHM** | Full width at half maximum |
| **GE** | Gradient echo |
| **GTR** | Gantry based treatment room beamline |
| **HDPE** | High density polyethylene |
| **MRI** | Magnetic resonance imaging |
| **MRiPT** | Magnetic resonance imaging integrated proton therapy |
| **MU** | Monitor unit |
| **NMR** | Nuclear magnetic resonance |
| **PBS** | Pencil beam scanning |
| **PE** | Phase-encoding |
| **pk-pk** | Peak-to-peak |
| **PMMA** | Polymethyl methacrylate |
| **ppm** | Parts-per-million |
| **PT** | Proton therapy |
| **PVC** | Polyvinyl chloride |
| **QA** | Quality assurance |
| **RF** | Radiofrequency |
| **SE** | Spin echo |
| **SNR** | Signal-to-noise ratio |
| **TE** | Echo time |
| **TOF** | Time-of-flight |
| **TR** | Repetition time |
| **UPTD** | University Proton Therapy Dresden |
| **XT** | X-ray therapy |

# 1 Introduction

Cancer continues to be the second leading cause of death in the European Union, just after diseases of the circulatory system (European Commission, 2020). Next to surgery and systemic therapy, radiation therapy is among the three main modalities in cancer treatment (Barnes et al., 2016). Mostly, external beams of ionizing photon radiation are deployed to deposit a therapeutic dose to the tumor to sterilize cancer cells. The current state-of-the-art photon-based radiotherapy (XT) is approaching the physical limits of shaping high doses to the tumor volume (Baumann et al., 2016). However, unavoidably, surrounding healthy tissue is also irradiated. In order to reduce the radiation exposure to healthy normal tissue surrounding the tumor and thereby reduce treatment side effects in normal tissue, proton therapy (PT) is an emerging alternative, potentially superior treatment option for a number of tumor entities (Baumann et al., 2016). The main advantage of protons is their characteristic to continuously slow down in tissue, deposit most of their energy near the end-of-range in the so-called Bragg peak and thereby sparing healthy tissue distally to the tumor (Jäkel, 2009). However, the sharp dose fall-off at the distal end of the Bragg peak makes PT very sensitive to any form of changes in the proton beam path. Such changes might result from patient setup uncertainties, changes in the patient anatomy, but also uncertainties in the actual proton beam range itself. Therefore, modern proton therapy is guided by daily imaging of the patient anatomy prior to dose delivery. However, imaging to date is achieved by orthogonal x-ray or cone-beam computed tomography directly at the treatment position or by a nearby in-room three-dimensional (3D) computed tomography (CT). All of these modalities apply additional imaging dose to the healthy tissues and lack soft-tissue contrast. These limitations could potentially be overcome by the integration of magnetic resonance imaging (MRI) into the proton treatment. In addition, this could allow for online image-based adaptation of the treatment in real-time. Despite this strong motivation, clinical hybrid systems for MRI-integrated PT (MRiPT) do not yet exist due to a number of hitherto open technological barriers and knowledge gaps. Two central aspects are the quality of beam delivery inside the complex-shaped magnetic fringe field of an MRI scanner

and the mutual magnetic interactions of both systems, which can potentially degrade both the beam and image quality (Hoffmann et al., 2020; Schippers & Lomax, 2011).

In 2017, the world's first combination of a low-field open MRI scanner with a static proton research beamline was achieved by Schellhammer et al. (2018b) as the first step towards the development of a clinical MRiPT system. Investigations on the technical feasibility have shown that, despite the proton therapy facility being an electromagnetically contaminated environment, anatomical MR imaging is feasible with an image quality sufficient for target volume definition and patient positioning and no visible beam-induced image degradation was observed in images of a tissue-mimicking phantom (Schellhammer et al., 2018b). However, this initial prototype system was installed at a static proton research beamline, only capable of delivering proton beams to a single central spot or at most a static volume spread out through a passive scattering (PS) technique using scatter-foils and ridge filters, to broaden the field in lateral and longitudinal direction, respectively. When delivered under the influence of the spatially variant main and fringe fields of the MRI scanner, such a passively scattered broad beam, also containing a broad energy spectrum, will deposit a radiation field that is severely deflected and deformed as compared to the desired radiation field in the case without the magnetic fields of the MRI scanner (Oborn et al., 2017). In contrast, state-of-the-art clinical PT uses active beam scanning by the so-called Pencil Beam Scanning (PBS) technique. To this end, a 3D radiation field is formed by a superposition of individual pencil beams. The positional variation in depth direction is achieved by variation of the proton beam energy, while for the two lateral directions the beam is magnetically steered using a pair of dipole magnets. In the case of PBS beam delivery, a per-pencil beam correction to compensate the beam deflection due to the magnetic field of the MRI scanner seems straight forward. Therefore, it is currently believed that the full integration of MRI with PT ultimately requires the MRI scanner to be operated at a PBS beamline (Hoffmann et al., 2020; Oborn et al., 2017).

Therefore, the main aim of this thesis is to investigate the feasibility of integrating an MRI scanner with an actively scanned proton beam. This is achieved by an exploratory study that focuses on quantifying the magnetic field interactions between the MRI scanner and the PT system and evaluates the effects of these interactions on MR image quality.

In preparation for such an integration of the MRI scanner with an actively scanned beam, one remaining challenge had to be investigated in more detail. The study by Schellhammer et al. (2018b) had revealed a sub-millimeter, space invariant image translation between im-

ages acquired with the static beamline magnets switched on and off. A detailed quantitative analysis of the MR image quality during simultaneous static irradiation was lacking so far. Such a study could confirm that the position of scanned objects in the MR images is subject to variations caused by the operation of the proton beamline (Gantz et al., 2021; Schellhammer, 2019). These image shifts were hypothesized to be the result of a change in the resonance frequency of the MRI scanner caused by the overlapping static magnetic fringe fields produced by the beamline magnets. In order to test this hypothesis and to unravel the magnetic field interactions between the MRI scanner and the PT system, a comprehensive magnetometric characterization of all magnetic influences from the PT system onto the MRI scanner was conducted in **Chapter 3**.

In the following, the feasibility of combining an MRI scanner with an actively scanned proton beam is investigated. In **Chapter 4**, such a combination, bringing the low-field open MRI scanner to a horizontal beamline with a dedicated PBS nozzle is presented. Here, the focus of the investigation is to create all the conditions to safely operate both the PBS beamline under the influence of the MRI scanner and vice versa. Therefore, due to radiation protection regulations, the beamline requires a fixed-position beam-stopper, i.e., a water tank large enough to stop the proton beam emitted from the PBS beamline in both cases with and without the MRI scanner at the beamline. To achieve this, the radiation field size at the proximal plane of the beam-stopper is determined by film measurements both with and without the MRI scanner at the beamline in order to verify the suitability and correct positioning of the beam-stopper. Additionally, the maximum applicable radiation field size inside the MRI scanner that allows irradiation of target objects without directly irradiating any component of the MRI scanner is theoretically determined and confirmed by measurement.

With these prerequisites achieved, **Chapter 5** focuses on studying the feasibility of simultaneous MR imaging and proton PBS irradiation. The operation of the PBS beamline is hypothesized to result in an interference of the dynamic magnetic fringe fields of the PBS beamline and scanning magnets with the static magnetic field ($B_0$) of the MRI scanner and thus potentially result in a loss of image quality during simultaneous imaging and irradiation. To test this hypothesis, firstly, a detailed magnetometry study is performed to assess the magnetic interactions of the fringe fields of the PT system, especially those produced by the beamline and scanning magnets of the PBS beamline onto the magnetic field of the MRI scanner. Secondly, the image quality of MR images which are acquired during simul-

taneous proton PBS irradiation is studied. To this end, the radiation field is decomposed into the three main axes to independently study the effects due to operation of the beamline magnets as well as the two scanning magnets. Finally, a theoretical description of the effects of dynamic changes of the $B_0$ field onto the MRI signal acquisition in $k$-space is presented. This theory is then utilized to reproduce the experimentally observed ghosting artefacts, demonstrating their origin.

Furthermore, the concept of MRiPT, operating an MRI scanner at the isocenter of a proton beamline, offers a unique possibility to potentially overcome one of the key challenges of proton therapy: the uncertainty in the proton beam range, which currently still limits the precision of the PT treatment. To reduce this uncertainty, currently, the verification of the proton range is mostly based on the detection of secondary radiation such as prompt gamma rays (Knopf & Lomax, 2013; Parodi & Polf, 2018) or ionoacoustic waves (Kellnberger et al., 2016; Takayanagi et al., 2020). However, none of these methods is capable of visualizing both the proton beam end-of-range and the patient anatomy. Therefore, investigating the possibility of online proton beam visualization using MR imaging seems desirable. In fact, a first exploratory study (Schellhammer, 2019) could show an MRI-detectable "signature" of effective dose delivery in a fluid-filled phantom which could potentially serve as a novel method for 3D beam range assessment and dose verification. However, the observed "signature" has only been described phenomenologically to date and the effect could not be reproduced in viscous or solid media. Therefore, in **Chapter 6** the hypothesis is tested that the observed proton beam-induced MRI-detectable signature is caused by buoyancy driven convection. This is achieved by utilizing an optimized MRI sequence and two independent experiments: Firstly, using a dedicated flow-restriction phantom that selectively allows and inhibits fluid flow and secondly, by introducing an external flow condition, to test if the beam-induced MRI-detectable signature can be explained by fluid flow.

In preparation to these investigations, **Chapter 2** introduces the basic principles of proton therapy, MR imaging and magnetometry for MRI systems. In the general discussion (**Chapter 7**) the advances in knowledge achieved by this thesis are discussed and implications for further studies are given, which are necessary to bring the concept of MRiPT closer towards a clinical application. Finally, the work is summarized in both English and German language in **Chapter 8** and **Chapter 9**, respectively.

# 2 Theoretical background

This chapter aims to provide a short overview of the physical principles underlying the topics covered within this thesis. The chapter starts by introducing proton therapy as a concept in radiation oncology, turns to a brief introduction of the main principles underlying the imaging process of an MRI scanner and finally covers the principles of magnetometry for MRI systems.

## 2.1 Proton therapy

### 2.1.1 Physical principle

As an alternative to classical photon based radiation therapy, patient irradiation using protons was first proposed in 1946 by physicist Robert R. Wilson and first attempts at patient irradiation soon followed in the 1950s. For radiotherapeuthic applications, proton beams with kinetic energies of up to 250 MeV are being used. For an individual proton, along the direction $x$ it travels, the rate at which it loses kinetic energy $E$ is defined as the stopping power $S$:

$$S \equiv -\frac{\mathrm{d}E}{\mathrm{d}x}.\tag{2.1}$$

As $S$ strongly depends on the stopping material, it is convenient to define the mass stopping power $S_\rho$ as stopping power $S$ corrected for the local density $\rho$ of the stopping medium:

$$S_\rho \equiv \frac{S}{\rho} = -\frac{1}{\rho}\frac{\mathrm{d}E}{\mathrm{d}x}.\tag{2.2}$$

When traversing a patient or material in the beam path, the protons mainly interact by three distinct processes: Coulomb interactions with electrons, elastic Coulomb scattering on nuclei, and inelastic nuclear interactions.

**Coulomb interactions with electrons**   Most of the energy of the protons is transferred by multiple inelastic Coulomb interactions between the proton and the electrons in the target. The collision stopping power $S_{\mathrm{col}}$ (which is the main contributor to $S_\rho$) for protons can be described by the Bethe-Bloch equation (Bloch, 1933):

$$S_{\mathrm{col}} = -\left(\frac{\mathrm{d}E}{\mathrm{d}x}\right)_{\mathrm{col}} = \frac{e^4}{4\pi\epsilon_0^2 m_e c^2} \cdot n_e \cdot \frac{1}{\beta^2}\left[\ln\left(\frac{T_{\max}}{I}\right) - \beta^2\right], \tag{2.3}$$

where $c$ is the speed of light, $\epsilon_0$ is the vacuum permittivity, $\beta \equiv v/c$, with $v$ the velocity of the proton, $m_e$ and $e$ are the mass and charge of the electron, respectively. Furthermore, $I$ is the mean excitation energy of the target material and $n_e = \frac{Z\rho}{Au}$ is the electron density (with the density $\rho$, charge number $Z$ and mass number $A$ of the nuclei and the atomic mass $u$) of the target material and

$$T_{\max} = \frac{2m_e c^2 \beta^2}{1 - \beta^2}$$

is the maximum kinetic energy transfer in a single collision with a free electron. Thus, $n_e$ and $I$ are the material-dependent parameters in Equation 2.3.

The product of the stopping power and the fluence $\Phi \equiv \frac{\mathrm{d}N}{\mathrm{d}A}$ (number of protons $\mathrm{d}N$ per unit area $\mathrm{d}A$) describes the total energy loss of the proton beam per unit mass and is therefore closely related to the physical dose $D = \frac{\mathrm{d}E'}{\mathrm{d}m}$ (with $E'$ being the absorbed energy), which is the most prevalent physical quantity in radiation therapy. However, it is not necessarily the same. The energy $E$ lost by a proton beam exceeds the energy $E'$ absorbed locally by a medium, as a fraction of the beam's energy is transferred to neutral secondaries (photons and neutrons) or high energetic secondary electrons ($\delta$-rays) (Paganetti, 2011). The dose is known to correlate with cell death and tumor control (Holthusen, 1936), and therefore commonly used to generate and evaluate treatment plans in radiotherapy. The main depth-dependence in the Bethe-Bloch equation is the $\frac{1}{\beta^2}$ term, indicating that protons lose more energy in a collision the longer they interact with the electron. The rate of energy loss therefore increases as the protons slow down.

**Scattering and nuclear interactions**   A primary proton may scatter both elastically and non-elastically off a material nucleus. Elastic scattering is described as the interaction of a proton with the Coulomb field of an atomic nucleus which leads to the proton being deflected from its initial direction. The mean deflection in a single collision is very small.

Scattering is described by Molière's multiple Coulomb scattering theory which predicts the spatial distribution to be nearly Gaussian and the scattering angle to depend mainly on the target materials atomic number $Z$ (Moliere, 1947). This results in both a broadening of the proton beam and a fluctuation in the range as projected on the initial beam direction, as each scattered proton will follow a different path. Additionally, the number of interactions between the proton and the material, as well as the amount of energy transferred in a single collision are subject to a stochastical fluctuation. This results in a broadening of the Bragg peak which scales with initial proton beam energy, to about 1 % of the proton range (Paganetti, 2011).

Besides elastic scattering, infrequently, protons will also interact non-elastically with a nucleus and produce uncharged particles (neutrons and $\gamma$-rays), charged fragments (such as secondary protons and $\alpha$-particles), as well as excited and radioactive nuclei. However, these secondaries tend to have much lower energies and larger angles than the primary protons and thus their dose contributions are orders of magnitude smaller than those of the primary particles (Paganetti, 2011). Therefore, the effect of nuclear interactions is merely a reduction in primary proton fluence, which may occur at any proton energy (and therefore depth) and is the primary source of fluence loss before the end-of-range. Although these processes do not significantly influence the proton dose deposition, they become of interest in radiotherapy for two reasons. Firstly, especially for metal objects in the beam path, radioactivation may become relevant for radiation protection (Faßbender et al., 1997) and secondly, because the emission of prompt gamma-rays is under research to be used for quality assurance, i.e. to verify the proton range in the patient (Verburg & Seco, 2014).

**The Bragg peak, range and range-energy relation**   The combination of the three interactions (stopping, scattering and nuclear interactions) determines the shape of the typical depth-dose curve, featuring the Bragg peak at the end-of-range (see Figure 2.1). The range $R_0$, also called mean projected range of a proton beam, is defined by the depth at which half of the initial protons have stopped, i.e. at which the fluence drops to 50 %. However, in measurements this quantity is often hard to obtain, as mainly dose is measured. Therefore the range $R_0$ is correspondingly defined as $R_0 \equiv R_{80}$, where $R_{80}$ is the depth at the distal 80 % point of the peak.

For a proton beam stopping in a homogeneous material, the range $R_0$ is determined by the protons initial energy $E_0$ and can be calculated using the continous-slowing-down
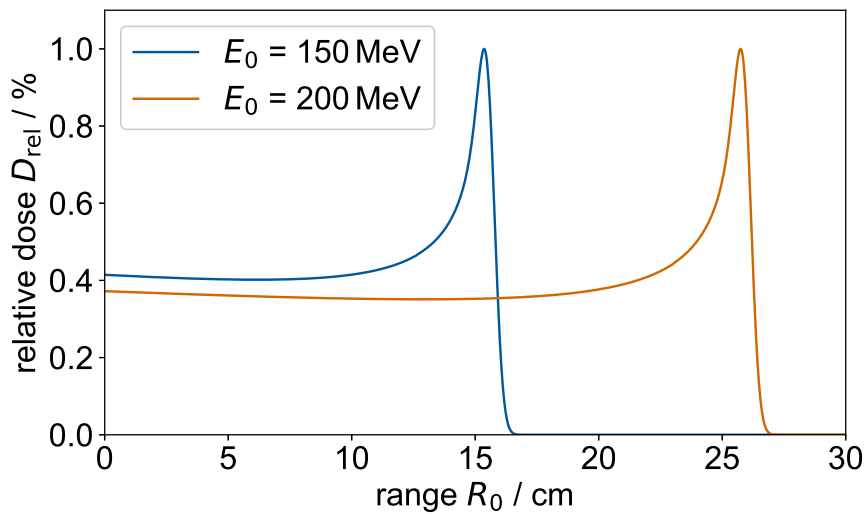
**Figure 2.1:** Analytical approximation of the relative dose $D_{\mathrm{rel}}$ as a function of penetration depth $R_0$ for two proton beams of 150 MeV and 200 MeV in water (Bortfeld, 1997).

approximation:

$$R_0(E_0) = -\int_{E_0}^{0} \frac{1}{S(E')\mathrm{d}E'}. \tag{2.4}$$

For practical use, these ranges are tabulated as a function of energy (Seltzer & Bergstrom, 1993) or can be determined using analytical approximations (Bortfeld, 1997) for range estimation.

### 2.1.2 Beam delivery

To be able to treat patients with proton therapy, protons have to be accelerated and subsequently guided to the patient. The general concepts of this production and beam delivery process are outlined in the following.

**Proton beam acceleration and energy selection** For radiation therapy, proton beams are typically generated by either a cyclotron or a synchrotron (Schippers, 2009). The most commonly used systems are isochronous cyclotrons which consist of mainly four components: a proton source, a radiofrequency (RF) generator system, a strong magnet and a beam extraction unit. In the proton source in the center of the cyclotron a hydrogen gas is ionized and the protons are extracted. The RF generator drives an oscillating voltage at

the electrodes providing a strong electric field which accelerates the protons between the electrode plates. The RF frequency equals a multiple of the orbital frequency of the protons and is typically on the order of $50\,\text{MHz} - 100\,\text{MHz}$. The strong magnet is utilized to confine the proton trajectories to a spiral-shaped orbit, that allows them to be repeatedly accelerated by the RF voltage between the electrodes. The magnetic flux density, which is typically on the order of $2\,\text{T}$ to $4\,\text{T}$, increases from the center of the magnet with increasing radius to account for relativistic effects. Thus, the time required for one revolution in the isochronous cyclotron is independent from the proton velocity, which allows for quasi-continuous beam extraction. Finally, the extraction system guides the particles that have reached their maximum energy, typically $230\,\text{MeV}$ to $250\,\text{MeV}$, out of the cyclotron into a beam-transport system. The cyclotron thus produces a proton beam of a constant energy. For treatment application, the proton beam is then decelerated to the requested energy by the use of a degrader, such as a graphite wedge and a subsequent arrangement of dipole magnets to reduce the energy spread (Bercher et al., 2001).

**Beamline and gantry**   From the cyclotron and energy selection system, the proton beam is guided towards the treatment room by a beamline, which mainly consists of an evacuated tube and several quadrupole and dipole magnets, which focus and redirect the beam, respectively. Typical maximum flux densities of the two magnet types are $0.5\,\text{T}$ and $2\,\text{T}$, respectively and are adjusted depending on the energy of the proton beam transported. The beam can either be directly delivered to the patient in a horizontal fixed beamline configuration or it is directed through a gantry, which allows patient irradiation from multiple different directions, without the need to move the patient couch. The gantry is a large rotatable ferromagnetic construction including several magnets to bend the beam trajectories towards the patient. Today, most proton therapy centers offer atleast one gantry based beamline (PTCOG, 2018).

**Field formation: Active and passive beam delivery**   In order to conform the proton beam dose distribution to the target, the proton beam has to be modulated to deliver a uniform dose to the target volume. To achieve this, two principle techniques are regularly used in proton therapy, passive scattering and active beam scanning.

During passive scattering one or more (typically two) scatterers are used to create a large uniform beam field, which is then adjusted to the tumor cross-section by either individually

designed solid brass or multileaf collimators. Different proton beam ranges are created by a rotating modulator wheel or a ridge filter placed in the beam path. Finally, to tailor the range of the beam to the distal end of the tumor individually manufactured compensators are used (Engelsman et al., 2009).

Alternatively, active PBS is utilized. For this technique, the target volume is divided into slices of equal proton beam energy. Each of these slices is irradiated by a beam of corresponding energy, while the beam is laterally deflected by a set of two dipole magnets. This way, typically starting from highest to lowest energy required, the whole target volume is scanned. The scanning time depends on the particular system but is typically on the order of tens to hundreds of milliseconds per scanned line and hundreds of milliseconds to a few seconds per slice while changing the beam energy takes about one to two seconds (Seco et al., 2009; Shen et al., 2017). Ionization chambers are used for on-line feedback of the beam fluence and position. PBS beam delivery does not require patient-specific hardware, allows the delivery of highly inhomogeneous dose distributions and enables improved proximal normal tissue sparing as compared to passive scattering (Engelsman et al., 2013). However, due to the spatio-temporal dependent irradiation, active scanning is very sensitive to organ motion (James et al., 2018).

## 2.2 Magnetic resonance imaging

In this section a brief introduction to the fundamentals of the process of MR image formation will be given, focusing on the central aspects which are important for the experiments and results of this thesis. For a more detailed and complete overview, the reader is referred to the literate, e.g. Haacke et al. (1999).

### 2.2.1 Physical principle of MRI

The fundamental property used for imaging in an MR imaging experiment is the nuclear magnetic momentum arising from the nuclear spin of atoms. Most applications of MR imaging focus on protons, which have the spin quantum number $I = 1/2$. When exposed to an external magnetic field, such as the static magnetic field $\mathbf{B_0} = B_0\mathbf{e_z}$ of an MRI scanner, which is typically on the order of 0.2 T to 7 T (Lipton, 2008), due to the Zeeman effect the nuclear magnetic moment of the proton splits into two energy states, parallel $N^+$ and

antiparallel $N^-$ orientation to the field. The energy separation $\Delta E$ reads as follows

$$\Delta E = \hbar\omega_0 = \gamma\hbar B_0, \tag{2.5}$$

where $\hbar$ is the reduced Planck's constant, $\gamma/2\pi$ = 42.6 MHz/T is the gyromagnetic ratio for protons and $\omega_0$ is the Larmor frequency. To change state between the two energy levels, the proton magnetic moment has to either absorb or emit a photon with the exact Larmor frequency. The distribution of the energy states $N^+$ and $N^-$ in an ensemble of spins depends on the energy separation and the temperature and is given by the Boltzmann-distribution (Keeler, 2010)

$$\frac{N^+}{N^-} = \exp^{-\Delta E/(k_{\mathrm{B}}T)}, \tag{2.6}$$

where $k_{\mathrm{B}}$ = 1.381·10$^{-23}$ J/K is the Boltzmann constant. For a $B_0$ field of 1 T and body temperature, the Boltzmann distribution shows that the two states are almost equally distributed, with only a very small excess on the order of $10^{-6}$. Nevertheless, this excess results in a net-magnetization $\mathbf{M_0} = M_0\mathbf{e_z}$, the vector sum of the magnetic moments, that is parallel to the external magnetic field.

The signal in MRI is obtained by modulating this equilibrium magnetization $\mathbf{M_0}$ by applying a short RF pulse $\mathbf{B_1}(t)$ which rotates around $\mathbf{B_0}$ with exactly the Larmor frequency $\omega_0$ and thus induces a torque on $\mathbf{M_0}$ (Bloch, 1946). Consequently, the magnetization is tipped away from the $z$-axis into the $xy$-plane. This magnetization $M_{xy}$, which rotates around the $z$-axis emits an electromagnetic signal $S \propto M_{xy}e^{i\omega t}$ which can be detected in a receiver coil by induction. Subsequently, the magnetization will return to the equilibrium by two distinct processes, $T_1$- and $T_2$- relaxation, which can be described by the Bloch equations (Bloch, 1946):

$$\frac{\mathrm{d}M_z}{\mathrm{d}t} = -\frac{M_z - M_0}{T_1} \tag{2.7}$$

and

$$\frac{\mathrm{d}M_{xy}}{\mathrm{d}t} = -\frac{M_{xy}}{T_2}. \tag{2.8}$$

$T_1$-relaxation is the process of the magnetization returning to the $z$ axis and is often called spin-lattice or longitudinal relaxation in MRI. Additionally, the transversal magnetization $M_{xy}$ de-phases due to local magnetic field inhomogeneities on the micro- and nanoscales and thus variations in the Larmor frequency. This process is called $T_2$ lateral relaxation or spin-

spin relaxation and is characterized by the time constant $T_2$ which is typically smaller then $T_1$ (Bloch, 1946).

## 2.2.2 Spatial encoding

To obtain an image, information on the distribution of the magnetization is required. This is achieved by applying additional gradient fields, which alter the frequency and phase of the MRI signal. In general, three different concepts are utilized, slice excitation, frequency-encoding (FE) and phase-encoding (PE). Adding a linear gradient $G_x$ in one direction results in a position-dependent field $\mathbf{B}(x, y, z) = \mathbf{B_0} + G_x \mathbf{e_x}$ and subsequently a position-dependent Larmor frequency along the direction of the gradient

$$\omega_0(x) = \gamma(B_0 + x \cdot G_x).$$ (2.9)

Modern clinical MRI scanners are equipped with gradient systems capable of generating field gradients of 40 mT/m with switching rates up to 200 T/ms (Hidalgo-Tobon, 2010). For image encoding only the non-constant part in Equation 2.9 is of interest, thus the frequency offset is $\Delta\omega = \gamma G_x x$. Generalizing the gradient to a vector $\mathbf{G} = G_x \mathbf{e_x} + G_y \mathbf{e_y} + G_z \mathbf{e_z}$ gives a general expression for the frequency and phase of the detected MRI signal:

$$\Delta\omega = \gamma \mathbf{G}(t) \cdot \mathbf{r}$$ (2.10)

and

$$\Delta\phi(\tau) = \int_0^\tau \Delta\omega(t)dt = \gamma \int_0^\tau \mathbf{G}(t) \cdot \mathbf{r}dt.$$ (2.11)

Slice-excitation refers to the process of applying a field gradient ($G_z$) during $\mathbf{B_1}$ excitation. When the $\mathbf{B_1}$ field has a bandwidth $\Delta\omega_{RF}$ a slice of thickness $z_{\text{slice}} = \omega_{RF}/\gamma G_z$ is excited. Therefore, the signal obtained is determined by the sum of the magnetization along the $z$-direction

$$M_{xy}^{\text{slice}}(x, y) = \int_{-z_{\text{slice}}/2}^{z_{\text{slice}}/2} M_{xy}(\mathbf{r})\mathrm{d}z.$$ (2.12)

Applying a gradient in $x$-direction during signal acquisition (often called read-out) results in a signal with a bandwidth of frequencies. Performing a Fourier transform of the signal along the $x$-direction of the gradient allows to decompose the position depend contributions. This process is called frequency encoding and the respective gradient is called frequency-

encode or read-out gradient. The remaining image dimension $y$ is then encoded by applying an additional gradient $G_y$ for a short amount of time. This gradient results in an temporary $y$ position-dependent change in the Larmor frequency and thus an accumulation of phase. After the gradient is turned off, the Larmor frequency of all spins is restored, however the relative difference in phases remains dependent on the $y$ position. This process is called phase-encoding.

Using these three encoding principles and Equations 2.10, 2.11 and 2.12, the signal can be expressed as

$$
\begin{aligned}
S(\mathbf{r}, t) &\propto \iiint_{FOV} M_{xy}(\mathbf{r}) e^{-i(\omega(\mathbf{r})t + \phi(\mathbf{r}))} dx\,dy\,dz = e^{-i\omega_0 t} \iiint_{FOV} M_{xy}(\mathbf{r}) e^{i\gamma \int_0^t \mathbf{G}(t') \cdot \mathbf{r}\, dt'} dx\,dy\,dz \\
&= e^{-i\omega_0 t} \int_x \int_y M_{xy}^{\text{slice}}(x, y) e^{i\gamma(xk_x + yk_y)} dx\,dy,
\end{aligned}
$$

(2.13)

where $k_i = \int_0^t G_i dt'$ with $i = x, y$ are the $x$ and $y$ components of the function $K(k_x, k_y)$, called the $k$-space, which is the 2D Fourier-transform of the magnetization $M_{xy}^{\text{slice}}$. The conventional principle to sample $k$-space is to acquire the time-resolved signal during the application of $G_x$ and repeating this acquisition after a certain time called the repetition time (TR), for different phase-encoding gradient amplitudes $G_y$, see Figure 2.2.

### 2.2.3 Basic pulse sequences

The two most common and basic MRI pulse sequences, spin echo and gradient echo will be presented in this section.

**Spin echo**  The idea of the spin echo (SE) sequence is to counterbalance the additional spin de-phasing which is caused by machine- and patient-specific inhomogeneities, such as e.g. gradient non-linearity (Haacke et al., 1999). Theses inhomogeneities introduce an additional relaxation $T_2'$ which results in an effective relaxation time $T_2^*$ that is smaller then $T_2$ ($1/T_2^* = 1/T_2 + 1/T_2'$). To prevent this, an additional $180°$ RF pulse is applied after half of the echo-time (TE) to invert the transverse magnetization. After the pulse, the dephasing caused by the machine- and patient-specific inhomogeneities is gradually restored. At time TE, when the gradient contributions of the read-out gradient $G_x$ is the same as before the $180°$ pulse (indicated by the area a in Figure 2.2a), both contributions rephase at the same time, forming a signal maximum, the spin echo which depends on $T_2$ rather then $T_2^*$ .
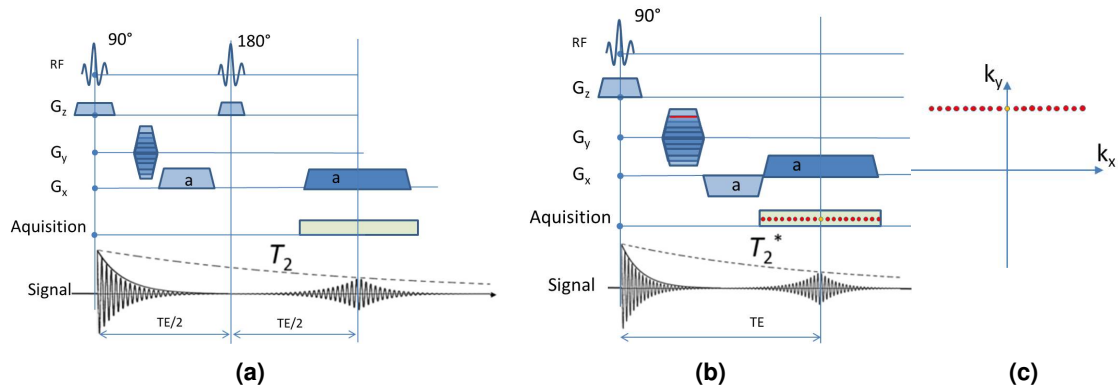
**Figure 2.2:** Sequence diagrams for a spin echo (a) and a gradient echo (b) pulse sequence. The gradients $G_x$, $G_y$ and $G_z$ are used for frequency-encoding, phase-encoding and slice selection, respectively. For the gradient echo, the line of $k$-space which is filled for one repetition of the pulse sequence is shown in (c), corresponding to the red line and spots that indicate the chosen PE level and the individual FE signal acquisitions, respectively.

**Gradient echo**   In gradient echo imaging (GE), the signal echo, instead of being generated by a 180° pulse, is realized by inverting the read-out gradient. Thus, an echo is formed when the two contributions cancel each other, indicated by the area a in Figure 2.2b. As opposed to spin echo, the gradient-echo does not counterbalance the machine and patient specific inhomogeneities and thus the signal depends on $T_2^*$. However, using a gradient-echo sequence, a shorter TE can be realized as less gradient operations have to be implemented and gradient slew rate is one typical limitation for short TE sequences (Hidalgo-Tobon, 2010; Reeder & McVeigh, 1994). Furthermore, gradient echo imaging is typically performed with lower flip angles (FA), which allows to decrease the TR which reduces the imaging time (Bernstein et al., 2004).

## 2.3  Magnetometry for MRI systems

A variety of methods exist to measure and characterize magnetic fields. For the use in MRI systems, mainly two techniques are used: Nuclear magnetic resonance (NMR) and Hall-probe devices.

**Nuclear magnetic resonance**   Nuclear magnetic resonance is the gold standard for magnetic field measurement (Keller, 2007). The general measurement principle is based on the identical phenomenon as MR imaging without spatial encoding. NMR Teslameters mea-

sure the Larmor frequency and therefore the norm of the magnetic flux density (Equation 2.5) with an accuracy of up to 10 nT (Zanche et al., 2008) and do not suffer from drift or temperature dependence. However, some limitations have to be considered when using NMR based devices for MRI system magnetometry. Firstly, the application is limited to uniform fields, as in inhomogeneous fields, a distribution of Larmor frequencies would be measured, resulting in a loss of accuracy. Secondly, the NMR measurement can only be applied for static or slowly changing fields, as the minimum measurement time is typically on the order of hundreds of milliseconds to a few seconds (Keller, 2011; Zanche et al., 2008). Thirdly, measuring low magnetic fields requires the use of larger samples, as the resonance diminishes with lower energy separation.

**Hall probe**    Hall probe devices use the Hall effect, which is the result of the Lorentz force $\mathbf{F}$ on charge ($q$) carriers moving with velocity ($\mathbf{v}$) in the presence of a magnetic field ($\mathbf{B}$)

$$\mathbf{F} = q\mathbf{v} \times \mathbf{B}. \tag{2.14}$$

The force results is an accumulation of charge carriers, leading to a steady state voltage $V_{\mathrm{Hall}}$ perpendicular to the current $I$ and magnetic field. The resulting voltage difference is linearly proportional to the applied current $I$ and the field component $B_\perp$ normal to the probes plane

$$V_{\mathrm{Hall}} \propto I \cdot B_\perp. \tag{2.15}$$

The measured voltage $V_{\mathrm{Hall}}$ is transferred into field reading using a linear calibration curve $B(V_{\mathrm{Hall}})$. As Hall probes measure individual $\mathbf{B}$ field components, in practical applications often three probes are combined in one device to access the field vector $\mathbf{B}$.

# 3 Magnetometry of the in-beam MRI scanner at the static research beamline

Schellhammer et al. (2018b) has previously described the combination of an open low-field MRI scanner with a static proton research beamline and has shown its technical feasibility (Schellhammer, 2019). Furthermore, a quantitative analysis of image quality during simultaneous irradiation was performed by S. Schellhammer and myself (Gantz et al., 2021; Schellhammer, 2019), showing that in-beam MR imaging is feasible, with mainly two effects of simultaneous irradiation on image quality. Firstly, a minor reduction in signal-to-noise ratio (SNR) (1 % − 6 %) was observed and secondly, an apparent image translation (0.1 mm − 0.7 mm) was found in frequency-encoding direction, which was dependent on the read-out gradient of the pulse sequence (Figure 3.1). This image shift was hypothesized to correspond to the changes in MRI resonance frequency due to the fringe fields of the proton beamline magnets being energized.



(a)  (b)  (c)
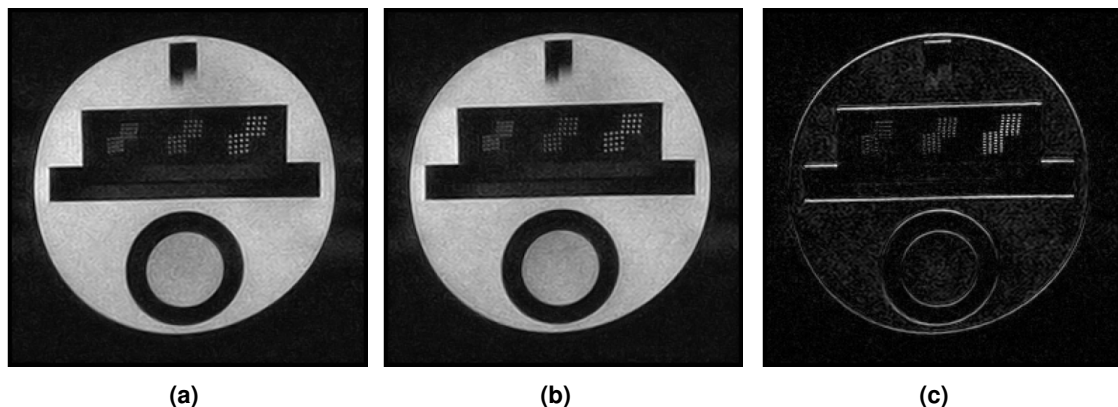
**Figure 3.1:** Example for the observed image shift along the vertical (frequency-encoding) direction between two $T_2^*$-weighted GE images in slice 1 of the ACR Small Phantom. (a) During irradiation using 125 MeV and 5.4 nA, (b) with all beamlines off and (c) difference image showing the 0.7 mm vertical shift between the two images.

These results indicate the necessity of a comprehensive magnetometry study of the combined MRI & PT system to evaluate all internal and external influences on the static magnetic field of the MRI scanner, such as changes induced by ambient temperature variation, operation of either of the two operational beamlines (at the time of this study, the PBS beamline, which is the third beamline at University Proton Therapy Dresden (UPTD), was still under construction) and the clinical gantry. Such a magnetometric analysis of the combined system will allow to test the hypothesis raised by Schellhammer (2019) whether the measured $B_0$ field changes can justify the observed image translations and provide a full overview of external magnetic sources to be monitored for any further studies using the presented combined MR-PT system. Parts of this chapter have been published in Gantz et al. (2021).

## 3.1 Material and methods

### 3.1.1 Measurement setup

Experiments were conducted in the research room of the UPTD facility. The facility hosts an isochronous cyclotron (C230, Ion Beam Applications SA, Louvainla-Neuve, Belgium) with three beamlines operated in two vaults, see Figure 3.2. Firstly, the clinical treatment room with the gantry-based beamline (GTR) and secondly, the research room that offers a horizontal fixed proton research beamline (FBL). The third beamline depicted in Figure 3.2, an active horizontal PBS beamline, was still under construction during the experiments performed in this chapter, but will be relevant for the investigations in Chapter 4 and 5.

Throughout this chapter, the exact same setup as reported in Schellhammer et al. (2018b) and Schellhammer (2019) was used. The C-shaped open MRI scanner based on a 0.22 T permanent magnet utilized a vertically upwards directed $B_0$ field. The MRI scanner is placed on a movable trolley system which incorporates an RF cage built from copper-laminated plywood panels. The MRI scanner was positioned in front of the fixed horizontal proton research beamline, with its magnetic isocenter aligned with the nominal beam-isocenter. In the lateral direction, the MRI scanner was positioned with a displacement of 2 cm to the right in beams eye view (BEV), to compensate for the beam deflection and assure that a 125 MeV proton beam would centrally impinge on a phantom placed at the magnetic isocenter of the MRI scanner (i.e. the center of the field-of-view (FOV) of the MRI
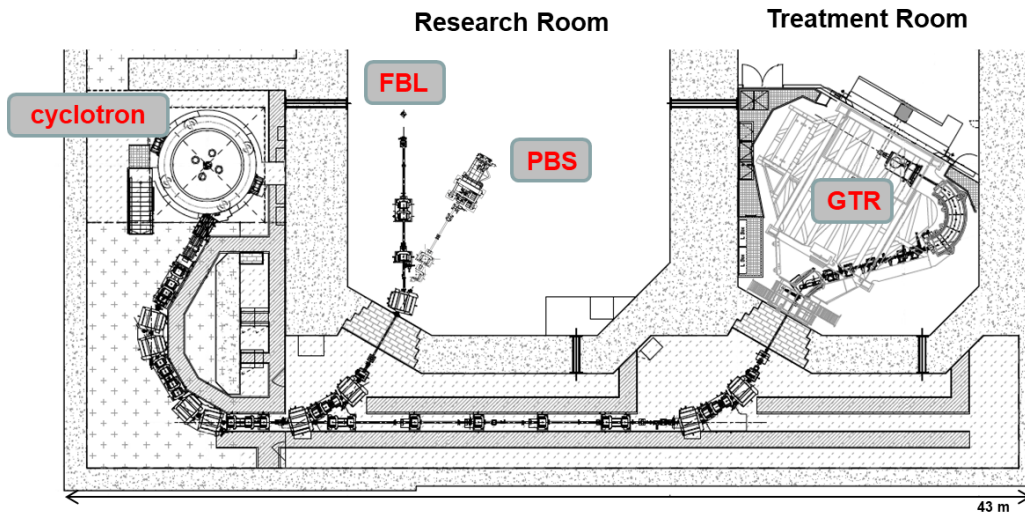
**Figure 3.2:** Overview of the UPTD proton therapy facility comprising the cyclotron, the research room with a horizontal static research beamline (FBL) and the treatment room with a rotating gantry (GTR). The second beamline in the research room, a horizontal beamline with a dedicated pencil beam scanning nozzle (PBS) was still under construction during the experiments discussed in this chapter.

scanner) (Schellhammer, 2019). The distance to the beam-exit window, last pair of focusing quadrupole magnets and 30° bending dipole magnet were 1.1 m, 2.8 m and 7.1 m stream upwards from the magnetic isocenter of the MRI scanner, respectively.

### 3.1.2 Magnetic field camera

The static magnetic field around the magnetic isocenter of the MRI scanner was mapped using a half-moon shaped magnetic field camera (MFC 3048, MetroLab, Geneva, Switzerland) containing 16 NMR probes evenly distributed along the arc of the half circle (Figure 3.3). Each probe measured the resonance frequency at a specific location. The probe array was vertically mounted on a manually rotatable holder with its origin aligned with the magnetic isocenter of the MRI scanner. The probe array was either directed towards the beam exit window at a fixed azimuthal angle of $\varphi$ = 180° or manually rotated over 360° along its vertical axis (i.e. parallel to the $B_0$ field lines) at 12 equidistant azimuthal angles of 30° each. In the former case, in total 16 samples were acquired on the arc with a radius of 11 cm, whereas in the latter case, for a full rotation, in total 16 × 12 samples were acquired on the surface of a 22 cm diameter-spherical volume (DSV). From this data, both the central resonance frequency ($f_n$), which was the average frequency over all $n$ samples, and
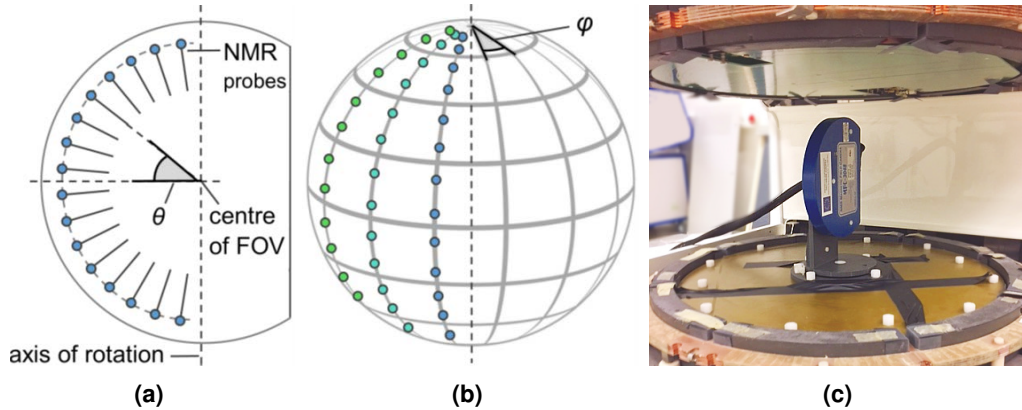
**Figure 3.3:** (a) Schematic representation of the half-moon shaped magnetic field camera with 16 individual NMR probes, distributed along the polar angle $\theta$. (b) Schematic representation of the measurement locations of a 16 × 12 samples $B_0$ field map on the surface of a 22 cm diameter spherical volume. The azimuthal angle $\varphi$ denotes the camera position ($\varphi = 0°$ when the camera is looking away from the beam exit window). (c) Setup of the camera at the magnetic isocenter of the MRI scanner. Figure reprinted from Gantz et al. (2021).

the peak-to-peak (pk-pk) frequency variation relative to the central resonance frequency to indicate the magnetic field homogeneity ($\mathrm{MFH}_n = \frac{f_{max} - f_{min}}{f_n}$) were calculated. The pk-pk MFH is reported in parts-per-million (ppm) as is common practice for $B_0$ field mapping in MRI.

### 3.1.3 Magnetic field drift

The MRI scanner used in this study is based on permanent magnets made of $Nd_2Fe_{14}B$ material which is known to be very sensitive to temperature fluctuations (Stapf & Han, 2005). The temperature coefficient of the residual magnetic flux density of $Nd_2Fe_{14}B$ is about -1100 ppm·K$^{-1}$ (Hitachi, 2019). To compensate for thermal drift effects of the $B_0$ field, the magnets and the flux returning steel yoke are temperature controlled at 36.0 °C. The temperature stability, as measured by the internal temperature sensors of the MRI scanner, is better than 0.3 mK. However, this measure provides no information on the temperature distribution over the whole volume of the magnet and given the very low thermal conductivity of the $Nd_2Fe_{14}B$ of 7-8 W·(m·K)$^{-1}$ (Hitachi, 2019), the $B_0$ field strength and homogeneity of the MRI scanner are expected to exhibit a residual drift due to environmental temperature fluctuations (Kose & Haishi, 2011). To evaluate the magnitude and rate of this drift, long-term measurements over 4 days, with a 2-hour break during the second day for reference rotation measurements (see below) were performed with the magnetic field cam-

era positioned at a fixed azimuthal angle of $\varphi = 180°$ and a sampling rate of 0.1 Hz, yielding a time series of $f_{16}$ and $\mathrm{MFH}_{16}$. To be able to correlate the frequency drift with the ambient temperature, $T_a$, the room temperature was logged with a miniature temperature data logger (SL52T, Signatrol, Tewkesbury, UK) positioned at the outside wall of the RF cage at a sampling rate of 2 minutes. The correlation between $f_{16}$, $\mathrm{MFH}_{16}$ and $T_a$ was determined by the Pearson correlation coefficient $p$. During the 2-hours break on day 2, three full rotations of the magnetic field camera were performed to measure the $\mathrm{MFH}_{192}$ and $f_{192}$. For these rotational measurements, it was assured that the quadrupole and dipole magnets in all beamlines were switched off.

### 3.1.4 Influence of gantry position and rotation

*This section results from a collaborative work of S.Schellhammer and myself and was already described in (Schellhammer, 2019), however as the result is relevant for the rest of this study it is briefly presented here.*

The proton therapy facility introduces three types of magnetic fields interacting with the MRI system. Firstly the static fringe field produced by the cyclotron, which is compensated for during MRI system shimming (Schellhammer et al., 2018b). Secondly, the large rotating ferromagnetic mass of the gantry in the neighboring treatment room changes the environmental magnetic field depending on its angular position. The latter regularly changes position during clinical operation and may affect both the spatial homogeneity and the absolute value of $B_0$, which can lead to image deformations and shifts, respectively. Therefore, both $f_{192}$ and $\mathrm{MFH}_{192}$ were quantified three times for static gantry positions of 0°, 90°, 180° and 270°, respectively, as well as during both clockwise and counter-clockwise gantry rotation at a speed of 1°/s and 6°/s, respectively. The third source of external magnetic fields are the quadrupole and dipole magnets in all beamlines of the PT facility and will thus be studied in the following.

### 3.1.5 Effect of FBL and GTR beamline magnets

The magnetic fringe fields produced by the beamline magnets are expected to overlap with the magnetic field deployed for imaging by the in-beam MRI scanner and hence distort the $B_0$ field. To study this effect, the $B_0$ field was mapped with the FBL beamline magnets being energized for nominal proton energies in the clinical range of $75\,\mathrm{MeV} - 225\,\mathrm{MeV}$ at equidis-

tant energy steps of 25 MeV. For each beam energy one full rotational measurement by the magnetic field camera was acquired with baseline measurements using non-energized beamline magnets in between. The latter were used to compensate for the magnetic field drift that may occur due to environmental temperature changes, through a linear relationship. For the beamline settings at 125 MeV two additional full rotations were performed, to measure the reproducibility and the robustness of the drift rate correction. In the same manner, the influence of the operation of the GTR beamline was investigated. Therefore, the GTR beamline was set to an energy of either 100 MeV, 125 MeV, 175 MeV or 225 MeV (representing passive beam delivery), with one camera rotation being performed for all energies and an additional double repetition for 125 MeV. Furthermore, these measurements were repeated for gantry angles of 0°, 90° and 270°. This was important, as the gantry position and rotation experiments described in Section 3.1.4 only investigated the effect of moving the ferromagnetic mass of the gantry while the dipole magnets inside the gantry, which bend the beam towards the patient were turned off. In this experiment, however, with the different positions of the magnets, a potential change in their fringe field was investigated.

## 3.2 Results

### 3.2.1 Frequency drift and reference measurements

Figure 3.4 shows the results of the drift measurement of the mean resonance frequency $f_{16}$, the $\mathrm{MFH}_{16}$ and the ambient temperature $T_a$ over 4 days. The mean resonance frequency $f_{16}$ was found to oscillate with a periodicity of about 24 h, with a maximum absolute slope of about 15 Hz/h and an amplitude of about 60 Hz. Given the temperature coefficient of the residual magnetic flux density of the magnets material -0.1 %/K (Hitachi, 2019), this translates to a temperature change on the order of 10 mK inside the permanent magnet material. Ambient temperature measurements showed changes in the range of 23.7 °C – 24.2 °C over the course of the experiment. The temperature $T_a$ and frequency $f_{16}$ were negatively correlated with $p$ = -0.62. The $\mathrm{MFH}_{16}$ exhibited an oscillating behavior, positively correlated ($p$ = 0.95) with the frequency $f_{16}$, with the same 24 h periodicity and an amplitude of about 1.5 ppm. Sharp drops in the resonance frequency and MFH indicate activities in the nearby treatment room (energizing the GTR beamline leads to an energy-dependent
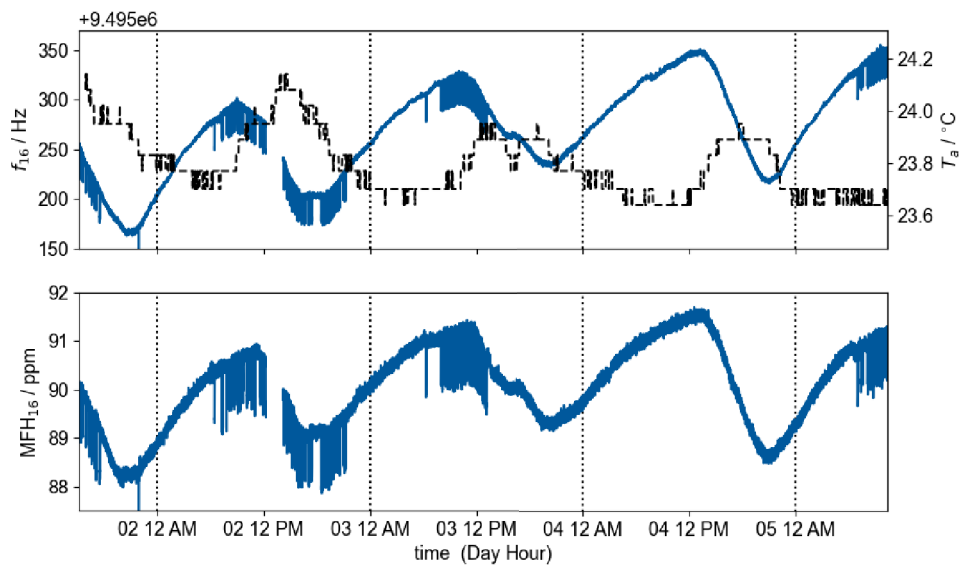
**Figure 3.4:** Multi-day drift measurement of the mean resonance frequency, $f_{16}$, (blue solid) and room temperature (black dashed) in the upper plot, as well as magnetic field homogeneity, $\mathrm{MFH}_{16}$, in the lower plot. Dotted vertical lines separate individual days. During the 2 h data void on the second day reference measurements were performed with the 360° rotating magnetic field camera. Figure reprinted from Gantz et al. (2021).
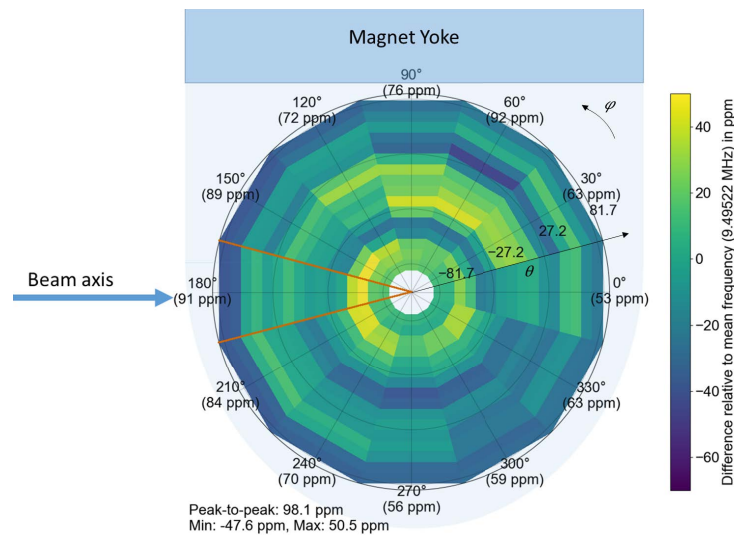


**Figure 3.5:** Polar plot of the 3D magnetic field map of the MRI scanner superimposed onto a top-view of the MRI scanner with the 192 measurement points on a 22 cm DSV. Angular component denotes camera position ($\varphi = 0°$ equals the position away from the beamline). Radial component of the plot denotes the individual NMR probes, South pole in the center, North pole at the rim. The beam axis was added for a better understanding of the geometrical position. Distances are not to scale. $\mathrm{MFH}_{16}$ values for the individual angular measurements are given in brackets. Figure reprinted from Gantz et al. (2021).
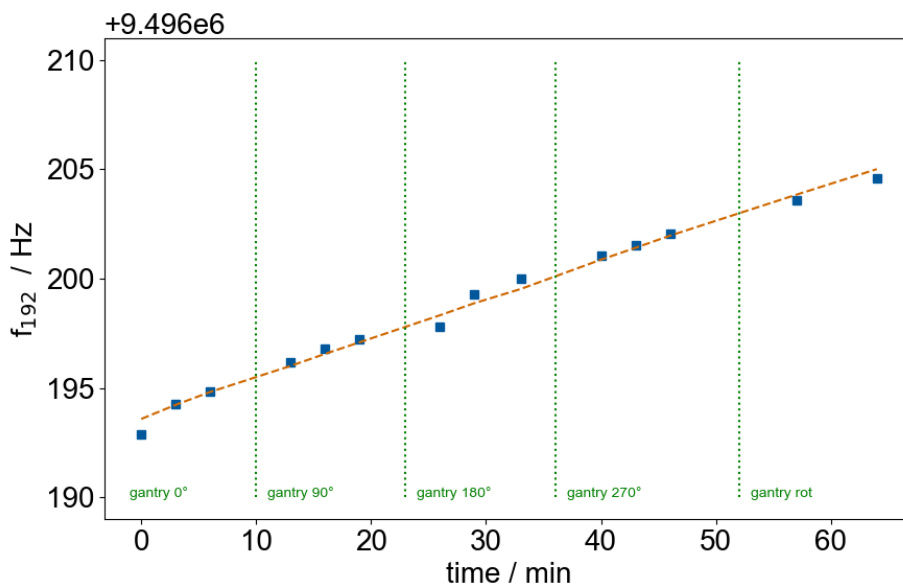
**Figure 3.6:** Measurement of the central frequency, $f_{192}$, for different gantry angles and during gantry rotation. The ambient temperature induced frequency drift is accounted for by a linear function (dashed orange).

decrease in $f_{16}$, compare Section 3.2.3). The 2 h data-void on the second day corresponds to the point of time of the reference rotation measurements. For these rotations, with all beamline magnets switched off, the $\mathrm{MFH}_{192}$ was 98.1 ppm, 97.9 ppm and 98.2 ppm (Figure 3.5). Absolute differences between the three measurements were within 2.1 ppm of all 192 probes. The mean and standard deviation of $f_{192}$ for the three measurements was $(9495219.0 \pm 1.7)$ Hz.

### 3.2.2 Influence of gantry position and rotation

On a short time scale (60 min), the above observed frequency drift can be modeled by a linear approximation. For all measurements with different gantry positions and gantry rotation, $f_{192}$ and $\mathrm{MFH}_{192}$ showed deviations from this linear drift (0.18 Hz/min) of less than 2 Hz and 2 ppm, respectively, see Figure 3.6. For typical gradient amplitudes of the MRI pulse sequences used on this MRI scanner which are on the order of 1 mT/m to 10 mT/m, a change of 2 Hz in $f_{\mathrm{res}}$ would translate to image shifts of 50 μm to 5 μm. Therefore, these shifts can be considered negligible as MRI images typically have pixel-dimensions on the order of a tens of a mm up to a few mm.

**Table 3.1:** Measured central resonance frequency change $\Delta f_{192}$ as a function of proton beam energy-dependent setting of FBL and GTR beamline as well as gantry angle in the nearby treatment room. For 125 MeV the mean and $1\sigma$ spread is given, resulting from a threefold repetition of the measurement.

| Beamline | Gantry angle / ° | $\Delta f_{192}$ / Hz for **Energy** / **MeV** | | | | | | |
|---|---|---|---|---|---|---|---|---|
| | | **70** | **100** | **125** | **150** | **175** | **200** | **225** |
| GTR | 0 | - | -20.4 | $-23.0 \pm 0.5$ | - | -26.6 | - | -23.0 |
| GTR | 90 | - | -20.7 | $-23.1 \pm 0.5$ | - | -27.6 | - | -26.6 |
| GTR | 270 | - | -21.3 | $23.8 \pm 0.5$ | - | -28.3 | - | -25.2 |
| FBL | 0 | -12.9 | -14.9 | $-15.7 \pm 0.5$ | -16.3 | -15.8 | -10.8 | 7.3 |

### 3.2.3 Influence of FBL and GTR beamline operation

The change in mean resonance frequency, $\Delta f_{192}$, as a function of the proton beam energy-dependent setting of both the GTR and FBL beamlines is shown in Table 3.1. For the FBL beamline, a marked beam energy-dependent change in $\Delta f_{192}$ is observed, with the mean frequency decreasing by 10 Hz – 16 Hz for all energies between 75 MeV and 200 MeV and increasing by 7 Hz for 225 MeV. For the GTR beamline, however, for all studied energies, a decrease of $\Delta f_{192}$ on the order of 20 Hz – 30 Hz was measured, with only a weak energy-dependence. Furthermore, the gantry position was found to exhibit only a minor effect on the measured changes in $\Delta f_{192}$, with the highest difference being 3.3 Hz, observed for 225 MeV at gantry angles of 0° and 90°. For all measurements, no relevant changes in $\mathrm{MFH}_{192}$ were seen, with maximum point-wise differences below 2.5 ppm as compared to reference.

## 3.3 Discussion

This work quantitatively investigated the influence of the magnetic fringe fields produced by the proton therapy system and all its beamlines onto the $B_0$ field of the MRI scanner.

The $B_0$ field measurements over a 22 cm DSV have shown that the peak-to-peak homogeneity of 98 ppm is within the operating specifications of the low-field open MRI scanner used in this study. Although this value is higher than the typical specification of $\sim$2 ppm for superconducting closed-bore high-field diagnostic MRI systems, it is sufficient for the purpose of prototyping an MRiPT system. High $B_0$ field homogeneity is required for fat suppression, phase-based imaging, spectroscopy and echo-planar imaging type of pulse

sequences (Bernstein et al., 2004). As SE-based pulse sequences show a relatively small sensitivity to $B_0$ field perturbations, an acceptable image quality can still be achieved with inhomogeneities of several tens of ppm (Blasche & Fischer, 2017; Marques et al., 2019). In addition, the $B_0$ field measurements showed three external sources perturbating the central resonance frequency ($f_0$) of the MRI scanner. Firstly, a residual daily magnetic field oscillation on the order of ±1.4 µT (±60 Hz), which was shown to correlate with ambient temperature, thus indicating imperfections in the thermal insulation of the temperature-sensitive permanent magnet material. Secondly, the operation of the proton beamline at which the MRI scanner is operated (FBL beamline) resulted in a change in $B_0$ field strength on the order of 0.35 µT (15 Hz) induced by the fringe fields of the beamline magnets. Thirdly, also the operation of the neighboring gantry-based clinical beamline (GTR beamline) was found to result in a change in $B_0$ field strength on the order of 0.5 µT − 0.7 µT (20 Hz − 30 Hz). All of these effects may be compensated by the implementation of a more accurate $f_0$ calibration method directly before acquisition of each MR image (Maier, 1989). This, however, only suffices when imaging is performed under constant beamline settings. While this seems readily achievable for the FBL beamline, for the GTR beamline, this requires accurate monitoring of the operation of the therapy beamline, to assure that MR imaging is only performed while the beamline is inactive. Especially, when looking into a future clinical application, this needs to be incorporated in all workflow considerations and may significantly prolong the treatment time per patient, as e.g. setup by MR imaging could not be performed while the second beamline is irradiating. Alternative measures to reduce these effects on $B_0$ are an improvement in thermal insulation and magnetic shielding of the MRI system against external fields.

Coming back to the motivation for this study, the vertical image shifts which were observed by Schellhammer (2019) during simultaneous imaging and irradiation using 125 MeV proton beams were sequence read-out gradient dependent, with larger shifts for sequences having smaller gradient amplitudes. As shown in Section 2.2.2, a change in the resonance frequency, $\Delta f_0$, results in a spatial off-resonance misencoding $\Delta x = \Delta f_0 / \gamma G_x$ in the frequency-encoding direction, where $\gamma$ is the gyromagnetic ratio of hydrogen nuclei (42.6 MHz/T) and $G_x$ is the frequency encoding gradient amplitude. Given the measured change in $f_{192}$, which was (-15.7 ± 0.5) Hz for 125 MeV, shifts of 0.1 mm to 0.5 mm are expected for gradient amplitudes between 5.7 mT/m and 0.7 mT/m as was used for the imaging experiments (Gantz et al., 2021). These results prove that the change in resonance fre-

quency caused by the operation of the beamline is in fact the reason for the observed image translations. In fact, a shift in the MR images can be understood as a translation of the co-ordinate system of the MR images. Future studies need to show how the coordinate system of the MR images can be reproducibly co-localized to an external fixed reference system (e.g. the proton beam coordinate system or the geometric center of the MRI scanner). One promising strategy would be to perform an updated precision-enhanced central resonance frequency determination of the MRI scanner not only before each imaging session but for each image acquisition individually, with the beamline already energized. This would, to-gether with a geometrically fixed image object, assure a reproducible co-localization of the coordinate systems.

A limitation of this study is that no dynamic effects of external magnetic field perturba-tions were investigated, such as a change in the magnetic fringe fields caused by switching on and off the nearby cyclotron or the proton beamline magnets during MR image acqui-sition. The former effects are known to potentially lead to severe image blurring (Hofman et al., 2013), whereas the latter will be discussed in detail in Chapter 5, when magnetic interactions and the effects of simultaneous PBS irradiation and MR imaging on the image quality are investigated.

The investigations described in this chapter provide the magnetometric evidence to un-derstand and support previous results of simultaneous imaging and static irradiation ex-periments performed with the same setup. Especially, it underlines the necessity to strictly monitor all activities in the proton therapy facility and incorporating them into an MR imaging guided PT workflow. This will assure perturbation free MR images and the correct repre-sentation of their absolute position. Furthermore, the $B_0$ field drift and $B_0$ field changes due to the operation of the beamlines need to be taken into account for any further experiment design. Consequently, when taking the next step of integrating the MRI scanner with an actively scanned proton beam, a comprehensive magnetometric investigation with the MRI scanner positioned at the PBS beamline will be necessary again (see Chapter 5).

# 4 Combination of the MRI scanner with a horizontal dedicated PBS Beamline

With the magnetometry of the MRI system at the static beamline understood, the next step towards clinical MRiPT prototyping is to combine the MRI scanner with active proton beam delivery at a PBS beamline, which was installed in the research room of UPTD in September 2018. This beamline allows active volumetric field formation, and PBS is currently considered the only feasible solution to deliver a clinical proton treatment field inside an MRI magnetic field. For passive scattering the magnetic deflections would be extremely complex (Oborn et al., 2017), whereas for PBS several techniques have been proposed to compensate for the beam deflection for each beamlet individually (Hartman et al., 2015; Moteabbed et al., 2014; Schellhammer & Hoffmann, 2017). This chapter consist of adaptations and technical feasibility considerations that were necessary to realize the combination of the low-field MRI scanner with the PBS nozzle. Firstly, the verification of the position and size of the beam-stopper was performed. This was required, as introducing the MRI scanner at the PBS beamline alters the proton trajectories and for radiation protection reasons, all beams have to be stopped in a beam-stopper. Secondly, the size and shape of the irradiation field that is deliverable inside the MRI scanner was predicted from first principles and confirmed by film-dosimetry measurements.

## 4.1 Installation of the MRI scanner at the PBS beamline

**Setup**   For this study, the MRI scanner was positioned at the horizontal dedicated PBS nozzle (IBA Particle Therapy, Louvain-la-Neuve, Belgium), which was installed as a second independent beamline in the research room at UPTD (Figure 3.2). The MRI scanner was positioned as close as possible to the distal end of the PBS nozzle, to minimize air scattering and to bring the isocenter of the MRI scanner as close as possible to the natural isocenter of the PBS nozzle, called "PBS isocenter" in the following. To achieve a
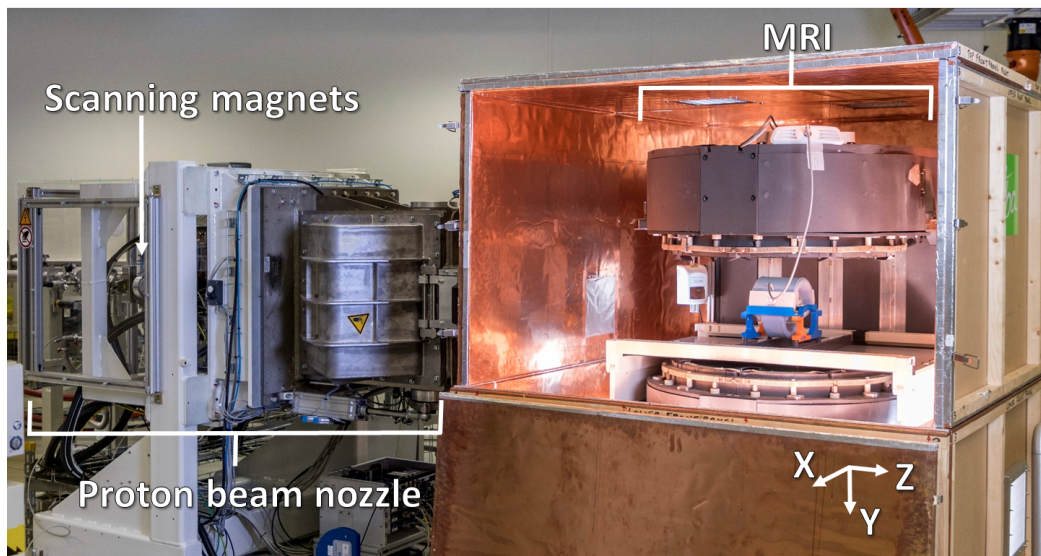
**Figure 4.1:** Experimental setup with partially opened Faraday cage. The in-beam MRI scanner is positioned directly in front of the proton PBS nozzle, which houses the X and Y beam scanning magnets. [Courtesy of HZDR/R.Weisflog]. Figure adapted from Gantz et al. (2020).

minimal distance between MRI scanner and PBS nozzle and to allow volumetric irradiation, the waveguide used at the FBL beamline was exchanged by a window covered with a thin copper foil (thickness 0.12 mm). The foil is a compromise between minimal material in the beam path, to prevent beam widening by scattering, and the shielding-quality of the RF cage. With this adaptation, the MRI scanner was reproducibly positioned with the MRI isocenter on the central beam axis 39 cm downstream of the PBS isocenter.

**Coordinate system** For all investigations where the MRI scanner is operated at the PBS beamline (Chapter 4 and Chapter 5), a consistent coordinate system was used, which followed the nomenclature of the IBA beam delivery system. Here, the central beam axis is denoted as the Z axis. The X axis is the horizontal direction, with the positive axis pointing along the direction of lateral beam deflection, away from the yoke of the magnet of the MRI scanner, i.e. the X axis is pointing to the right in beam's eye view. Finally, the Y axis is the vertical direction, with Y pointing downwards, i.e. anti-parallel to the direction of the magnetic field of the MRI scanner (Figure 4.1).

**Beam delivery at the PBS beamline** Beam delivery at the PBS beamline is realized by irradiation spot maps which have been designed and calibrated to deliver beam spots to the

PBS isocenter. The notation for pencil beams to be delivered to the lateral X-Y plane at PBS isocenter is ($X_{PBSiso}$,$Y_{PBSiso}$) with $X_{PBSiso}$ and $Y_{PBSiso}$ in mm, following the coordinate system given above. Therefore, if not specified otherwise, all beam spot positions in this chapter and in Chapter 5 will be given for the PBS isocenter. However, for any position other than the PBS isocenter, e.g. further downstream, the field size and spot sizes will differ significantly. For all energies greater or equal to 100 MeV the maximum field sizes at PBS isocenter are 400 mm and 300 mm in horizontal and vertical direction, respectively. For energies below 100 MeV, the maximum field size in horizontal direction is slightly smaller at 390 mm. Note here, that these values do not account for the width of individual beam spots, but denote the center coordinates of each spot, i.e. the absolute field sizes will be larger than given here, depending on the spot width. For each spot map, the target monitor unit (MU) for each spot is defined individually. The resulting dose per spot changes with both lateral and depth position as well as beam energy. A complete description of the beam properties or commissioning of the beamline is beyond the scope of this work, but has to be performed in future studies. Here, considerations regarding beam delivery were limited to those absolutely necessary to study the general applicability of simultaneous imaging and irradiation (Chapter 5).

## 4.2 Position verification of the beam-stopper

**Material and methods**   A fixed-position beam-stopper is required for the operation of the PBS beamline. This experiment is performed, firstly, to verify that the beam-stopper is sufficiently large and correctly positioned relative to the MRI scanner and PBS beamline to absorb all beams at the maximum field size, including the beam deflections caused by the magnetic field of the MRI scanner. Secondly, this investigation shall provide experimental input data for a detailed simulation of the combined MRI scanner and PT setup, which will be important for future studies, such as MRI scanner position verification, treatment planning for MR-integrated PT and next-generation system design. A 600 l water-filled plastic tank (dimensions (W × H × D): 120 cm × 80 cm × 100 cm) was installed on an aluminum frame, with a table height of 88.5 cm (Figure 4.2). The beam-stopper was positioned such that its front face is at a distance of 1.80 m downstream of the MRI isocenter, i.e. 2.19 m downstream of the PBS isocenter. Note, that this is the minimum distance to allow the MRI

scanner to be removed from the beamline without moving the beam-stopper, as the room laser pillars of the beamline block a purely lateral exit of the MRI scanner. The beam-stopper is positioned with a lateral offset of $\Delta = (+14.5 \pm 1)$ cm in positive X direction relative to the central Z axis.

To verify the position and size of the beam-stopper for operation of the PBS beamline both with and without the MRI scanner at the beamline, two radiochromic film (Gafchromic EBT3, Ashland, USA) measurements were performed: Firstly, in the absence of the MRI scanner and secondly, with the MRI scanner installed as described above. Both measurements were performed with film sheets installed at the proximal plane (front-face) of the beam-stopper to verify the field size. For the first measurement, in the absence of the MRI scanner, the top-right quadrant of the field was measured using 6 spots: (8,-150), (8,30) and (195,30) using 70 MeV proton beams and (53,-150), (53,-35) and (200,-35) using 220 MeV. These spots were chosen to study both energies on the same films, thus reducing setup errors, but requiring offsets from the central X and Y axis in order to assure that the spots do not overlap. The MU per spot were 1860 MU and 225 MU for 70 MeV and 220 MeV, respectively. Additionally, 5 spots forming a small central cross around the (0,0) coordinate were irradiated on a separate film using 220 MeV to check the alignment of the horizontal and vertical laser lines with the center spot irradiation and compensate for any potential offset between central beam spot and laser coordinate center.

The second set of film measurements at the beam-stopper was performed as a transmission measurements through the magnetic field of the MRI scanner. Therefore, the MRI scanner was positioned at the beamline, with the upper part of the RF cage removed, in order to minimize further enlargement of the spot sizes by scattering due to the copper foil and plywood in the beam path. This experiment was only performed for the horizontal field direction, as for the vertical direction no beam deflections were expected and the previous experiment yields the field size along the vertical axis. Furthermore, the vertical maximum field size with the MRI scanner at the beamline was expected to be mainly limited by the space between the magnet poles, as discussed in Section 4.3. For this experiment, proton beam energies of 70 MeV, 125 MeV and 220 MeV were used, thus covering the whole range of energies available at the PBS beamline. This was important, as beam deflections strongly depend on proton beam energy. Beam spots used for the three energies were (0,0), (50,0), (100,0), (150,0) and (200,0) for both 125 MeV and 220 MeV and (0,0), (0,60), (0,120) and (0,195) for 70 MeV. Here, the distances between the spots for 70 MeV had to

**(a)**          **(b)**
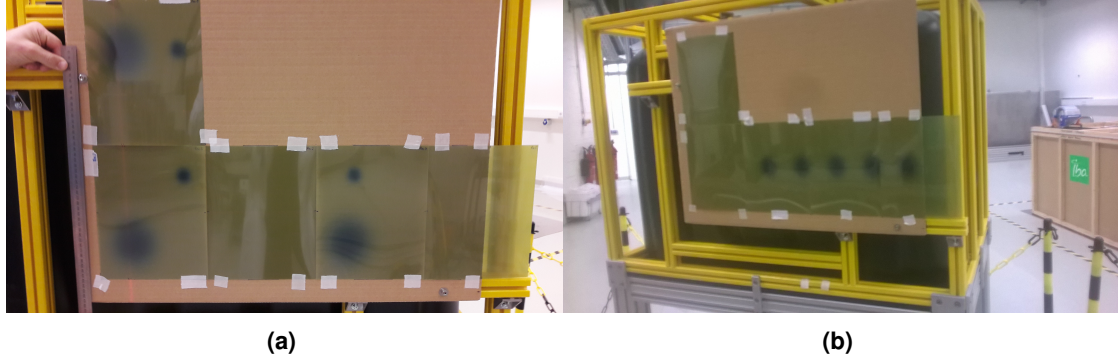
**Figure 4.2:** EBT3 films at the beam-stopper. (a) Survey of horizontal and vertical field size of the right upper quadrant without the MRI scanner at the beamline using 70 MeV and 220 MeV beams (large and small spots, respectively). (b) Verification of horizontal beam deflection for 125 MeV beams and 5 dose spot irradiations covering the positive X-axis.

be increased because of the larger spot size to avoid overlapping spots. MU per spot were 1860 MU, 770 MU and 225 MU for 70 MeV, 125 MeV and 220 MeV, respectively. For both experiments, dose evaluation of the irradiated films was performed following an in-house standardized procedure (Schellhammer, 2019). Spot center positions, $X_{Film}$ and $Y_{Film}$, and 1$\sigma$ spot width, $\sigma_X$ and $\sigma_Y$, were determined by a fit of a two-dimensional Gaussian function of the 2D dose profile of the film for each spot individually. For all spots from the first measurement, i.e. in the absence of the MRI scanner, a linear regression $X_{Film} = a \times X_{PBSiso}$ and $Y_{Film} = b \times Y_{PBSiso}$ was calculated from these coordinates to gain magnification factors $a$ and $b$. These magnification factors serve two reasons: Firstly, they were necessary to estimate the full lateral field size at the front face of the beam-stopper and secondly, using these factors, the deflection $\Delta X$ by the magnetic field of the MRI scanner could be determined as $\Delta X = X_{Film,MRI} - X_{calc}$, where $X_{Film,MRI}$ are the $X_{Film}$ coordinates from the second measurement and $X_{calc} = a \times X_{PBSiso}$ are the corresponding spot positions to be expected in the absence of the MRI scanner.

**Results** The alignment offset between laser lines and central irradiation spot was -6 mm and -1 mm in X and Y direction, respectively. Thus, for all further spot coordinates, a correction vector of (+6 mm, +1 mm) was applied, to compensate for the offset in laser alignment. Measured positions of all 6 spots delivered for the first experiment without the MRI scanner at the beamline are given in Table 4.1. The linear regressions resulted in the following transformations: $X_{calc} = 2.129 X_{PBSiso}$ (R$^2$ > 0.999) and $Y_{calc} = 1.947 Y_{PBSiso}$ (R$^2$ > 0.999).

**Table 4.1:** Measured center positions (corrected for offset of laser lines) of the 6 spots delivered onto EBT3 film at the front face of the beam-stopper in the absence of the MRI scanner.

| Energy / MeV | $(X, Y)_{PBSiso}$ | $X_{Film}$ / mm | $Y_{Film}$ / mm |
|:---:|:---:|:---:|:---:|
| 70 | | | |
| | (8, 30) | $15 \pm 5$ | $55 \pm 5$ |
| | (195, 30) | $413 \pm 5$ | $60 \pm 5$ |
| | (8, -150) | $18 \pm 5$ | $-291 \pm 5$ |
| 220 | | | |
| | (53, -35) | $114 \pm 2$ | $-70 \pm 2$ |
| | (53, -150) | $113 \pm 2$ | $-293 \pm 2$ |
| | (200, -35) | $427 \pm 2$ | $-68 \pm 2$ |

These magnification factors agree to trigonometric predictions, using intercept theorem, within $\pm\,0.5\,\%$ (underlying distance measures to the scanning magnets are given in Section 4.3). Resulting from these data, the full field size (X,Y) at the front face of the beam-stopper without the MRI scanner in place is 88 cm by 58 cm. Note here, that this consideration does not include the spot width. Measured FWHM (full width at half maximum) spot sizes were $(18 \pm 3)$ mm, $(40 \pm 5)$ mm and $(60 \pm 10)$ mm for beam energies of 220 MeV, 125 MeV and 70 MeV, respectively.

For the second experiment, with the MRI scanner at the beamline, measured beam spot positions at the beam-stopper are given in Table 4.2. The maximum $X_{Film}$ positions for the studied (positive) half of the X-axis of the irradiation field were 695 mm, 631 mm and 577 mm for energies of 70 MeV, 125 MeV and 220 MeV, respectively. These positions can be understood as a composition of the expected position, $X_{calc}$, without the MRI scanner in place at this depth along the central beam axis, superpositioned with a beam deflection by the main and fringe fields of the MRI scanner. The beam deflections $\Delta X$ show two trends, firstly, the lateral deflections increase with decreasing proton energy due to a reduced gyroradius (which scales with the kinetic energy of the protons) and secondly, within each energy the deflection values are decreasing with increasing $X_{PBSiso}$, i.e. distance from the irradiation field center. The latter effect can be understood by the particle trajectories, traversing the $B_0$ field further away from the central axis, thus experiencing less of the magnetic field of the MRI scanner.

Combining the results from both film irradiation experiments, Figure 4.3 illustrates the field size and position at the front face of the beam-stopper both with and without the MRI scanner. Note, that with the MRI scanner, only the positive X axis was measured, while the
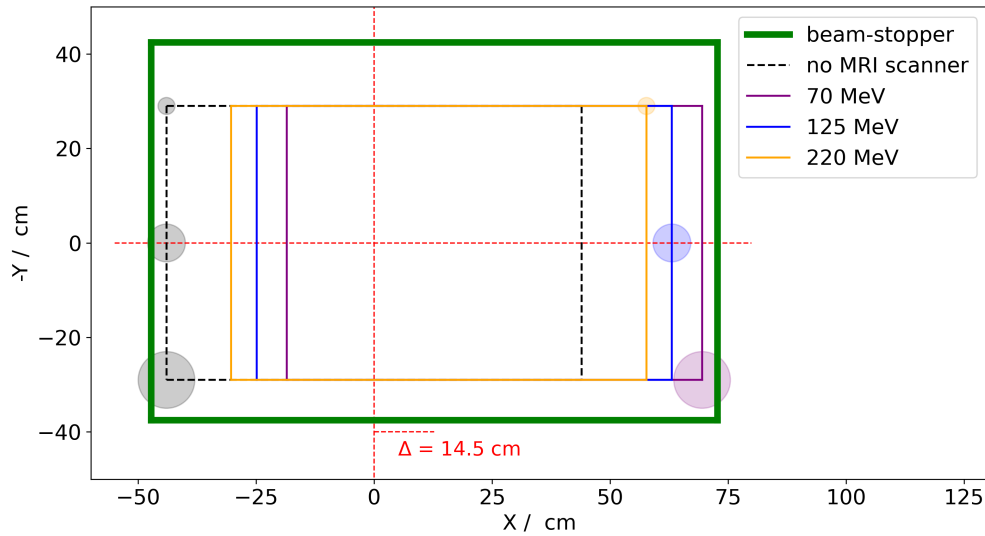
**Figure 4.3:** Comparison of field size and position at the front face of the beam-stopper both with and without the MRI scanner in place. Black circles illustrate the FWHM spot sizes of proton beams of 70 MeV, 125 MeV and 220 MeV (bottom to top). Colored circles denote the spot sizes of their respective color. The lateral offset $\Delta$ at which the beam stopper was installed relative to the central Z axis is indicated in red.

field extension in Y and negative X direction is extrapolated from the measurements without the MRI scanner, neglecting the $B_0$ field-induced trapezoidal field deformations (compare Section 4.3). Additionally, FWHM spot sizes were added to the figure as circles, to highlight, that the field size only refers to spot center coordinates. This result shows, that the position of the beam-stopper has to be considered a compromise between operation with and without MRI scanner. For energies of 125 MeV and above nearly all primary particles will be stopped inside the water tank, however, for lower energies, due to the greater lateral beam deflection and also scattering in air (which significantly increases the spot size) the beam-stopper is not sufficiently large in X direction and further measures have to be taken to control the complete absorption of all primary particles. Therefore, for all further irradiation measurements performed at the PBS beamline described in this thesis, additional water tanks were used closer to the beamline (i.e. inside the MRI scanner), to assure all particles are appropriately stopped.

**Table 4.2:** Spot coordinates $X_{Film}$ as measured with EBT3 film at the front face of the beam-stopper for all spots delivered through the $B_0$-field of the MRI scanner. Additionally, the expected position without the the MRI scanner, $X_{calc}$ and the difference $\Delta X$ by lateral deflection is given.

| Energy | $X_{PBSiso}$ / mm | $X_{Film}$ / mm | $X_{calc}$ / mm | $\Delta X$ / mm |
|---|---|---|---|---|
| 70 MeV | | | | |
| | 0 | $319 \pm 5$ | $0 \pm 2$ | $319 \pm 6$ |
| | 60 | $443 \pm 5$ | $128 \pm 2$ | $315 \pm 6$ |
| | 120 | $561 \pm 5$ | $255 \pm 2$ | $305 \pm 6$ |
| | 195 | $695 \pm 5$ | $415 \pm 2$ | $281 \pm 6$ |
| 125 MeV | | | | |
| | 0 | $233 \pm 3$ | $0 \pm 2$ | $233 \pm 4$ |
| | 50 | $338 \pm 3$ | $106 \pm 2$ | $232 \pm 4$ |
| | 100 | $440 \pm 3$ | $213 \pm 2$ | $227 \pm 4$ |
| | 150 | $538 \pm 3$ | $319 \pm 2$ | $219 \pm 4$ |
| | 200 | $631 \pm 3$ | $426 \pm 2$ | $206 \pm 4$ |
| 220 MeV | | | | |
| | 0 | $171 \pm 2$ | $0 \pm 2$ | $171 \pm 3$ |
| | 50 | $277 \pm 2$ | $106 \pm 2$ | $170 \pm 3$ |
| | 100 | $379 \pm 2$ | $213 \pm 2$ | $167 \pm 3$ |
| | 150 | $480 \pm 2$ | $319 \pm 2$ | $161 \pm 3$ |
| | 200 | $577 \pm 2$ | $426 \pm 2$ | $152 \pm 3$ |

## 4.3 Determination of maximum radiation field size inside the MRI scanner

When integrating the MRI scanner at the PBS beamline, it has to be assured that the magnet poles and the yoke of the MRI scanner are not directly irradiated. This is important not only to prevent radio-activation of the MRI scanner but additionally to prevent radiation-induced demagnetization of the permanent magnet material (Ito et al., 2001). To guarantee this, the maximum field size applicable inside the MRI scanner had to be determined. Therefore, firstly, the maximum field size was estimated by trigonometric consideration and secondly it was verified by film measurements performed between the magnet poles of the MRI scanner. The latter experiment also enables an experimental verification of the predicted trapezoidal deformation of the irradiation field due to the main and fringe magnetic fields of the MRI scanner (Oborn et al., 2015).

**Trigonometric estimation** To estimate the maximum field size inside the MRI scanner, the center of the two X and Y scanning magnets, which are at a distance of 194.2 cm

**Figure 4.4:** Schematic of the experimental setup of the MRI scanner relative to the Y and X scanning magnets for trigonometric consideration of vertical (a) and horizontal (b) maximum field size in the MRI scanner.

and 234.5 cm relative to the PBS isocenter, respectively, were assumed as virtual point sources of the scanned proton beams. Directing the proton beams to the most distal position of the magnet poles and the yoke of the magnet of the MRI scanner for vertical and horizontal direction, respectively, yields an approximation of the largest applicable field to beam isocenter coordinates $\Delta x$ and $\Delta y$, see Figure 4.4a and b. Additional measures required are the distance between MRI isocenter to PBS isocenter (39 cm), magnet pole gap (38 cm), width of the yoke (92 cm) and the diameter of the magnet poles (77 cm). Using the intercept theorem, the resulting maximum half-field sizes $\Delta x$ and $\Delta y$ in horizontal and vertical direction are 36.2 cm and 14.3 cm, respectively. However, the maximum field size of the PBS nozzle is $\pm 20$ cm and $\pm 15$ cm in horizontal and vertical direction, respectively.
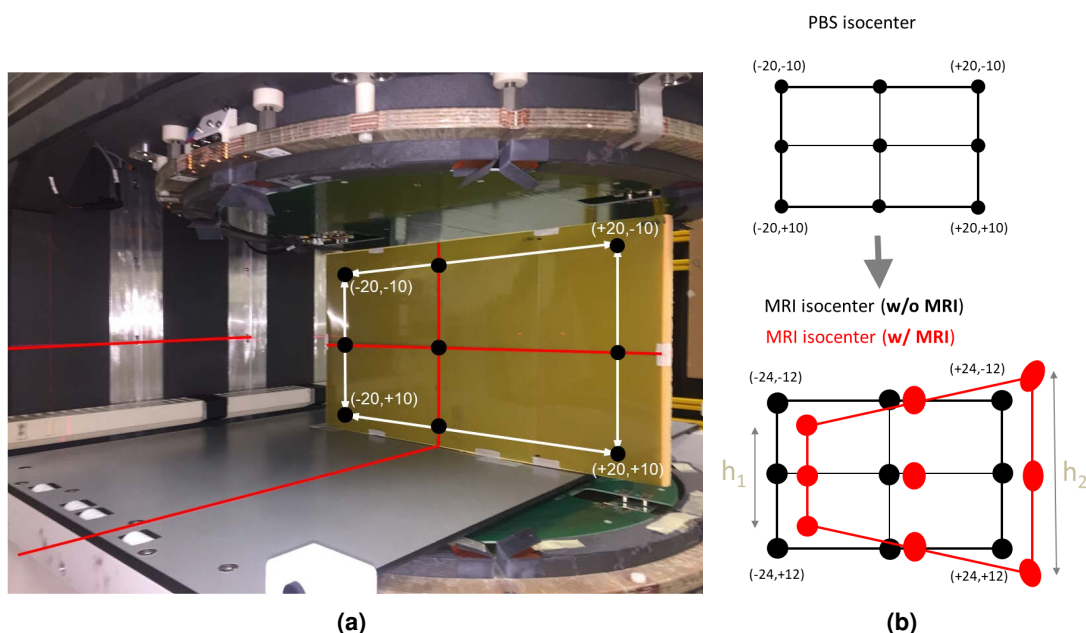
**Figure 4.5:** Setup of the field size measurement inside the MRI scanner, using a vertically placed EBT3 film at the lateral plane of the MRI isocenter. Given spot coordinates denote lateral $(X, Y)_{PBSiso}$ coordinates in PBS isocenter. Red lines in (a) mark the PBS laser lines used for reproducible positioning of the radiochromic films and MRI isocenter localization.

Thus, for the horizontal direction, no restriction in field size needs to be considered, as the 36.2 cm is greater than the maximum half-field size and this estimation is a worst-case scenario only, not taking into account beam deflection, which further deflects the proton beams away from the yoke. However, for the vertical direction the estimated half-field size $\Delta y$= 14.3 cm is smaller than the maximum achievable field size of $\pm 15$ cm. Here, a limitation of the field size has to be considered, as for the maximum field size the magnet poles would be irradiated. In addition, this estimation does neither include beam width nor beam widening by air scattering, thus it is too optimistic. The vertical field size limit should be chosen considerably smaller at $\pm 10$ cm only.

For the vertical direction, the planned field size of $\pm 10$ cm at PBS isocenter was dosimetrically verified by EBT3 films using 220 MeV beams at the most distal position between the magnet poles, i.e. 38.5 cm behind the MRI isocenter. Two spots ((0,10) and (0,-10)) were delivered and the distance of the centers was measured to be $(27.0 \pm 0.5)$ mm which agrees to the trigonometric calculation (26.6 cm).

**EBT3 film measurements at MRI isocenter**   For future dose application experiments it is essential to define the field size at the vertical plane at the MRI isocenter. From geometric considerations, the field size at MRI isocenter can be estimated from the field size at PBS isocenter by taking into account a magnification factor of +20.1 % and +16.7 % for the horizontal and the vertical direction, respectively. A detailed beam commissioning here is much beyond the scope of the experiment, The experiment solely aims to confirm the calculated field size, measure the beam deflection, i.e. the absolute position of the field, and investigate whether previously predicted field deformations (Oborn et al., 2015), due to the main and fringe magnetic fields of the MRI magnet, can be experimentally verified. Therefore, for a set of three beam energies (70 MeV, 125 MeV and 220 MeV) a rectangular spot pattern including 9 spots marking the full field size of 40 cm x 20 cm (planned at the PBS isocenter) was irradiated and measured by a vertically placed EBT3 film at the lateral plane at the MRI isocenter (Figure 4.5a). Dose evaluation of the irradiated films was performed following an in-house standardized procedure (Schellhammer, 2019). A fit of the measured dose distribution of each individual spot by a two-dimensional Gaussian function yielded the center coordinates of the dose spots, spot width and tilt angle $\theta$ relative to the negative Y axis. The tilt angle is only reported for elliptical spots, with a difference in $1\sigma$ spot width of more than 1 mm between the two axes, as for a circular spot the choice of the tilt axis is arbitrary.

**Results**   A complete list of all measured spot positions, spot width and tilt angles is given in Table A.1 in the Appendix. Horizontal beam deflections of the central spot (0,0) were 26 mm, 19 mm and 15 mm for 70 MeV, 125 MeV and 220 MeV, respectively. 25 out of 27 measured spots had an elliptical shape, with a smaller horizontal than vertical axis length. Furthermore, off-axis spots showed a rotation of up to 22°, that increased with increasing beam energy and the major axis of the ellipse pointing away from the center of the irradiation field (Figure 4.5b). In addition, an energy-dependent, trapezoidal deformation of the irradiation field was observed, with maximum vertical height differences $\Delta h$ of 18 mm, 14 mm and 10 mm for 70 MeV, 125 MeV and 220 MeV, respectively (Figure 4.5b).

## 4.4 Discussion

The combined MRI and PT prototype system with the MRI scanner positioned at the PBS beamline, as realized in this work, is readily usable for technical feasibility studies. The position of the beam-stopper was optimized for the operation of the beamline both with and without the MRI scanner as well as for the full range of proton beam energies and the full field size available at the PBS beamline. It was found, that the beam-stopper is sufficient to stop the majority of the irradiated proton beams, both with and without the MRI scanner positioned in the beam path. However, for the most extreme spot positions in horizontal direction, it is necessary to use additional beam-stoppers closer to the PBS nozzle to assure that all primary particles are stopped. Furthermore, the beam deflection data can be used as input to validate a fully integrated computer simulation model of the MRI and PT system. Initial results have been presented by Oborn et al. (2020), showing that the experimentally determined beam deflections were systematically underestimated by the initial computer model by 6 mm to 21 mm. This shows that further studies are necessary to refine the computer model, e.g. by including of a detailed 3D magnetic field map of the MRI scanner.

For the maximum irradiation field inside the MRI scanner, the trigonometric calculations match the experimental verification measurements and have shown that a reduction of the maximum irradiation field size in vertical direction is necessary to prevent direct irradiation of the magnet poles. Thus, it is crucial to consider this for all following PBS irradiation experiments using this system. Furthermore, the irradiation field survey results demonstrate that the field size deformation predicted by Oborn et al. (2015) are indeed measurable with our experimental setup and that additionally, for the first time, a beam energy-dependent spot rotation was observed for all off-axis spots. The latter effect had not been described previously and its origin has to be investigated in follow-up studies.

Overall, the results indicate that in order to successfully irradiate an object placed in the magnetic field of the MRI scanner, methods for dosimetry and treatment planning in the presence of MRI magnetic fields have to be developed. This is beyond the scope of the current thesis. However, the combined MRI and PT system presented here is suitable to investigate the feasibility of simultaneous MR imaging and PBS irradiation in an experimental setting, as described in the following chapter.

# 5 Characterization of magnetic interference and image artefacts during simultaneous in-beam MR imaging and proton pencil beam scanning

For the first time, a low-field open MRI scanner was combined with a proton PBS research beamline. This combination allows a study that characterizes the magnetic fringe fields produced by the PBS system and to measure their effects on MR image quality during simultaneous PBS irradiation and MR image acquisition. For the first part, focusing on the magnetometry of the system, previous results from Chapter 3 have to be taken into account, such as the observed frequency drift that is expected to be comparable and thus will not be studied again. However, as the MRI scanner is now positioned at the PBS beamline, the environmental magnetic field conditions, mainly the fringe fields of all three beamlines, are altered as compared to the investigations presented in Chapter 3 and therefore the influence of the operation of all three beamlines and the operation of the gantry in the nearby treatment room on the $B_0$ field of the MRI scanner have to be quantified again. For the second part, the feasibility of imaging with static beamline settings (such as present for the passive beam delivery technique) has been previously shown (Gantz et al., 2021) and is therefore not addressed here. This chapter focuses solely on the more complex case of dynamic magnetic fields that are present during active PBS beam delivery and their effects on image quality during simultaneous MR imaging and PBS irradiation. Major parts of this chapter have been published in Gantz et al. (2020).

## 5.1 Material and methods

To investigate the feasibility of simultaneous MR imaging and PBS irradiation, the MRI scanner is operated at the PBS beamline, as described in detail in Chapter 4.

### 5.1.1 Magnetometry of external influences on the magnetic field of the MRI scanner

To characterize the effects of the magnetic fringe fields produced by the three beamlines (FBL, PBS and GTR) on the $B_0$ field of the MRI scanner, the NMR-based magnetic field camera is used (see Section 3.1.2). To position the magnetic field camera at the isocenter of the MRI scanner, the lower RF transmit coil was removed from the MRI scanner and water tanks were installed in between the PBS nozzle and the camera. For all following measurements the camera was either operated at a fixed position (directed towards the beamline) or manually rotated to acquire data on the full surface of the 22 cm DSV. For both cases, the central resonance frequency ($f_{16}$ or $f_{192}$) and the field homogeneity ($\mathrm{MFH}_{16}$ or $\mathrm{MFH}_{192}$) were measured (see the detailed description in Section 3.1.2).

**Influences from the GTR and FBL beamlines**

**Gantry position and rotation**    For the MRI scanner positioned at the FBL beamline, no influence of different gantry positions and gantry rotation was seen. However, with the MRI scanner now being closer to the gantry system, the same experiment was repeated for 4 gantry angles (0°, 90°, 180°, 270°), performing 3 full camera rotations each to measure $f_{192}$ and $MFH_{192}$, followed by clockwise and counter-clockwise gantry rotation with a rotation speed of 3°/s. During all these measurements, all beamline magnets were turned off and $f_{192}$ was drift-corrected by a linear function.

**FBL and GTR beamline magnets**    To assess the influence of energizing the beamline magnets of the FBL beamline, $\Delta f_{16}$ was measured as a function of the proton beam energy-dependent setting of the FBL beamline for energies of 70 MeV, 100 MeV, 125 MeV, 150 MeV, 175 MeV, 200 MeV and 224 MeV. This experiment was performed in continuous operation of the NMR camera with a sample of $f_{16}$ acquired each 5 seconds, with the beamline energized for 90 s and 60 s in between energies. The baseline was corrected using an asymmetric least-squares smoothing algorithm (Eilers & Boelens, 2005). For the GTR beamline, changes in $\Delta f_{16}$ were studied for one clinical treatment plan in PBS mode, consisting of 3 irradiation fields from gantry angles of 280°, 80° and 180°. The individual fields consisted of 38, 39 and 34 energy layers, with energies from 218 MeV − 103 MeV, 217 MeV − 100 MeV and 195 MeV − 100 MeV, respectively.

**Effects of the PBS beamline operation**

Since the settings of the electric currents running through the beam transport magnets and the scanning magnets are related to the requested beam energy and the spot position, respectively, two magnetometry experiments were conducted to assess the influence of the PBS beamline operation. Firstly, the fringe field effects of the PBS beamline magnets on the $B_0$ field were measured for a series of central spot irradiations at four different energies (70 MeV, 125 MeV, 170 MeV and 220 MeV), covering the full clinical range of proton energies. Secondly, the fringe field effects of the dipole scanning magnets on the $B_0$ field were measured for two extreme spot positions along both vertical ($Y_{PBSiso}$ = $\pm$ 10 cm) and horizontal ($X_{PBSiso}$ = $\pm$ 20 cm) axis at a fixed energy of 220 MeV. To prevent the camera from being irradiated, all magnets of the PBS beamline were energized without the proton beam being transported. Moreover, this allowed all magnets to be energized to the specified current settings for each individual spot for a suitable time (2 min) in order to manually rotate the camera over 360° to measure $f_{192}$ and $MFH_{192}$. All measurements were repeated three times in succession with baseline measurements using non-energized magnets in between, to compensate for the magnetic field drift due to environmental temperature changes in the permanent magnets of the MRI scanner (Huang et al., 2018; Li et al., 2009) that have been shown in Chapter 3.

**Hall probe measurements** The minimum acquisition time of the NMR camera is limited to about 1 s and therefore the camera is not capable of resolving dynamic changes in $B_0$ that occur faster then about 1 Hz. Therefore, to enable the measurement of dynamic fringe field effects produced by the beamline and scanning magnets during PBS operation, a triaxial Hall probe (THM1176LF, Metrolab, Geneva, Switzerland) was placed laterally from the center of the Y scanning magnet at 70 cm perpendicular to the central beam axis. This enabled a fast recording of the fringe field up to 500 Hz. For all simultaneous imaging and PBS irradiation experiments (Section 5.1.2) 3D magnetic fringe field data was acquired. The measured field data is reported as the difference compared to the baseline scenario in which all beamline and scanning magnets were disabled.

### 5.1.2 Image quality experiments

To characterize the effects of both the static and the dynamic fringe fields produced by the PBS beamline on the MR image quality, images of the ACR (American College of Radiology) Small Phantom (ACR Small MRI Phantom, Newmatic Medical, Grand Rapids, USA) were acquired. The phantom was positioned centrally in a dedicated knee receiver coil at the magnetic isocenter of the MRI scanner using an in-house built phantom holder (Schellhammer et al., 2018b). A spoiled gradient echo sequence (TE = 20 ms, TR = 80 ms, FA = 60°, FOV = (20 × 20) cm$^2$, asymmetric sampling = 12.5 %, phase-encoding dummies = 25, acquisition matrix = 281 × 314, Cartesian sampling, reconstructed image = 256 × 256, bandwidth = 42 Hz/px) was used to image a single transversal slice in the fluid-only region of the ACR phantom that is regularly used to quantify the image intensity uniformity and the percent signal ghosting (American College of Radiology, 2008). The GE sequence was preceded by a pre-scan frequency calibration in order to compensate for image shifts due to the thermal drift of $B_0$. The total scan time of the GE sequence excluding the pre-scan frequency calibration while including the PE dummies was 22 s. The PE dummy scans were 25 repetitions of the first line of $k$-space, which were acquired in order to assure system phase stability and were discarded during image reconstruction. The GE sequence offered a reasonable compromise between image quality and acquisition speed, but was chosen primarily because of the simple sequence structure, which helped to unravel and understand the origin of potential imaging artefacts. Operation of the proton beamline in PBS mode is a two-stage process. First, the current in the quadrupole magnets is set for the requested beam energy (and range). Then the scanning magnets are dynamically energizing to consecutively deliver the beam spots in a pre-defined pattern within the energy layer. To investigate the impact of these steps on the MR image quality, two experiments were conducted. First, a baseline experiment was performed to assess the effect of setting only the PBS beamline magnets. In the second experiment, the effect of volumetric PBS irradiation was assessed.

**Baseline experiments: Static beamline settings**

To test the hypothesis that setting the PBS beamline magnets shows no visible effect on the MR image quality, image acquisition was performed both with the beamline magnets disabled or energized. For the latter, the magnet currents were set for a beam energy of

70 MeV, 125 MeV, and 220 MeV, without the beam being transported. The scanning magnets were not energized for this experiment.

**Imaging and simultaneous volumetric proton beam scanning**

To test the hypothesis that the dynamic operation of the PBS beamline and scanning magnets during simultaneous MR image acquisition affects the image quality, the 3D volumetric radiation field was decomposed into its three components: change of energy layers (Z), horizontal (X) and vertical beam scanning (Y). The energy variation was achieved by 9 energy layers using beam energies from 220 MeV to 140 MeV, with equidistant energy steps of 10 MeV and a single central beam spot for each layer. The corresponding spot map is indicated as Z9 in the following. For both lateral scanning directions, the central X and Y axis of a 48 cm × 24 cm radiation field were scanned individually using either 9, 17, 33 or 81 equidistant spot locations. The corresponding spot maps are designated as X9, X17, X33, X81 and Y9, Y17, Y33 and Y81 in the sequel. Each of the spot maps was designed such that the total dose delivery time was 20 s. In this way, dose delivery was completed within the image acquisition time frame, while starting after the pre-scan frequency calibration to make sure the latter is not affected by dynamic beam scanning effects. To test for reproducibility, all experiments were repeated three times. The MR image quality was evaluated qualitatively and compared to the images acquired for the baseline experiment.

### 5.1.3 Theory and computer simulation

Under the hypothesis that the dynamic fringe fields of the beamline and scanning magnets change the $B_0$ field of the MRI scanner during image acquisition, implications for the data acquisition in $k$-space and the reconstructed MR images can be deduced from theoretical considerations. From textbooks (Haacke et al., 1999) it is well-known that the accumulated phase, $\Phi$, at time $t$ after initial excitation of a detected MRI signal can be expressed as:

$$\Delta\Phi(t, \mathbf{r}) = \gamma \int_0^t \Delta B_0(\tau, \mathbf{r}) d\tau, \qquad (5.1)$$

where $\Delta B_0(\tau, \mathbf{r})$ is the change in the magnetic flux density, $t = 0$ is the time of the RF excitation, $\gamma$ is the reduced gyromagnetic ratio for protons (42.6 MHz/T) and $\mathbf{r}$ is the position vector. If it is assumed that the change in the $B_0$ field is uniform over the whole FOV and

time-invariant between the initial excitation and the time of the signal echo (TE), then $\Delta\Phi$ simplifies to

$$\Delta\Phi(t) = \gamma\Delta B_0 t = \Delta f t, \tag{5.2}$$

where $\Delta f$ represents a change in central resonance frequency. Hence, a change in $B_0$ that occurs between two adjacent lines of $k$-space can be modeled as a phase ramp along the FE direction. The acquired phase error corrupted signal $S^{'}(k,j)$ for PE line $j$ is then given by (Durand et al., 2001):

$$S^{'}(k,j) = S(k,j)e^{i\Delta\Phi(t)} = S(k,j)e^{i\Delta f(j)t_k}, \tag{5.3}$$

where $S(k,j)$ is the theoretical, uncorrupted signal, $k$ is the sample number along the FE direction and $t_k$ is the time between RF excitation and sampling of the $k$th point along the FE direction. In order to resemble the time structure of the X9 spot map from the simultaneous imaging and irradiation experiments (Section 5.1.2), $\Delta f(j)$ was modeled as a function of PE line $j$ using a maximum central resonance frequency change of $\Delta f$ = 230 Hz (input taken from results of Section 5.2.1), split into 9 equidistant spots, i.e., in steps of 230/8 = 28.75 Hz from -115 Hz to +115 Hz, (Figure 5.1a). Furthermore, along FE direction, $t_k$ was modeled using the precise timing of the GE sequence, with a dwell time $t_d$ = 94.7 μs between sample points, that resulted from the sampling receiver bandwidth of the GE sequence (rBW = 10563 Hz). This resulted in the phase ramp matrix $M(k,j) = e^{i\Delta f(j)t(k)}$ shown in Figure 5.1b. Furthermore, the $k$-space of a GE image acquired during the baseline experiment was used as an approximation of the uncorrupted signal $S(k,j)$. In other words, the phase ramp matrix $M(k,j)$ was multiplied by the baseline $k$-space image. The reconstructed image resulting from the computer simulation in $k$-space was qualitatively compared to images acquired during the X9 beam-scanning experiments.
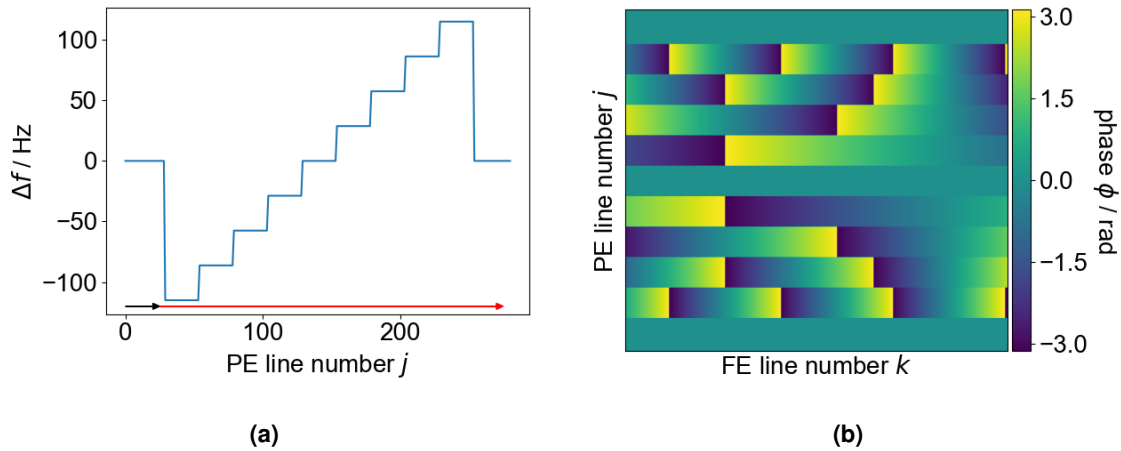
**Figure 5.1:** a) Change in central resonance frequency $\Delta f$ as a function of PE line number $j$ in $k$-space, as implemented for the simulation experiment. Black and red arrows indicate the time interval of the dummy scans (2 s) and the actual image acquisition (20 s), respectively. b) Resulting phase ramp matrix $M(k, j)$ for the simulation experiment. Figure adapted from Gantz et al. (2020).

## 5.2 Results

### 5.2.1 Magnetometry results

**Influences from the GTR and FBL beamlines**

For all gantry angles and for gantry rotation, the mean drift-corrected changes in $\Delta f_{192}$ were within 2 Hz (Figure 5.2a). Changes in MFH$_{192}$ were below 0.5 ppm. This indicates that there is no dependency on gantry angle or rotation. For the operation of the GTR beamline, i.e., the one PBS treatment plan consisting of 3 fields, a marked change in $\Delta f_{16}$ was seen (Figure 5.2b). The change in resonance frequency $\Delta f_{16}$ is energy-dependent and on the order of 25 Hz to 10 Hz for energies of 218 MeV to 100 MeV. Changes in MFH$_{16}$ were below 2 ppm for all 3 fields.

For the operation of the FBL beamline, measured changes in $\Delta f_{16}$ as a function of beam energy are given in Table 5.1. The resonance frequency changes increased with proton beam energy and were in the range of 29 Hz – 88 Hz for energies of 70 MeV – 224 MeV.

**Table 5.1:** Effects of FBL operation: Change in $\Delta f_{16}$ due to setting the FBL beamline for proton beam energies of 70 MeV – 224 MeV.

| Energy / MeV | 70 | 100 | 125 | 150 | 170 | 200 | 224 |
|---|---|---|---|---|---|---|---|
| $\Delta f_{16}$ / Hz | $28.6 \pm 1.0$ | $34.4 \pm 1.0$ | $39.3 \pm 2.4$ | $44.5 \pm 4.1$ | $52.4 \pm 1.1$ | $65.1 \pm 1.1$ | $88.2 \pm 0.8$ |
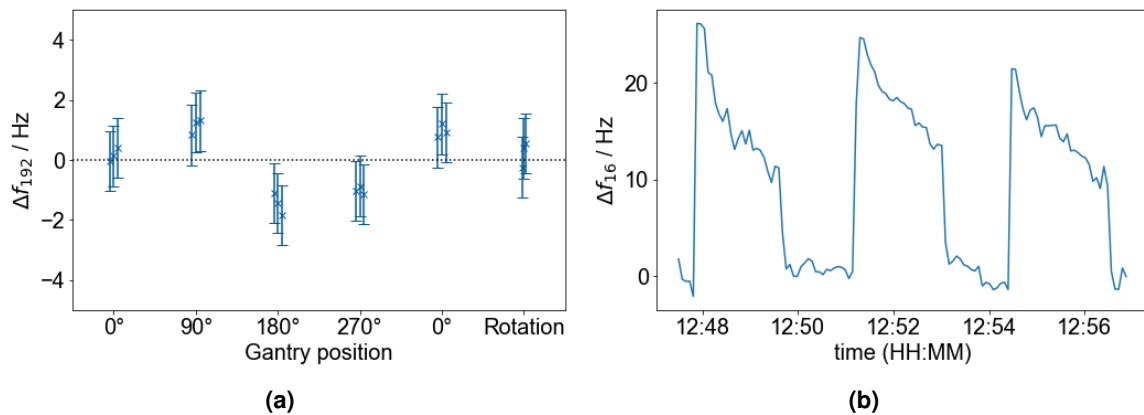
**Figure 5.2:** Effects of gantry beamline operation: (a) Drift-corrected change in $\Delta f_{192}$ due to different gantry angles and gantry rotation with all magnets off and (b) change in $\Delta f_{16}$ during delivery of a clinical PBS treatment plan consisting of 3 fields.

These results show that operation of both the FBL and GTR beamlines affect the resonance frequency and therefore the $B_0$ field of the MRI scanner, potentially leading to severe image degradation. It is therefore necessary to monitor the operation of the GTR and FBL beamlines and acquire MR images only when all beamlines are in a static setting, i.e., preferably inactivated unless the scanner is magnetically decoupled from the fringe fields.

**Effects of the PBS beamline operation**

**Magnetic field camera**    The effect of the ambient temperature induced $B_0$ field drift was compensated for by subtraction of a linear function that was fitted to the measurements of the baseline experiments. The mean frequency drift for all experiments was in the range from -0.1 Hz/min to -0.5 Hz/min. The measurements showed that the central resonance frequency $\Delta f_{192}$ monotonically increased with beam energy over a range from 18 Hz to 50 Hz when the quadrupole magnets were set to energies ranging from 70 MeV to 220 MeV (Table 5.2). The current applied to the quadrupole magnets is a monotonically increasing function of the beam energy with no discontinuities over the whole range of energies studied (data not shown). Only minor changes in the MFH$_{192}$ were measured when setting the

**Table 5.2:** Effects of PBS beamline operation: Change in central resonance frequency ($\Delta f_{192}$) as function of setting the beamline transport magnets to different proton energies.

| Energy / MeV | 70 | 125 | 170 | 220 |
|---|---|---|---|---|
| $\Delta f_{192}$ / Hz | $18.0 \pm 0.4$ | $25.4 \pm 0.4$ | $32.3 \pm 0.3$ | $50.4 \pm 0.5$ |
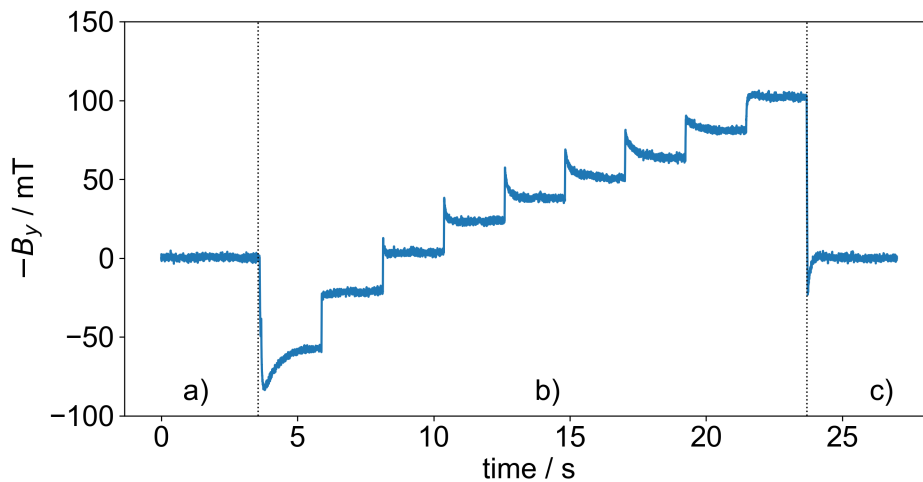
**Figure 5.3:** Change in the vertical magnetic fringe field component ($B_y$) as measured by the tri-axial Hall probe during dose delivery of the X9 spot map. Vertical dotted lines represent the transitions between the time intervals in which the magnets were set to: a) beamline magnets set for 220 MeV with scanning magnets disabled, b) operation of the scanning magnets during delivery of the X9 spot map and c) all beamline and scanning magnets disabled. Figure adapted from Gantz et al. (2020).

beamline magnets. The maximum change in MFH$_{192}$ was measured to be less than 2 ppm for a 220 MeV proton beam at a baseline MFH$_{192}$ of (109 ± 1) ppm.

During operation of the scanning magnets at maximum beam energy (220 MeV), a minor change in the central resonance frequency $\Delta f_{192}$ of (-0.3 ± 2.1) Hz and (3.7 ± 2.0) Hz was measured for the two extreme spot positions at (X = 0 cm, Y = -12 cm) and (X = 0 cm, Y = 12 cm) in vertical direction, respectively, whereas the central resonance frequency $\Delta f_{192}$ changed from (-90.8 ± 3.5) Hz to (144.0 ± 3.6) Hz for the two extreme spot positions (X = -24 cm, Y = 0 cm) and (X = +24 cm, Y = 0 cm) in horizontal direction, respectively. Absolute changes in the MFH$_{192}$ were less than 3 ppm for all measurements in both scanning directions.

**3D Hall probe** Figure 5.3 shows the time structure of the vertical component of the fringe field ($B_y$) produced by the scanning magnets during irradiation of the X9 spot map. Note, that as the $y$-axis is pointing down, $-B_y$ is reported in order to simplify the understanding of the time structure. The spot location dependent effect on the magnetic fringe field that the X-scanning magnet produced for the 220 MeV beam can be appreciated. From the baseline level, a sharp decrease of approximately 80 mT is observed that is related to spot position
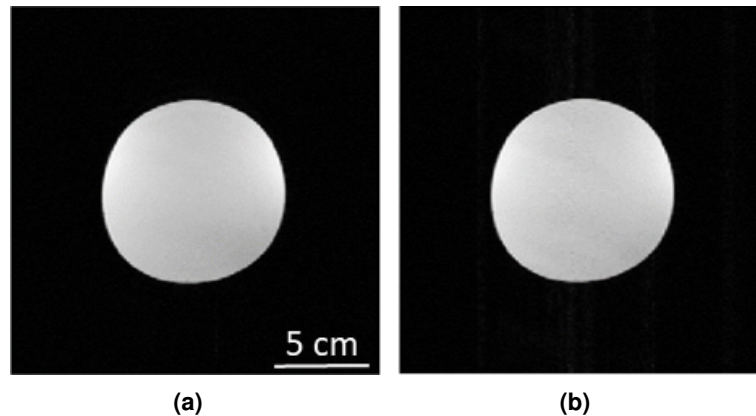
**Figure 5.4:** GRE images of an axial slice of the homogeneous region of the ACR phantom a) with all beamline magnets disabled and b) with the beam transport magnets set for 220 MeV. Figure reprinted from Gantz et al. (2020).

(X = -24 cm, Y = 0 cm) of the radiation field. Then, a stepwise increase in $-B_y$ takes place every 2.2 s until spot position (X = +24 cm, Y = 0 cm) is reached. Here, the level of $-B_y$ has increased to 105 mT, after which it returns to the baseline level immediately after the 9th dose spot has been delivered. Note that for each change in spot location a transient magnetic field effect of less than 1 s occurs. The response time of the Hall probe, including induction, is below 0.5 μs (Crescentini et al., 2017), which shows that a transient effect from the measurement device can be excluded. Thus, the observed effect is due to the settling behavior of the scanning magnet after current ramping caused by eddy currents inside the magnet. The Y9, Y17, Y33 and Y81 spot maps show a similar stepwise change in $B_x$ with an amplitude change between the first and last spot of 40 mT, whereas for the Z9 spot map no change is seen in any of the measured field components. This indicates that the Hall probe resolves fringe field changes due to settings of the scanning magnets, but is insensitive to changes in the settings of the beamline magnets.

### 5.2.2 Image quality experiments

**Baseline experiments: Static beamline settings**

Images from the baseline experiment showed no visual differences between beamline magnets disabled and beamline magnets set for a 220 MeV beam (Figure 5.4), except for a sub-voxel shift of less than 0.5 mm in FE direction, which is caused by the change in resonance frequency due to activation of the beamline magnets (Section 5.2.1) and uncertainties in
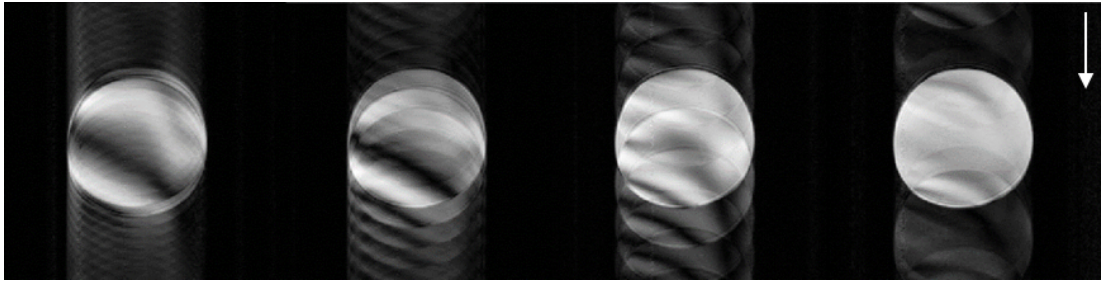
**Figure 5.5:** GE images of an axial slice of the homogeneous region of the ACR phantom acquired during irradiation of the X9, X17, X33 and X81 spot maps (from left to right) show the ghosting artefacts in PE direction (white arrow). Figure reprinted from Gantz et al. (2020).

the pre-scan frequency calibration (see Chapter 3 and (Gantz et al., 2021; Schellhammer et al., 2018b)). A similar image quality was achieved with the beamline magnets energized for 70 MeV and 125 MeV. Hence, no visual image degradation was observed due to the static settings of the beamline magnets. Consequently, the dynamic effects of PBS irradiation during imaging could be studied independently in the following.

**Imaging and simultaneous volumetric proton beam scanning**

Images acquired during irradiation of the Z9 spot map showed no visual differences to the images acquired at baseline. The same applies to the Y9, Y17, Y33 and Y81 spot maps. This shows that beam energy variation and vertical beam scanning does not deteriorate the MR image quality. The MR images acquired during horizontal beam scanning, however, clearly show coherent ghosting artefacts in the PE direction (Figure 5.5). The number of ghosts in the images decreases with increasing number of dose spots applied during image acquisition. The observed effects can be attributed to phase shifts occurring between adjacent lines in $k$-space. This is evident from $k$-space phase images (Figure 5.6a), which clearly show the 9 consecutive time intervals during which $k$-space was linearly filled while the X9 spot map was delivered.

### 5.2.3 Computer simulation

The reconstructed MR image and $k$-space phase map that were synthesized in the computer simulation experiment by $k$-space phase manipulation of a baseline image are shown in Figures 5.7c and 5.7a, respectively. Furthermore, for comparison, Figures 5.7b and 5.7d show the $k$-space phase and reconstructed magnitude image acquired during irradiation of
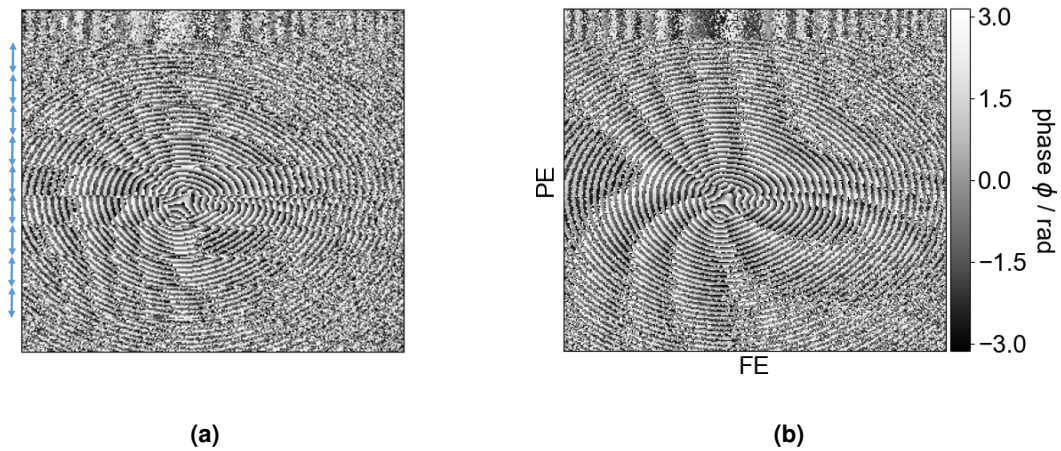
**Figure 5.6:** Phase images of the $k$-space acquired during (a) irradiation of the X9 spot map and (b) at baseline. Blue arrows on the left indicate the time interval (about 25 lines each) of each single dose spot. Since $k$-space is filled linearly from top to bottom, the first 25 lines represent the dummy scans. Figure adapted from Gantz et al. (2020).

the X9 spot map. As expected, the simulated and measured images show the same number of ghosts and similar intensity variation inside the circular object imaged. This demonstrates that the presented theory is capable to accurately describe the observed image artefacts.

## 5.3 Discussion

For the successful development of MR-integrated proton therapy, artefact-free real-time imaging during proton PBS irradiation is considered an absolute necessity for organ motion mitigation. In this chapter, a first systematic experimental investigation into the effects of simultaneous imaging and actively scanned proton pencil beam irradiation by utilizing magnetic field measurements in combination with MR imaging experiments during simultaneous irradiation on our research prototype in-beam MRI scanner were conducted. These experiments provide a comprehensive understanding of the fringe field effects of the proton beamline onto the imaging capability of this in-beam MRI scanner. Effects of the two additional beamlines, the fixed research beamline and the clinical gantry-based beamline was found to be relevant with proton energy-dependent changes in $f_{192}$ on the order of 10 Hz to 100 Hz. As a direct consequence, the MRI scanner should only acquire images when neither of the of the two beamlines are operated. This also requires a detailed logging of beamline operations, and for future clinical application, a dedicated workflow incorporating
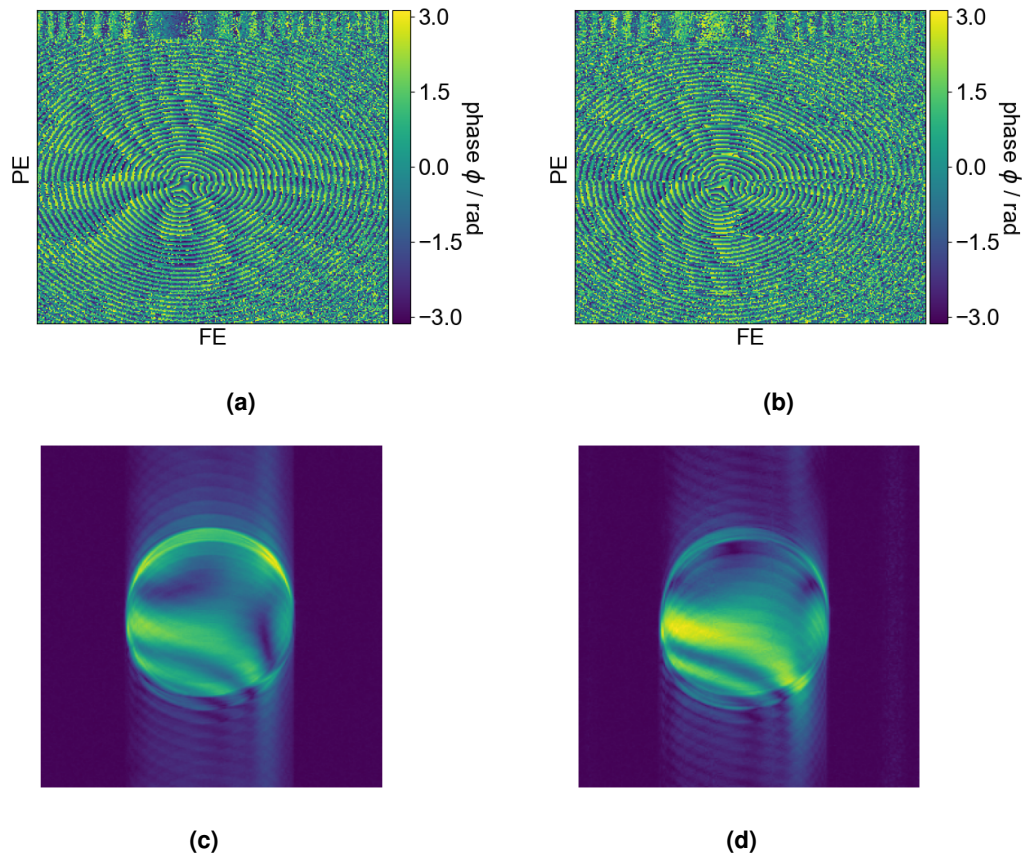
**Figure 5.7:** Simulated $k$-space phase (a) and magnitude (c) image resulting from the computer simulation experiment. Measured $k$-space phase (b) and magnitude (d) image acquired during irradiation of the X9 spot map. Figure adapted from Gantz et al. (2020).

activities in both rooms. Baseline experiments at the PBS beamline showed that the static operation of the beamline magnets do not compromise the MR image quality independent of proton beam energy. The results have shown that proton energy dependent settings of the beamline magnets change the MRI frequency by 18 Hz to 50 Hz and have no effect on image quality other than the already known image shift in FE direction (Gantz et al., 2021; Schellhammer et al., 2018b), which can be compensated for by a pre-scan frequency calibration to a sub-pixel shift below 0.5 mm.

Dynamic operation of the PBS beamline revealed that changing the proton beam energy in 9 equidistant energy steps from 220 MeV to 140 MeV resulted in a total change in $f_{192}$ on the order of 20 Hz. This corresponds to a change in $f_{192}$ of about 2 Hz between adjacent energy layers. Imaging experiments have shown no degradation in image quality while changing the energy layers. Here, it is important to note that the time to change energy

layers is about 2 s, which implies that the change in $f_{192}$ does not occur between individual lines of $k$-space but instead is distributed over about 25 lines, thus resulting in a much lower frequency change per line. Furthermore, since for clinically relevant dose distributions the typical energy layer step size is well below 10 MeV (Alshaikhi et al., 2019) the effect is further reduced. For vertical beam scanning along the direction of the $B_0$ field, the magnetic field camera measurements showed a total change in $f_{192}$ of 4 Hz between extreme spot positions of the radiation field. For the Y9 spot map, the spot-to-spot change in $f_{192}$ was well below 1 Hz. Accordingly, the acquired MR images showed no degradation in image quality. Horizontal beam scanning showed a much stronger effect on $f_{192}$, with a maximum frequency change of 235 Hz between the two extreme spot positions of the radiation field. For the X9 and X81 maps, the spot-to-spot resonance frequency change was on the order of 30 Hz and 3 Hz, respectively. As the time to change between spots is on the order of 1 ms to 2 ms, this change in frequency was expected to result in phase changes between adjacent lines in $k$-space. The computer simulation experiments confirmed this presumption by showing that severe ghosting artefacts occurred in MR images that were reconstructed from perturbed phase maps in $k$-space. MR images acquired during $B_0$ field perturbations due to the horizontal beam scanning showed the same severe artefacts, with the number of ghosts being dependent on the spot scanning frequency. This is consistent with previous findings showing that the number of coherent PE ghosts increases when decreasing the number of $k$-space discontinuities (Zhuo & Gullapalli, 2006).

Based on the results from the 3D volumetric irradiation experiments it was concluded that for frequency changes down to 3 Hz between lines in $k$-space ghosting artefacts occur, whereas for changes on the order of 1 Hz or below no visual change in image quality as compared to the baseline could be observed. This result agrees well to the study by Hofman et al. (2013) that investigated magnetic interaction between an MRI system and a nearby cyclotron and concluded that for $T_2^*$-weighted gradient echo imaging blurring in the PE direction would occur for phase changes larger than TE $\cdot \Delta f$ = 0.05. For this investigation, with TE = 20 ms this translates to a frequency change of 2.5 Hz. The spot maps used in this study were designed to have a simple energy layer and spatio-temporal structure, which allowed a systematical examination of the image artefacts due to dynamic dose spot delivery. For clinically representative spot maps, dose application per energy layer is much faster and the spatio-temporal structure per layer will be more complex. As the periodicity inherent in the spot maps used for this study is lost for clinical spot maps, image blurring

along the PE direction is expected to occur instead of coherent ghosts that degrade the image quality.

To understand the differences in the magnetic fringe field effects produced by the vertical and horizontal scanning magnets, their geometry and field orientation needs to be taken into account. The main magnetic field of the horizontal scanning magnet is parallel or anti-parallel to the $B_0$ field of the MRI scanner, whereas the main field of the vertical scanning magnet is perpendicular to the $B_0$ field. Addition of a field perturbation parallel to the $B_0$ vector will result in a larger change in its magnitude than adding a field perturbation of the same strength that is perpendicular to the $B_0$ vector. Thus, the change in resonance frequency is expected to be larger for the superposition of the fringe field produced by the X scanning magnet onto the $B_0$ field than by that of the Y scanning magnet. Apart from this field superposition, the high magnetic permeability of the iron flux return yoke of the magnet could lead to an increase in the absorbed magnetic energy by the external fringe fields. Computer modeling studies are needed to understand the complex magnetic coupling underlying this hypothesis. In addition to this, the horizontal scanning magnet is located downstream of the vertical scanning magnet. Hence, the gap between the magnet poles is wider for the X scanning magnet than for the Y scanning magnet, to allow beams deflected in Y direction to pass (Farr et al., 2013). This results in a less confined magnetic field and consequently in a stronger fringe field, as confirmed by the Hall probe measurements. Maximum differences in the fringe fields of the horizontal and vertical magnets were 180 mT and 40 mT between extreme spots in horizontal and vertical direction, respectively. The synergistic effects of the geometry and field orientation of the scanning magnets explain why the fringe field of the horizontal scanning magnet has a stronger effect on $f_{192}$ than that of the Y scanning magnet, even though their distances from the MRI scanner as well as their maximum field strengths are almost the same.

The fact that the observed image ghosting artefacts originate from phase changes in $k$-space has been demonstrated by theoretical considerations and computer simulations. In theory, these phase changes can be deduced from the known time structure of the spot map and the spot-position dependent change in the resonance frequency. Hence, to compensate for this effect, it would be obvious to reverse the phase changes. However, this would require a synchronization between dose spot delivery and $k$-space filling, as well as a fast and precise online measurement of the central resonance frequency, to a precision of about 1 Hz (about 20 nT) or better. Additionally, a generalization of the presented theory

should be included to account for frequency changes occurring during acquisition of a single FE line. However, this effect is assumed to be very small compared to the PE ghosting seen in this study. Other potential measures to eliminate the image artefacts due to the dynamic fringe field of the X scanning magnet would need hardware or software solutions. In the former case, magnetic decoupling between the beamline and the MRI scanner should be realized to suppress dynamic perturbations in the $B_0$ field, whereas in the latter, online or offline image correction strategies should be implemented. For magnetic decoupling both active and passive shielding techniques should be considered. For the latter, magnetic modeling will be the key in ascertaining the effectiveness of such an approach (Whelan et al., 2018). Online corrections should evaluate the central resonance frequency at every signal acquisition. This can possibly be achieved through a navigator-echo approach (Butts et al., 1994; Li et al., 2009; McGee et al., 2000). Offline corrections are expected to be based on either an optimization process to correct phase errors between PE lines (Broche et al., 2017) or a deep-learning based image correction approach (Küstner et al., 2019) based on a large set of corrupted and uncorrupted images. Further research is mandatory to determine which of these measures is most promising. In this regard, it is important to highlight that the change in central resonance frequency does not only affect the phase along the PE direction in $k$-space, but has additional effects on the image acquisition, such as a shift in slice position that will be relevant for anatomical imaging. Therefore, magnetic shielding or online frequency evaluation strategies are expected to be potentially advantageous over corrections applied to image reconstruction.

The current study provides first experimental evidence that simultaneous MR imaging and dynamic PBS proton irradiation is not feasible without degradation of image quality. This seems to contradict the conclusion of the only magnetic modeling simulation study present to date (Oborn et al., 2016). However, this study only investigated the magnetic fringe field effects of the scanning magnets of a typical PBS beamline assembly on the $B_0$ field homogeneity of the 1 T split-bore MRI system of the Australian MRI-Linac program from first principles. The results presented here are consistent with the findings of Oborn et al. (2016), in that changes in MFH are small and not relevant for geometrical distortion of MR images. However, the simulation study did not investigate the effects on MR image formation. The results of the current study, on the other hand, have revealed that severe image ghosting artefacts originate from the phase changes caused by dynamic perturbations in the $B_0$ field due to the operation of the X scanning magnets.

This study is subject to a number of limitations. Firstly, the single-slice GE sequence was deployed because of its simple pulse structure, which helped to unravel the origin of the ghosting artefacts. Although this sequence provides a generally good compromise between image quality and acquisition speed, its acquisition time of 22 s is too long for real-time imaging. Balanced steady-state free precession (bSSFP) sequences are generally used on hybrid MR-linac systems for 2D cine-imaging, as they provide the necessary acquisition speed, a favorable $T_2/T_1$ contrast and high SNR (Klüter, 2019; Raaymakers et al., 2017; Scheffler & Lehnhardt, 2003; Tyler et al., 2006). Typically, bSSFP sequences have repetition times on the order of a few ms, which allows for single-slice frame rates up to 4 Hz − 8 Hz. Navigator-echo-based image correction approaches seem unfeasible, as they would prolong the TR and thus reduce the frame rate of bSSFP sequences used for cine-imaging. This would imply that magnetic shielding could be a more promising option to reduce $B_0$ field perturbations during PBS irradiation. Secondly, the time resolution of the magnetic field camera was too low to resolve changes in the $B_0$ field due to the time structure of the spot maps, as the time between dose spots is on the order of 1 ms − 2 ms, while the camera has a time resolution of 5 s. Therefore, I investigated the $B_0$ field changes caused by spot-dependent settings of the scanning magnets in a static operation for each spot individually and used the Hall probe which has a high sampling rate (500 Hz) and was placed close to the scanning magnets to resolve the time structure of the dose spot irradiation. Thirdly, as the MRI scanner is movable, its absolute position is subject to a re-positioning uncertainty of ± 10 mm in both X and Z direction. However, the influence of this positional uncertainty on both the magnetometry and imaging results were found to be negligible.

A different aspect regarding the integration of MRI and PT is the energy-dependent proton beam deflection caused by the static imaging and fringe fields of the MRI scanner. Although this is beyond the scope of this thesis, reference is made to previous computer simulation studies showing the dosimetric effects of a uniform transversal magnetic field in water phantoms and patient geometries (Fuchs et al., 2017; Hartman et al., 2015; Moteabbed et al., 2014; Raaymakers et al., 2008), as well as the dosimetric effects of realistic MRI fringe fields (Oborn et al., 2015). A first experimental validation showed that magnetic field induced proton beam deflection is accurately measurable and predictable (Schellhammer et al., 2018a). A recent treatment planning study by (Burigo & Oborn, 2019) has demonstrated that beam deflection can be adapted for precisely by intensity-modulated proton

therapy in the presence of a realistic inline MR fringe and imaging field. For the experimental setup used in the current study, lateral beam deflections were 2.6 cm, 1.9 cm and 1.5 cm measured at the magnetic isocenter of the MRI scanner relative to the central beam axis for respective beam energies of 70 MeV, 125 MeV and 220 MeV (Section 4.3). Since this chapter only focuses on the imaging aspects, beam deflections were not considered.

As future MRiPT systems might require an MRI scanner to be integrated in a rotating gantry to facilitate beam access to the patient from different angles, the MRI magnet design may differ from that of the gantry-less in-beam MRI system used in the current study. Nevertheless, it is expect that the findings of the current study are at least partially transferable to a gantry-based system, as long as its beamline has downstream scanning magnets that have a similar geometry to that used in the current study. A magnetic decoupling of the PBS system and the MRI scanner most probably remains indispensable. However, the optimal MRI magnet design is subject to ongoing research. For an inline field orientation with the beam directed parallel to the $B_0$ field, the magnetic fringe field effects on the MRI resonance frequency are expected to be reduced relative to a cross-line orientation with the beam directed perpendicular to the $B_0$ field, since the fringe fields of both the X and Y scanning magnets would be perpendicular to the $B_0$ field, as was only the case for the Y scanning magnets in the current study. From a dosimetric point of view, an inline orientation is expected to cause significant beam rotation, whereas more complex beam deflection and distortions have been reported for the perpendicular orientation (Oborn et al., 2015). Nevertheless, a recent treatment planning study by Burigo and Oborn (2019) has shown for the first time that dose distributions to be delivered with state-of the-art intensity-modulated proton therapy can be optimized to account for the presence of an inline MRI fringe field. This promising result stimulates further research into the technical challenges and developments required to bring the concept of MRiPT into clinical reality.

# 6 Proton beam visualization by online MR imaging: Unravelling the convection hypothesis

One of, if not the decisive benefit of proton therapy over conventional X-ray therapy is the ability to confine the radiation doses to the tumor, because of the presence of the Bragg peak. The precision of the treatment, however, is currently still limited by the uncertainty in the proton beam range (Takayanagi et al., 2020). In order to improve the precision of proton therapy it would therefore be extremely desirable to verify the proton range in-vivo, either prior to, during, or after therapy (Knopf & Lomax, 2013). Several concepts, including proton radiography and tomography (Sarosiek et al., 2021), prompt gamma imaging and timing (Richter et al., 2016; Werner et al., 2019), ionoacoustic tomography (Kellnberger et al., 2016; Takayanagi et al., 2020), PET imaging (Lopes et al., 2016; Paganetti & Fakhri, 2015) and even offline MRI (Yuan et al., 2013) have been proposed to achieve in-vivo range verification for proton therapy. However, none of these methods is capable to visualize both the proton beam end-of-range and the patient anatomy. Therefore, the unique opportunity of a first experimental integrated MRI and proton therapy setup built in 2017 (Schellhammer et al., 2018b), allowed to investigate the possibility of online proton beam visualization using MR imaging. A first exploratory study (Schellhammer, 2019), revealed the potential to visualize the proton beam in various liquid materials, such as water and oil. However, as the effect could not be reproduced in solid media and a relatively high dose threshold was necessary to visualize the beam, the hypothesis of proton beam induced local heating that causes a buoyancy driven flow or convection was raised. Therefore, to further investigate the potential of online MRI based proton beam visualization, this chapter aims to test the convection hypothesis using a novel MRI sequence, specifically tailored to test convection. The designed MRI sequence is tested for a beam-induced change of MRI signal under variation of the proton beam energy and current. Furthermore, by introducing vertical capillaries and selectively closing compartments the effect is studied under flow restriction and inhibition, respectively. Finally, externally introduced flow in a tube is studied as a comple-
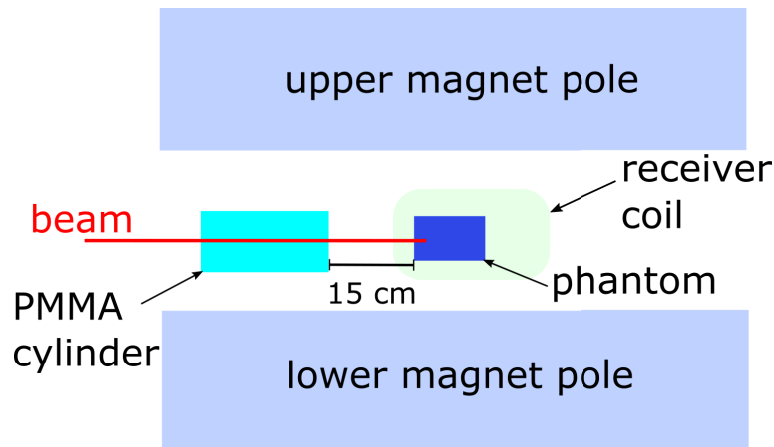
**Figure 6.1:** Schematic of the experimental setup for the beam visualization experiment. The water filled phantom is centrally positioned in the knee coil and phantom holder, with the PMMA cylinder for range shifting at 15 cm upstream of the phantom.

mentary experiment, to demonstrate that a similar change in MRI signal can be created by water flow.

## 6.1 Material and methods

### 6.1.1 Experimental setup

For this study, the 0.22 T open MRI scanner was positioned at the horizontal fixed beamline (see Section 3.1.1). The MRI scanner was initially positioned identical to all measurements described in Chapter 3. The choice of performing this experiment at the fixed beamline, rather than the PBS beamline was motivated by (1), the intend to follow-up on previous experiments performed by S. Schellhammer, J. Pawelke, L. Karsch, A. Hoffmann and myself and initially published by Schellhammer (2019) and (2), the extended flexibility of applicable beam parameters at the fixed beamline in comparison to the PBS beamline. Here, especially the option to vary the beam current over a wide range in continuous irradiation without the need of dedicated irradiation plans, was a decisive argument. The lateral position of the MRI scanner relative to the central beam axis was adapted by a lateral shift of $\Delta x = 13$ mm to assure that a 200 MeV proton beam would centrally impinge on the phantom that was centrally positioned inside the FOV of the MRI scanner. The relative position of beam and phantom was verified using radiochromic EBT3 film (see Figure 6.3).

From previous experiments (Schellhammer, 2019), it was known that high beam currents

(> 9 nA) are required to visualize the proton beam. Highest beam currents (up to 80 nA), however, can only be achieved for the upper end of range of clinical proton beam energies available at the system, as for lower energies, the transmission in the energy selection system is decreasing rapidly. Therefore, to make the beam stop inside a phantom that can simultaneously be imaged, a range shifter had to be used, in order to reduce the residual proton beam range. Using the standard imaging setup with the dedicated phantom holder and knee receiver coil allows a maximum phantom diameter of $\approx 10 \, \text{cm} - 15 \, \text{cm}$. A 20 cm long cylindrical polymethyl methacrylate (PMMA) range shifter with a diameter of 15 cm was positioned such that its distal end is at a distance of 15 cm from the proximal end of the phantom (see Figure 6.1).

**MRI phantom and insets**

The choice of the MRI phantom for the convection experiments was motivated by two reasons. Firstly, the phantom should allow all experiments to be performed in the same setup, to guarantee comparability of the results. Secondly, the phantom needed to fit into the knee receiver coil and be centrally aligned with the proton beam, while simultaneously providing space for an external tubing and a u-shaped tube for experiments introducing external flow. These requirements were met by a water-filled container, made of high-density polyethylene (HDPE). Nominal outer dimensions were $(100 \times 100 \times 65) \, \text{mm}^3$ and the wall thickness was 1 mm. For the flow restriction experiments, a 15 mm thick PMMA inset featuring $(7 \times 7 - 1) = 48$ capillaries with a diameter of 10 mm, shown in Figure 6.2b was constructed. The inset can be reproducibly positioned inside the phantom by a set of four small plastic legs in the lower corners. The top left capillary is spared to assure reproducible positioning of the plate and provide a reference of orientation. Additionally, two 1 mm thick flow restriction plates were constructed, to selectively inhibit the flow in each second capillary using two complementary checkerboard-like hole patterns, see Figure 6.2b. Figure 6.2a shows the phantom and a second lid with a glued-in u-shaped tube that was used for the experiment introducing external flow. For all experiments, the phantom was centrally positioned in the knee receiver coil at the MRI isocenter. Beam alignment was verified using an EBT3 film that was fixed at the proximal end of the phantom, as well as an ionization chamber (PTW 34045, Advanced Markus® Chamber, PTW Freiburg, Germany).
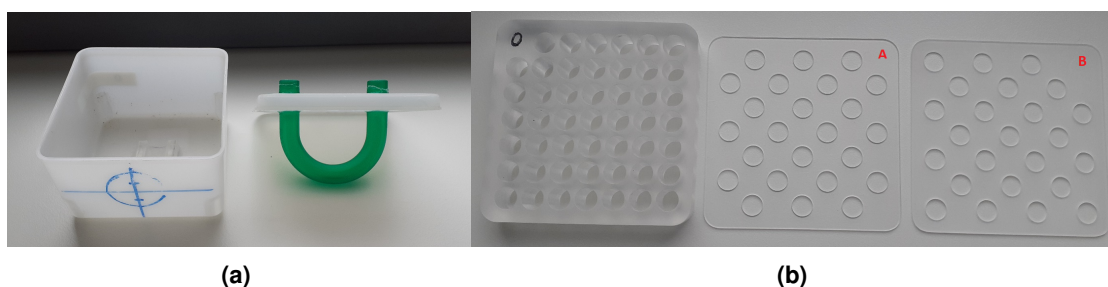
**Figure 6.2:** (a) Photography of (left) the HDPE phantom used for the beam visualization experiment with the lid removed and the position of the advanced Markus chamber marked in blue, and (right) the second lid, with a u-shaped tube inset for the external flow measurements. (b) From left to right: Photography of the capillary inset that is horizontally positioned in the midplane of the phantom, as well as the two flow inhibition plates A and B, to selectively close each other flow capillary.

**Dose rate calibration**

As the monitor chamber at the beam exit window of the horizontal fixed research beamline is known to saturate for high beam currents the dose rate had to be measured independently. To be able to estimate the dose delivered into the phantom during the irradiation experiment, the beam current was calibrated to a dose-rate measured using the exact same setup as in the main experiments, with the Advanced Markus® Chamber attached to the proximal end of the phantom. The chambers position was marked in blue on the container (see Figure 6.3a). The beam current was varied over a range of 0.5 nA to 64 nA, with irradiation times of 30 s to 5 s, receptively. The ionization chamber dose readings were normalized to the irradiation time, and thus yield an estimate of the dose rate applied.

### 6.1.2 MRI sequence design

An MRI pulse sequence was designed in order to test the convection hypothesis. Under the assumption that the proton beam locally heats the water, and thus induces a buoyancy driven flow, the water is expected to flow upwards. As common in time-of-flight (TOF) angiography (Angio) MR imaging, the flow is visualized by either pre-saturating all static spins in the imaging slice or pre-saturating spins in a thicker slab directly above or below the imaging volume (Nayak et al., 2001; Saloner, 1995). The latter approach was chosen here. A spoiled fast gradient echo sequence using an echo time of TE = 7 ms and a repetition time of TR = 19.2 ms (a full list of sequence parameters is given in Appendix B.2) was chosen with a 4 cm wide pre-saturation slab added directly below the imaging slice, such that

all spins flowing upwards into the imaging volume should be saturated and shall thus give no MRI signal.

### 6.1.3 Baseline experiments: Validation of beam energy and current dependency

A baseline experiment was performed in order to validate that the newly designed sequence can accurately reproduce previous findings that the beam-induced effect is both current- and energy-dependent (Schellhammer, 2019). Therefore, a standardized irradiation and imaging protocol was designed. The proton beam irradiation was set to a total irradiation time of 20 s starting 15 s prior to imaging, in order to allow a dose/energy deposition build-up in the water phantom. The Angio TOF MRI sequence has a duration of 3 s and therefore completed 2 s before the end of irradiation. The experiment was performed using 3 proton beam energies (200 MeV, 207 MeV and 215 MeV) as well as 4 different proton beam currents (8 nA, 16 nA, 32 nA and 64 nA).

**Estimation of residual proton beam range**

The residual expected proton beam ranges in the phantom for the three proton beam energies used for this experiment will be estimated in this paragraph. From previous investigations it is known that the nominal energies, $E_{\mathrm{N}}$, being used at the fixed research beamline can not be directly converted to residual range using one of the standard libraries, such as PSTAR (Seltzer & Bergstrom, 1993). Range calibration measurements performed by S. Schellhammer and P. Wohlfahrt were therefore taken as the basis for residual ranges in water, $R_{\mathrm{w}}$. Furthermore, all material in the beam path between the beam-exit window and the water inside the phantom had to be taken into account. These materials included: (1) the 0.12 mm copper foil closing the RF cage, (2) the 20 cm PMMA range shifter, (3) (80 ± 5) cm of air, and finally (4) the 1 mm HDPE phantom wall. For the copper foil and air, the range differences, $\Delta R$, were calculated following the approach presented in (Zhang & Newhauser, 2009):

$$\Delta R = \frac{\overline{(S/\rho)}_{\mathrm{m}}\rho_{\mathrm{m}}}{(S/\rho)_{\mathrm{w}}\rho_{\mathrm{w}}}t_{\mathrm{m}}, \tag{6.1}$$

where $\rho_{\mathrm{m}}$ is the material mass density, $\overline{(S/\rho)}_{\mathrm{m}}$ is the mean proton mass stopping power of the material, and $t_{\mathrm{m}}$ is the thickness of the material. For both air and copper, the radi-

**Table 6.1:** Estimation of expected residual proton beam ranges in water ($R_{\mathrm{res}}$) as a function of nominal energy ($E_{\mathrm{N}}$).

| $E_{\mathrm{N}}$ / MeV | $R_{\mathrm{w}}$ / cm | $R_{\mathrm{res}}$ / cm |
|---|---|---|
| 200 | 26.30 | $2.85 \pm 0.2$ |
| 207 | 27.93 | $4.48 \pm 0.2$ |
| 215 | 29.79 | $6.34 \pm 0.2$ |

ologically "thin material" approximation is used. Hence, instead of a mean mass stopping power, a single value for the initial proton beam energy ($E_0 = 200\,\mathrm{MeV}$) is used from PSTAR (Seltzer & Bergstrom, 1993). For the plastics (2) and (4), for simplicity of the calculation, the 1 mm HDPE phantom wall thickness was approximated by 1 mm of PMMA. For the resulting thickness of PMMA, $t_{\mathrm{PMMA}}$, of 20.1 cm, the range difference was estimated using a water equivalent path length of $1.1593 \pm 0.007$ resulting in a range loss of ($23.3 \pm 0.15$) cm. The water equivalent path length value was experimentally determined for clinical QA (quality assurance) purposes and kindly provided by D. Kunath. The mass densities of PMMA, air, copper and water were estimated as $\rho_{\mathrm{PMMA}} = 1.183\,\mathrm{g/cm}^3$, $\rho_{\mathrm{air}} = 0.001\,\mathrm{g/cm}^3$, $\rho_{\mathrm{Cu}} = 8.96\,\mathrm{g/cm}^3$ and $\rho_{\mathrm{water}} = 1.00\,\mathrm{g/cm}^3$, respectively. The resulting residual ranges in the phantom, $R_{\mathrm{res}} = R_w - \Delta R$, are given in Table 6.1, where the overall uncertainty due to the used approximations and setup uncertainties were estimated to be about 2 mm.

**Estimation of convection velocity caused by proton beam induced local temperature increase**

The measurements using an externally introduced flow are performed to investigate whether water flow can reproduce a similar MRI signal change as observed during proton beam irradiation. For the externally introduced flow, the flow velocities can be measured precisely, however this will not be possible for the experiments with high dose proton beam irradiation. Therefore to compare the two independent experiments, a convection velocity as induced by the local heating if the proton beam will be estimated in this section. Proton beam irradiation leads to a deposition of energy in water, that ultimately leads to a local increase in temperature. This temperature increase $\Delta T$ can be expressed as $\Delta T = D/c_{\mathrm{w}}$ = 0.24 mK/Gy, where $D$ is the dose deposited and $c_{\mathrm{w}} = 4.2\,\mathrm{kJ/(kgK)}$ is the specific heat capacity of water. This local increase in temperature results in a change of the density of water $\Delta\rho(T_0) = \rho(T_0) - \rho(T_1) \approx \rho(T_0)(1 - e^{(-\Gamma(\Delta T))})$ where $T_0$ is the temperature of the

water in the phantom, and $\Gamma$ is the volumetric thermal expansion coefficient (Demtröder, 2015). Resulting from this change in density, the heated volume experiences a buoyancy force (i.e. up-thrust), that leads to a local upward motion of the water. The velocity of this motion can be estimated using the falling ball model based on Stokes' law, by assuming the heated volume to be a sphere. The resulting velocity is then $v = \frac{2}{9}\frac{\Delta\rho}{\mu}gR^2$, (Demtröder, 2015) where $R$ is the radius of the sphere, $g$ is the gravity of earth and $\mu(T_0)$ is the dynamic viscosity of water. Input parameters for this calculation are the initial temperature $T_0$ of the water in the phantom, the dose $D$ delivered and the radius $R$ of the sphere. These parameters have to be determined experimentally.

### 6.1.4 Flow restriction and inhibition

**Flow restriction to vertical capillaries**

To test the convection hypothesis, the water flow in the MR imaging plane was restricted to the vertical direction only. The reasons are twofold, firstly the horizontally acquired MRI sequence was expected to be sensitive to out-of-plane flow (i.e. vertical) only and secondly, the beam induced flow is expected to result in a local upward motion, and thus restricting to purely vertical capillary flow suppresses diffuse flow dissipation in the horizontal plane. This was achieved by the insertion of the 15 mm thick PMMA flow restriction inset (Figure 6.2b). MR images were acquired using the same protocol as for the baseline experiment, using proton beam energies of 200 MeV, 207 MeV and 215 MeV at a constant beam current of 64 nA.

**Selective flow inhibition**

By adding either one of the two 1 mm thick flow inhibition plates A or B (see Figure 6.2b) onto the flow restriction inset, the vertical upward flow was selectively inhibited in each second capillary. The complete experiment, including all three proton beam energies, was repeated with either of the two plates installed to investigate the effect of inhibited flow on the proton beam induced MRI signature.

**Table 6.2:** Calibration of the pump flow setting to mean flow velocity $v_{\text{flow}}$ in the u-shaped tube.

| pump flow setting / (a.u.) | mean flow velocity $v_{\text{flow}}$ / (cm/min) |
| :---: | :---: |
| 35 | $39.9 \pm 0.3$ |
| 20 | $22.5 \pm 0.5$ |
| 10 | $11.5 \pm 0.5$ |
| 5 | $5.4 \pm 0.2$ |
| 2 | $2.0 \pm 0.3$ |
| 1 | $0.9 \pm 0.1$ |
| 0.7 | $0.7 \pm 0.1$ |
| 0.35 | $0.3 \pm 0.1$ |

### 6.1.5 External flow measurements

**Setup and flow rate calibration**

External capillary flow was generated using an Ismatec™ IPC 4 (Cole-Parmer GmbH, Wertheim, Germany) peristaltic pump. For all experiments, all four channels of the pump were used in parallel operation using silicone tubing with an inner diameter of 2.4 mm. The tubes were connected by standard Y-connectors and then connected to a 7 mm inner diameter PVC (polyvinyl chloride) tubing (Nalgene™, Thermo Scientific™) that was guided inside the RF cage through an additional wave guide installed next to the filter panel. Finally, the tubing was connected to the u-shaped tube in the phantom lid using an intermediate 12 mm inner diameter PVC tubing. Both ends of the tubing system were connected to a large (10 l) water reservoir and the whole tube system was then filled with water and all remaining air was removed to assure consistent flow conditions. The pump features flow rate settings ranging from 0.35 to 30 (unit less arbitrary values) which were calibrated to mean volumes per time unit by continuous operation of the pump in both flow directions for 1, 2 or 4 minutes, depending on the flow rate. The transported volumes were measured using either 10 ml, 25 ml, 50 ml or 100 ml graduated cylinders. The measurement uncertainty was estimated by considering both the systematic uncertainties from the scales of the graduated cylinders, as well as a statistical uncertainty that was evaluated by a three-fold repetition of each of the calibration measurements. Furthermore, the volume per time unit was converted to mean flow velocity $v_{\text{flow}}$ in the u-shaped tube, by dividing by the tubes cross-sectional area ($3.14 \, \text{cm}^2$). The resulting calibration is presented in Table 6.2.
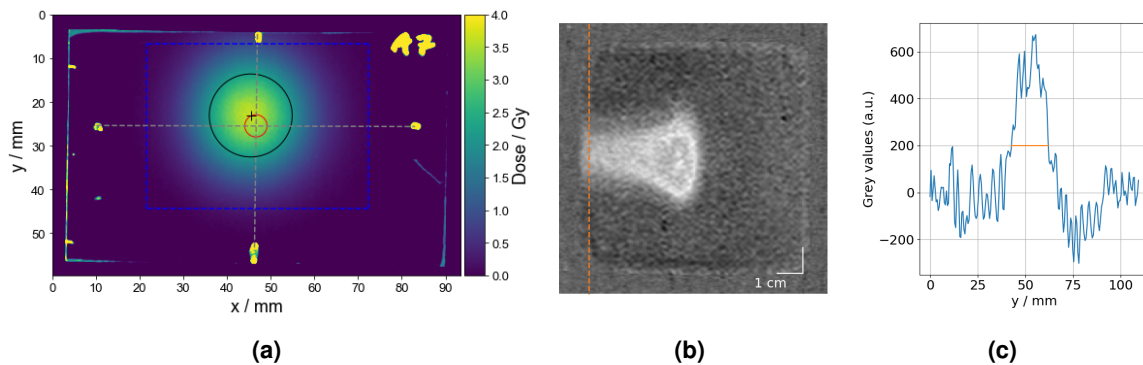
**Figure 6.3:** (a) Dose evaluation of the EBT3 film at the proximal end of the phantom. The grey lines indicate the crosshair as marked on the phantom, the blue rectangle show the area used for the 2D Gaussian fit for the beam spot size, the black circle and cross denote the $1\sigma$ beam size and center, respectively. Additionally, the active measurement area of the advanced Markus chamber used for beam-current to dose calibration is marked by the red circle. (b) Difference image between beam signature at 207 MeV and 32 nA and reference (no beam), the orange line indicates the position of the lateral profile. (c) Lateral profile of the difference image of the MRI signature (blue) and estimate of the beam-width (orange).

**External flow measurements**

This experiment aims to test the convection hypothesis and to demonstrate that a similar MRI signal loss as shown under proton beam irradiation can be produced by externally introduced flow in a tube perpendicular to the MR imaging plane. Therefore the peristaltic pump was operated continuously using the full range of flow settings, between 0.35 and 30 (a.u.). As the diameter of the tubing running through the pump is much smaller than the diameter of the tube in the phantom, and the transported volume per stroke of the pump is extremely small, i.e. the flow is mainly driven by an increase of the stroke speed of the pump, the resulting flow in the u-shaped tube can be considered to be continuous. The experiment was performed to study both flow directions independently. For each measurement, first the pump was started, with the MR image acquisition starting 15 s later. This procedure was chosen to minimize any initial transient effects from starting the external flow. The pump was stopped after the MR image acquisition was terminated and sufficient time ($\approx$ 1 min) was given for the water to settle before the next measurement. This was verified by the acquisition of reference MR images in between flow measurements, which were visually inspected to assure that the signal in both arms of the tube was similar to the background water signal in the phantom.
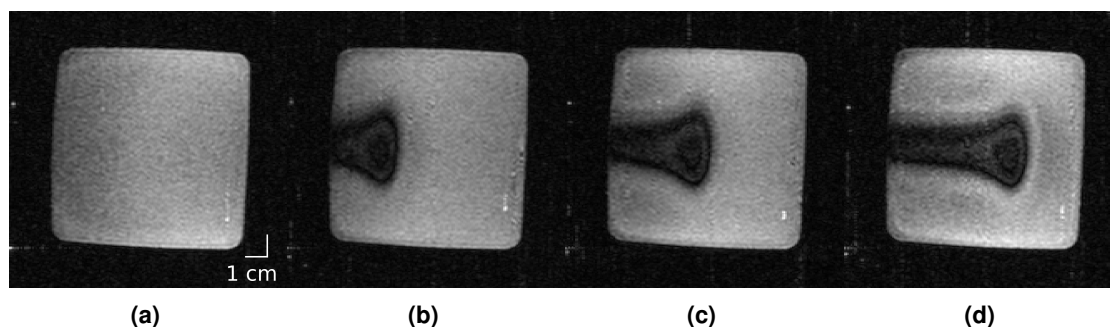
**Figure 6.4:** Angio TOF MR images showing the beam energy and range dependency of the signature: (a)-(d) were acquired during irradiation using 32 nA and 0 MeV, 200 MeV, 207 MeV and 215 MeV, respectively.

## 6.2 Results

### 6.2.1 Baseline experiments

**Verification of proton beam position and comparison of lateral beam width**

Figure 6.3a shows the absolute dose evaluation of the EBT3 film that was irradiated while being attached to the proximal end of the MRI phantom. It shows that the beam center has an offset from the marked cross-hair of 1.2 mm and 2.4 mm in horizontal and vertical direction, respectively. This verifies that the active area (red circle in Figure 6.3a) of the ionization chamber used for dose-calibration was sufficiently covered by the beam. A 2D Gaussian fit of the beam profile yielded a $1\sigma$ width of 9.2 mm and 9.7 mm in horizontal and vertical direction, respectively. This translates to a mean FHWM of the pencil beam at phantom entry of 22.3 mm. This beam width can be compared to the beam width estimated from the Angio TOF MR images. Figure 6.3b shows a difference image between an MR image acquired during irradiation using 207 MeV and 32 nA and a reference image acquired without beam. The orange dotted vertical line denotes the position of a vertical profile which was used to estimate the beam width in the MR image to be 19.7 mm (Figure 6.3c). However, for irradiation at 64 nA the beam width estimated from the MR image was 24.2 mm. This difference can be understood by the current-dependency of the MRI signature, see page 69 and Figure 6.6.
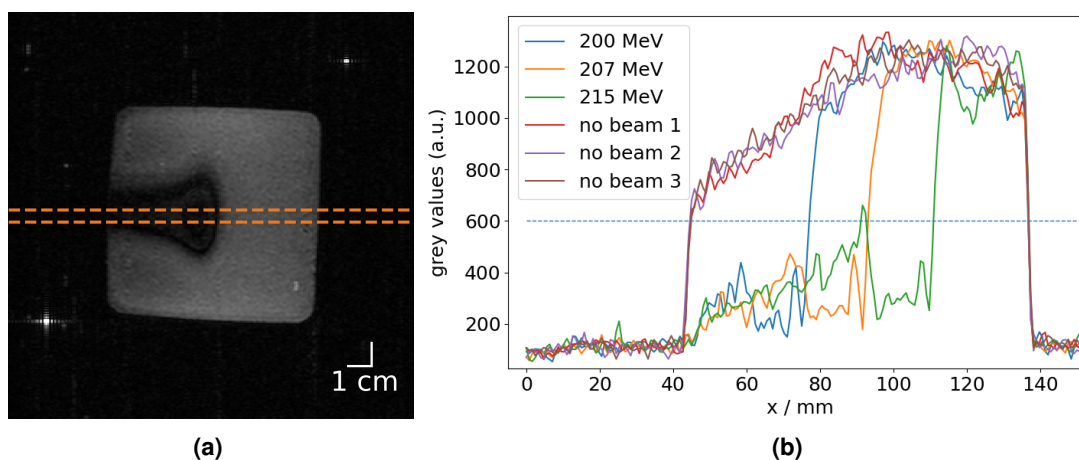
**Figure 6.5:** (a) MR image with beam signature at 32 nA and 207 MeV. Orange dotted lines indicate the 10 central profiles used for range determination (b) Mean profiles over the 10 central lines, for 200 MeV, 207 MeV and 215 MeV acquired at 32 nA and three no beam references. Dotted blue line indicates grey value level (600) used for range difference estimation.

**Proton beam energy dependency of the MRI signature**

Figure 6.4 shows the Angio TOF MR images acquired during simultaneous proton beam irradiation at a constant beam current of 32 nA for different beam energies (and ranges). The proton beam is visible as a hypo-intense signature, that is beam-energy dependent and closely resembles a planar longitudinal proton beam dose distribution. Range differences between the three beam energies studied were determined using an arbitrarily chosen threshold level of 600 grey values on the central horizontal profiles determined from the average of 10 central horizontal line profiles through the image, see Figure 6.5. Similarly, absolute range, $R_{\mathrm{MR}}$ was determined as the profile shift compared to the no-beam references. The resulting apparent absolute and relative beam ranges are given in Table 6.3. Differences to expected residual ranges, as calculated in Section 6.1.3 were within 4 mm, with a systematic trend to overestimate the range in MR images. However, relative range differences between beam energies agree to predictions within 1 mm.

**Beam current dependency**

Figure 6.6 shows the dependency on the beam current of the beam induced MRI signatures for a variation of the beam current from 0 nA (reference) up to 64 nA. With increasing beam current the area of the signal void increases. For the lower currents (8 nA and 16 nA) only
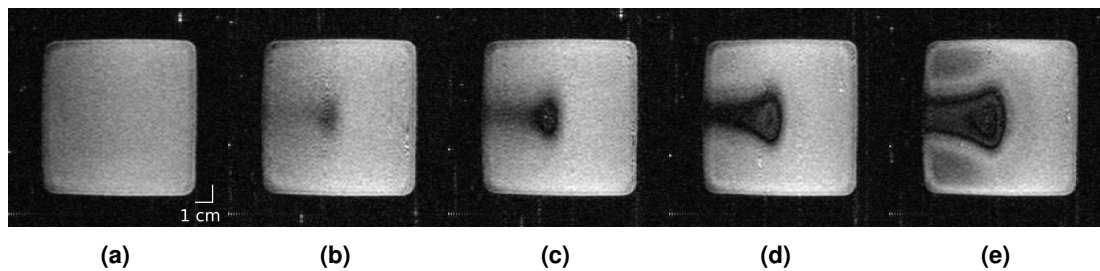
**Figure 6.6:** Angio TOF MR images showing the beam current dependency of the signature. (a)-(e) were acquired under irradiation using 207 MeV and 0 nA, 8 nA, 16 nA, 32 nA and 64 nA, respectively.

an elliptically shaped area is visible that closely resembles the Bragg peak region. This indicates that a certain dose threshold is necessary to visualize the MRI signature, as the relative dose is expected to be highest in the Bragg peak region. For the highest current (64 nA) the beam signature is surrounded by regions of hypointense signal, potentially due to a flow reflection on the lid of the phantom.

This strong beam current dependency shows why absolute proton range determination in the Angio TOF MR images is challenging. The apparent beam range differs markably with the used beam current, with a maximum difference of 7 mm between the two extreme cases studied (8 nA and 64 nA).

**Dose rate and convection velocity**

The measured dose rates for the beam currents of 8 nA, 16 nA, 32 nA and 64 nA were 660 Gy/min, 1300 Gy/min, 2550 Gy/min and 5100 Gy/min, respectively. To approximate the total dose delivered, an effective irradiation time is required to scale the dose rate. However, it is not inherently clear which effect the irradiation during imaging has on the images themselves, thus for the effective irradiation time two cases have to be considered: (1) only accounting for the 15 s of pre-imaging irradiation and (2) including the 3 s of image acquisition. To include this uncertainty into the calculation, the effective time was chosen to be

**Table 6.3:** Comparison of estimated residual proton beam ranges by MR imaging, $R_{\mathrm{MR}}$, and prediction, $R_{\mathrm{res}}$. $\Delta R_{\mathrm{MR}}$ and $\Delta R_{\mathrm{res}}$ indicate the relative range difference to the previous (lower) energy.

| Beam energy / MeV | $R_{\mathrm{MR}}$ / mm | $R_{\mathrm{res}}$ / mm | $\Delta R_{\mathrm{MR}}$ / mm | $\Delta R_{\mathrm{res}}$ / mm |
|---|---|---|---|---|
| 200 | $32.3 \pm 0.5$ | $28.5 \pm 2.0$ | | |
| 207 | $48.3 \pm 0.5$ | $44.8 \pm 2.0$ | $16.0 \pm 0.5$ | $16.3 \pm 2.0$ |
| 215 | $66.2 \pm 0.5$ | $63.4 \pm 2.0$ | $17.9 \pm 0.5$ | $18.6 \pm 2.0$ |

16.5 s ± 1.5 s leading to effective doses of (180 ± 20) Gy, (360 ± 30) Gy, (700 ± 60) Gy and (1400 ± 130) Gy, for beam currents of 8 nA, 16 nA, 32 nA and 64 nA, respectively. The temperature of the water $T_0$ in the phantom before irradiation was measured to be 29 °C. This results in a density of $\rho(T_0)$ = 0.995944 g/cm$^3$ (Rumble, 2020) and a dynamic viscosity of $\mu(T_0)$ = 0.814 mPa s (Cooper, 2008). The radius of the sphere in the viscometer model (see page 64) was approximated to be half of the FWHM of the beam profile at phantom entry, which results in $R$ = 11 mm. This, however, is only a valid assumption for the beam entry region, as the dose profile widens closer to the Bragg peak region. The estimated beam-induced flow velocities were in the range of 17 cm/min to 130 cm/min, for beam currents between 8 nA and 64 nA (Table 6.4). Note here that this calculation can only be understood as an order-of-magnitude estimation, as a number of large uncertainties could strongly influence the result. The main contributions are (with an estimate of the relative effect in brackets): Firstly the applied dose is influenced both by the effective irradiation time (≈10 %) and the increase in dose towards the Bragg peak (peak-to-plateau ratio can be up to +400 %). Secondly, the radius of the beam increases with depth in the phantom (up to ≈ +100 %). Thirdly, the water temperature before irradiation is subject to an uncertainty on the order of ±1 °C, however its effect on both the density and viscosity is small (< 5 %). Lastly, the Stokes' law viscometer model itself is a further limitation, as the water is not confined to a sphere, and the heated volume is closer to a cylinder then a sphere.

## 6.2.2 Vertical flow restriction and flow inhibition

Figure 6.7a shows a reference no-beam Angio TOF MR image using the flow restriction inset in the phantom. The MRI signal is clearly present in the water filled capillaries, whereas the PMMA inset itself produces signal voids. Images acquired during irradiation with beam energies of 200 MeV, 207 MeV and 215 MeV (at constant beam current of 64 nA) show the same energy-dependent signal void as in the baseline experiment. This is shown in Figure

**Table 6.4:** Calculated flow velocity $v_\mathrm{flow}$ as a function of proton beam current.

| proton beam current / nA | estimated flow velocity $v_\mathrm{flow}$ / cm/min |
|---|---|
| 8 | 17 |
| 16 | 33 |
| 32 | 65 |
| 64 | 130 |
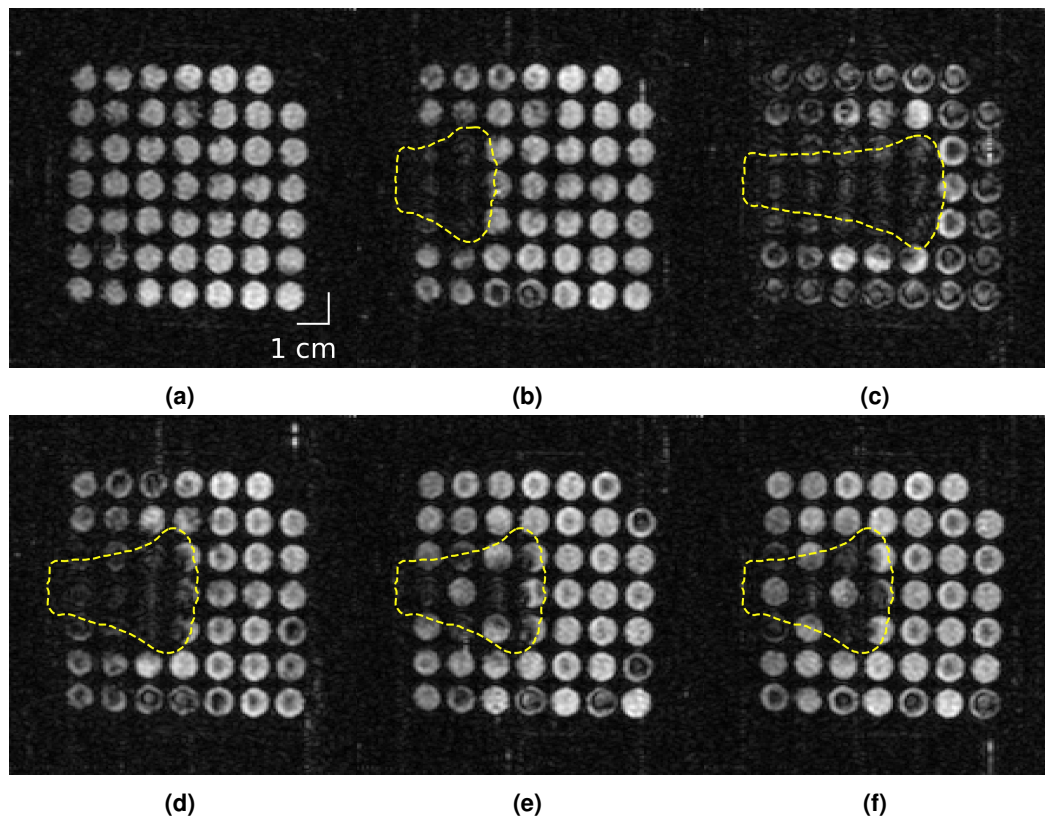
**Figure 6.7:** Angio TOF MR images of the vertical capillary flow restriction experiment. (a) Reference no-beam image, (b) and (c) image acquired with irradiation using 200 MeV and 215 MeV beams, respectively. Images acquired during irradiation using 207 MeV, without (d), and with flow inhibition plates B (e) and A (f), respectively. Yellow dotted contours denote the beam contour from the baseline experiments. All images (b-f) were acquired using a beam current of 64 nA.

6.7(b-d) with overlaid yellow contours adapted from the baseline experiment. The addition of either of the two flow inhibition plates A or B leads to an increase in MRI signal in all the closed capillaries that are within the area of dose-deposition (inside the yellow contour), resulting in a signal intensity that is identical to no-beam references and/or regions without the beam (outside the yellow contour). Figure 6.7(e-f) shows the results for 207 MeV: All selectively closed capillaries appear bright, whereas in all open capillaries the MRI signal is hypointense. The same qualitative results were observed for the other two proton beam energies studied (results not shown here).

**Figure 6.8:** Angio TOF MR images showing the effect of external flow. Images (a)-(d) were acquired with flow settings of 0, 0.35, 0.5 and 2, respectively. The red circles mark the tube, in which the flow direction is upwards.
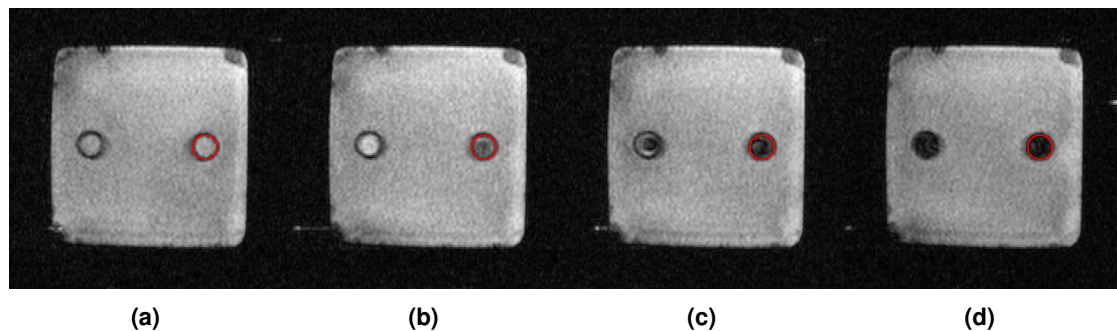
### 6.2.3 MRI signal loss by external flow

Figures 6.8(a-d) show the Angio TOF MR images acquired during externally introduced flow condition in the u-shaped tube, for flow velocity rate settings of 0, 0.35, 0.5 and 2, respectively. The red circle in the images marks the part of the tube, in which the flow direction is upwards. This flow direction corresponds to the beam induced flow. For all images with the pump running, i.e. with the flow present, a reduction in the MRI signal was observed for upwards directed flow. This signal reduction increased with increasing flow setting, i.e. flow velocity. For the flow rate of 2 and all higher pump settings, the signal inside both tubes completely vanished. For the downwards directed flow, a similar effect is visible, the signal inside the tube reduces with increasing flow rate for all flow rates above 0.5. However, for the lowest flow rate setting of 0.35 (Figure 6.8b), the signal in the downward flow tube is slightly increased as compared to the non-moving water signal in the phantom. With the pre-saturation slab directly below the imaging slice and the pre-saturation pulse not being a perfect rectangular function in the frequency domain, the signal in the non-moving water is slightly reduced as compared to an identical sequence without pre-saturation. Thus, the inflowing fresh (non-pre-saturated) water flowing into the slice, therefore shows a slightly increased signal.

The experiment was repeated with the flow direction reversed and qualitatively similar results were observed.

## 6.3 Discussion

For the first time, an Angio TOF MRI sequence was utilized to visualize a proton beam in images of a water filled phantom. The beam induced change in MRI signal was demonstrated to be caused by beam-induced flow effects. The Angio TOF MRI sequence reproduces previous findings, a stopping proton beam is clearly visible as a hypo-intense signature in images of a water filled phantom. The signature closely resembles the range and shape of a planar dose distribution of the used pencil beam. Furthermore, the effect was shown to be both proton beam current- and energy-dependent.

The main research question, whether the beam induced MRI signature effect is triggered by convection was studied by two independent experiments. Both the flow restriction and inhibition in the phantom as well as the externally introduced flow without irradiation have shown that a vertical flow, perpendicular to the MR imaging plane, results in a local loss of MRI signal. During irradiation, the induced flow in the capillaries caused the MRI signal to vanish in only those capillaries that were open (i.e. had no flow inhibition), whereas for all selectively closed capillaries within the irradiated volume, no reduction in MRI signal was observed. This demonstrates that the inhibition of vertical flow prevents the beam induced signature effect and therefore clearly shows that beam induced convection is highly likely to be the underlying mechanism that explains the observed beam signature effect.

The second independent experiment with the externally introduced flow, demonstrates the same effect. It shows a loss of MRI signal for water flowing into the imaging plane. This further supports the convection hypothesis, even though some details of the findings might require further investigation. The main point here is that the experiment clearly showed that not only the upward flowing water shows a reduced MRI signal but also the downward flow. This indicates that the pre-saturation of the spins can not be the solitary reason for signal loss. Another possible mechanism could be flow induced signal de-phasing (Urchuk & Plewes, 1992), although this effect is primarily known to occur for in-plane flow along the read-out gradient (Axel, 1984).

Furthermore, turbulent flow is known to cause severe MRI signal loss (Jou, 2002), however Reynolds numbers in the performed experiment are on the order of 1 to 100 in the u-shaped tube and hence turbulent flow can be excluded. Furthermore, it is noteworthy that the downward flow required a higher flow rate compared to the upward flow to reach the same signal loss. This can be interpreted as a superposition of two different effects

both leading to signal loss, but at different flow velocities. To understand the exact mechanism behind the observed signal loss, further investigations are important, but were beyond the scope of this study. Regarding the flow velocities in the two experiments, the predicted velocities in the irradiation experiment were about an order of magnitude higher then the velocities required for external flow to produce signal loss. Here, however, as presented on page 70, the uncertainty of the estimated beam induced velocity is at least as high or even higher then the difference in velocities between the two experiments. It is therefore necessary to reduce these uncertainties in future experiments and potentially include a velocity encoding MRI sequence, to experimentally verify the flow velocity in the water phantom. This should further be supported by a simulation of the flow condition in the phantom, which uses a measured proton dose deposition as input for the spatial distribution of temperature change in the water and yields a complete 3D velocity distribution.

Comparing the findings of this chapter to the literature, reference shall be given to a recent publication (Oglesby et al., 2021) which investigated a temperature induced MRI artefact (i.e., a local signal loss) in warm (37 °C) liquid water filled phantoms, which was shown to be caused by convection currents. Similarly to the experiments performed in this chapter, the authors could clearly demonstrate that a water flow perpendicular to a horizontal imaging plane results in a local loss of MRI signal. Moreover, the flow velocities determined by their simulation were on the order of 1 mm/s to 10 mm/s, which is the same order of magnitude as the calculated flow velocities caused by proton beam irradiation in this chapter (see Table 6.4). This again shows, that two different mechanisms of signal loss are present in both experiments performed in this chapter. Firstly, the pre-saturated spins flowing into the imaging plane and secondly, an MR signal loss that is directly associated to the water flow. Both of these processes require certain threshold velocities in order to be visible in the acquired images. This was also visible in the baseline experiment, which highlighted that while relative range differences determined in the MR images between different proton beam energies (under constant beam current) could very accurately be matched to predictions, the current method is subject to a strong beam current-dependency (and therefore flow velocity dependency), as for lower beam currents, only the Bragg peak region, i.e. the region of expected highest dose (or flow velocity), exhibits the beam induced signal void. This again suggests that the effect requires a dose or rather dose-rate threshold, which can be understood as a flow velocity threshold, in order to visualize the beam in the Angio TOF MR images. While this shows, that further investigations are necessary to fully unravel this

velocity threshold, it also suggests that under constant dose-rate conditions, the method presented in this chapter holds a promising potential for MRI-based proton beam range determination and beam localization. Especially in the context of MRI integrated proton therapy, a reliable means to co-localize the MRI and proton beam coordinate systems is currently missing and absolutely mandatory when looking towards a clinical application of an MRiPT system. While this study was performed using a static proton beam, it is expected that the results, i.e. the possibility to visualize and therefore localize the proton beam, are directly transferable to an actively scanned proton beam.

In conclusion, the experiments performed demonstrate that the convection hypothesis is able to explain the observed phenomena. Beam-induced convection thus shall be considered as a valid explanation for the beam induced effects visible in the MR images. From this, an application of the observed effect to be used in-vivo for proton range verification seems extremely unlikely, as the concept has only been demonstrated in liquids. Future studies aiming for MRI-based in-vivo proton range verification shall thus concentrate on different physical or chemical effects that offer potential to detect the proton beam in-vivo. However, for co-localization of the proton beam and MRI coordinate system in a future hybrid MRiPT system, the observed proton beam signature offers great potential.

# 7 General discussion and future perspectives

In this chapter, the central aspects investigated in this thesis are discussed in the context of the general development of MRiPT. Resulting implications and research questions generated by the findings of this work are presented and perspectives for future studies are given.

## 7.1 General discussion

### 7.1.1 Magnetometry of the in-beam MRI system

The standard procedure for diagnostic MRI systems includes a magnetic survey at the potential installation site prior to the installation of the system to assess the environmental magnetic field conditions and identify potential sources of interference that might impact on the MR image quality (Jackson et al., 2010). The motivation is that advanced imaging sequences require very strict $B_0$ field homogeneity and stability constraints. However, for the full integration of an MRI system into an existing PT system, the situation is more challenging, as a variety of different disruptive factors, such as the moving masses of ferromagnetic materials (i.e. the PT gantry in the nearby treatment room) and the environmental magnetic field, which changes with the operation of the proton delivery system, are a unique feature to MRiPT. Prior to this work, the knowledge on the mutual electromagnetic interference between the MRI and PT system was limited to an initial investigation of the effect of the gantry position and rotation on the magnetic field homogeneity of the MRI scanner as well as a first feasibility study showing that the MRI scanner can be shimmed within the static magnetic fringe field of the nearby cyclotron (Schellhammer, 2019). Therefore, a comprehensive magnetic survey was of key importance to identify all sources of interference to evaluate potential workflows for MRiPT in order to assure that the image quality is not negatively affected by the operation of the PT system.

This work has shown (Chapter 3 and 5) that the operation of the three proton beamlines

at the OncoRay facility influences both the central resonance frequency and the magnetic field homogeneity of the $B_0$ field of the in-beam MRI scanner. These results, while giving different values of field perturbation, were qualitatively the same for both positions of the MRI scanner, both initially at the horizontal static beamline, as well as for the position at the horizontal PBS beamline. The magnitude of the change in field homogeneity was very small (i.e. less then 3 ppm) for all studied scenarios and is therefore considered negligible at the current state of development of MRiPT. However, the change in resonance frequency explains the image translations previously observed by Schellhammer (2019) during simultaneous imaging and static proton beam irradiation. A detailed analysis of the image quality of the in-beam MRI scanner at the static beamline had revealed that during static proton beam irradiation mainly two effects were seen: Firstly, a minor reduction in the SNR and secondly a sequence-depend image shift in frequency-encoding direction (Gantz et al., 2021; Schellhammer, 2019). As discussed in detail in Gantz et al. (2021), the reduction in SNR can be understood by secondary radiation-induced currents in the receiver coil (Burke et al., 2010; Burke et al., 2012). Regarding the observed shifts in frequency-encoding direction, this work has shown, that the magnitude of these image translations corresponds to the measured change in resonance frequency. To reduce the effects of magnetic field interactions on the MR image quality, firstly, magnet shimming accounts for all sources of static environmental magnetic fields, as shown by Schellhammer (2019) for the cyclotron and secondly, pre-scan frequency calibration is necessary to account for the measured changes in $B_0$ field due to the operation of the beamlines. This could only become an issue for future compact proton therapy units, with the cyclotron closer to the treatment isocenter, however even then, dedicated magnetic shielding and magnet shimming should be able to account for the field gradient. Additionally, the observed temperature-induced $B_0$ field drift is a limiting factor for the field stability of the permanent-magnet-based MRI scanner used in this study. Although it was beyond the scope of this thesis to investigate the best design of a future clinical MRiPT system, it should be noted that in case it would be based on permanent magnet technology, such a field drift is to be expected and could potentially compromise the versatility of the MRI scanner, as the $B_0$ field drift results in a drift of the image coordinate system and therefore requires constant recalibration. However, it is expected that the $B_0$ field drift can be further reduced by optimizing the thermal insulation and the temperature stability of the magnet's heating system. Furthermore, improving the accuracy of the pre-scan frequency calibration procedure should further reduce the impact

of the drift on the quality and reproducibility of the MRI images.

Regarding the transferability of the results obtained from the current study to a future clinical MRiPT system, it should be noted that the principles will remain the same: the fringe fields of the beam transport and beam scanning magnets of the PT system will continue to interfere with the magnetic field of the MRI scanner due to the close proximity of the two systems and the large extension of the stray fields of the PT magnets, if not magnetically decoupled. Assuming a future in-beam MRI system would be larger than the current system, the fringe field effects could be reduced at the MRI isocenter if it was positioned further away from the beamline. However, as this study has also shown that the operation of a neighboring beamline significantly alters the $B_0$ field, it is expected that this challenge will remain. This finding is independent of the choice of MRI technology and will therefore also be the case for a potential future superconducting magnet system. However, the magnitude of these influences will strongly depend on the specific design of a future system and therefore remain to be studied experimentally in the future.

### 7.1.2 Simultaneous MR imaging and active PBS beam delivery

According to current insights, a future clinical MRiPT system should feature in-beam MR imaging simultaneous to PBS irradiation as the ultimate goal of the integration (Oborn et al., 2017), as it combines the ultra-conformal dose delivery technique with the unprecedented soft-tissue image quality of online real-time MRI in the treatment position. However, as a major result of this thesis, the magnetic fringe fields of the scanning magnets in the PBS beamline were shown, for the first time, to cause severe loss of image quality during simultaneous MR imaging and proton PBS irradiation. From the combination of (1) magnetometry measurements showing the underlying dynamic change in the $B_0$ field, (2) simultaneous MR imaging and irradiation experiments, showing the resulting ghosting artefacts and (3) providing a theory capable to describe and reproduce the observed artefacts and their origin, distortions in the phase information in $k$-space, this thesis has presented a full description and understanding of the effects (Chapter 5).

Therefore, future studies need to focus on potential means to guarantee artefact-free image quality during PBS irradiation. From the results described in this thesis two approaches seem promising and should therefore be investigated. Firstly, magnetic shielding of either the MRI system or the scanning magnets is required to decouple the magnetic fields. Fu-

ture studies should therefore assess the necessary minimal shielding factor to guarantee artefact-free MR image quality and investigate different options to shield either the scanning magnets directly or design a shield surrounding the MRI scanner. Both passive and active shielding solutions should be considered. For passive shielding the geometric design and choice of shielding material are essential aspects to investigate. For an active shielding solution, a three component solution seems necessary: a fast measurement of the $B_0$ field changes and a control system that operates an external shielding coil or potentially the integrated active shim coils of a future in-beam MRI system. Ultimately, the feasibility of active shielding will depend on the speed and accuracy of the field adjustment. Secondly, a correction of the raw data of the images prior to image reconstruction or potentially even online during image acquisition following the theory presented in Chapter 5 seems feasible to achieve artefact-free image quality. For the latter approach, a precise synchronization of the MRI and PT systems and an online, accurate determination of the shift in magnetic resonance frequency to a precision of at least 1 Hz (about 20 nT, compare Section 5.3) would be required. As an alternative, a synchronization of the MRI and PT system, where MR imaging is only performed between energy layers would circumvent the dynamic $B_0$ field changes caused by the fringe field of the horizontal scanning magnet and could therefore yield a temporary solution for artefact-free image quality. However, this approach would not allow real-time imaging, as the time duration to deliver one energy-layer is typically on the order of around one to a few seconds (see Section 2.1.2). Thus, such an approach would significantly reduce the expected benefits of an integrated MRiPT system. Therefore, future studies should investigate the feasibility of the two suggested approaches to achieve a magnetic decoupling of the MRI and PT system for artefact-free MR image quality to determine which of the two methods can be realized.

### 7.1.3 MRI-based proton beam visualization

As one of the biggest challenges for proton therapy, proton beam range uncertainties arise from tissue heterogeneities, organ motion, setup and anatomical variations, dose calculation approximations, and biological considerations. As a result, during treatment planning, on single energy CT images, an uncertainty in the proton beam range of up to 3.5 % plus an additional 1 mm – 3 mm is typically assumed (Paganetti, 2012b). As this adds up to sub-

stantial margins, especially for proton beams of higher energy, a reduction of these margins is expected to further improve the targeting precision and reduce normal tissue side effects. However, typical methods for in-vivo proton range verification, such as prompt gamma imaging lack the ability to simultaneously visualize both the proton beam end-of-range and the patient anatomy (Parodi & Polf, 2018). MR imaging, however, especially in the context of in-beam MRI at the treatment isocenter could potentially offer both of these information simultaneously. Therefore, investigating the feasibility to visualize the proton beam, using MR imaging, seems very appealing. Prior to this work, MRI-based proton beam range verification was reported as either an off-line retrospective in-vivo phenomenon of biological changes in the liver (Yuan et al., 2013), a method of MR-based gel-dosimetry (Bäck, 1998) and as recently shown in an exploratory study by Schellhammer (2019) a direct on-line visualization of the proton beam in MRI images of various liquids. However, the underlying principles of the latter approach have not yet been understood.

This work (Chapter 6) has demonstrated that the previously observed MR-detectable beam effects in liquids are highly likely to be caused by convection. This result deems the approach infeasible for in-vivo MRI-based range verification as it will only be present in liquids. However, as the presented method is capable of simultaneously visualizing an MRI-visible liquid-filled object placed in the MRI scanner and the trajectory and range of a proton beam, it may provide a means for co-localization of the MRI and proton beam coordinate system, reducing otherwise necessary co-registration margins. Furthermore, the novel method may prove itself feasible for routine machine-specific quality assurance to verify the position and range of the beam. Nevertheless, at the current stage of development, the method requires a high beam current and dose and the underling image contrast mechanism is still not fully understood. Therefore, it is expected, that future studies could provide means to reduce the minimal beam current required to initiate the effect, e.g. by further optimizing the utilized MRI pulse sequence.

Additionally, to date the potential for in-vivo MRI-based range verification is not yet fully exploited, as the current method only deploys magnitude images and a full theoretical description of the mechanism of signal loss is currently lacking. Thus, future studies aiming for in-vivo MRI-based range verification should focus on different aspects, such as phase sensitive imaging or changes in tissue relaxation times due to e.g. free radicals or exogenous contrast agents.

## 7.2 Future perspectives for MRiPT

For the future application of MRiPT as a clinical treatment modality, serious additional efforts have to be taken. Recently, Hoffmann et al. (2020) have presented the four main aspects which are essential for the development of an MRiPT system: (1) understanding and solving the electromagnetic interactions between the MRI and PT system, (2) realizing a fast and accurate treatment workflow for MRiPT, which allows online treatment adaptation, patient-specific QA and adaptive replanning of stationary or even moving targets, (3) dose calculation, optimization and delivery taking into account both the complex-shaped magnetic fringe fields and the uniform imaging field of the MRI scanner and (4) MRI only treatment planning, which is necessary for online treatment adaptation. While all of these aspects require further research in order to bring MRiPT towards a clinical implementation, considering all of them is far beyond the scope of this thesis. Therefore, this section will address some technological choices for a future system, mainly related to the aspect of electromagnetic interactions and the findings and advances of knowledge presented in this thesis.

### 7.2.1 Short-term perspectives

As a short- to mid-term perspective, demonstrating a first patient treatment with the existing machine or a similar device seems one of the key milestones to bring MRiPT closer towards a clinical application. For such a first demonstration it could be sufficient to use MR imaging for patient setup verification and for the detection of interfractional anatomy changes, such as tumor swelling. To achieve this, the following aspects have to be realized. Firstly, a geometric accuracy of the MR images of $\leq 2\,\text{mm}$ over the whole FOV has been suggested as a requirement for real-time MRI-guided X-ray radiotherapy (Chandarana et al., 2018). This is rather challenging for conventional MRI systems (including the MRI scanner presented in this thesis) due to the magnetic field inhomogeneity and gradient non-linearities which need to be corrected for in order to assure geometric fidelity of the images which is highly important for treatment accuracy.

The image quality study performed with the MRI scanner used in this thesis at the static beamline (Gantz et al., 2021) did not include a sophisticated geometric distortion analysis or geometric distortion correction, thus this is required in a future study. Secondly, future

studies have to investigate how the changes in resonance frequency due to the operation of the PT system, especially the beamline and scanning magnets, can be accounted for. Potential strategies to circumvent the change in $B_0$ caused by the fringe fields of the PT system include, but are not limited to, magnetically decoupling the MRI scanner from the environment or potentially a positional compensation using e.g. a stationary MRI visible frame or restricting the use of the MRI scanner to only intermittent operation with the PT irradiation. While the latter may be a solution for a first-in-human treatment, as e.g. imaging directly before and after irradiation seems sufficient, the development of a workflow where all beamlines are not energized for an extended period of time (likely 5-20 minutes) in which MR images are acquired is necessary and will severely prolong treatment times. Therefore, realizing one of the other strategies described above seems preferable especially when looking further into the future where online imaging is the ultimate goal of the MRI and PT integration. Thirdly, beam commissioning of the combined MRiPT system and treatment planning for protons in realistic MRI fields are two additional important aspects which have to be adapted from clinical standard-of-practice to incorporate the additional challenges that MRiPT upholds. Both of these topics go beyond the scope of this thesis and require substantial future studies, as to date only conceptional knowledge and in-silico studies (Burigo & Oborn, 2019) are available. However no ready-to-use treatment planning system accounting for realistic, inhomogeneous magnetic fields and complex irradiation fields exists so far.

### 7.2.2 Long-term perspectives

On a longer perspective, real-time imaging, which requires a solution for artefact-free MR imaging simultaneously to proton beam delivery has to be realized, as described above preferably by magnetically decoupling the MRI and PT systems. Additionally, several system design choices for a clinical machine will have to be answered and are discussed in the following: (1) the choice of MRI field strength, opting between a low-field and high-field MRI scanner, with their respective benefits and drawbacks, (2) the consideration of active versus passive beam delivery for a future clinical MRiPT system and finally (3) additional challenges which will be introduced by a potential integration of an MRI scanner into a gantry based PT system.

**Optimal MRI field strength for MRiPT**    The choice for a low-field or mid-field MRI system versus a high-field MRI system should be briefly discussed in the following.

With the development of low-field and mid-field MRI scanners, that utilize modern high-end gradient systems, real-time imaging has become available at field strength of 0.35 T and 0.55 T using bSSFP pulse sequences, resulting in an image quality comparable to high field (e.g. 1.5 T diagnostic) MRI systems (Bandettini et al., 2020; Rashid et al., 2018). Furthermore, dosimetric effects, such as e.g. beam deflection and electron return effect (Lühr et al., 2019) are more pronounced at higher $B_0$ field strength, which could complicate treatment planning. Therefore, there no longer seems to be a convincing argument that would require a high-field MRI solution in order to realize real-time imaging in an integrated MRiPT setup. In addition, while in general SNR is scaling with $B_0$ field strength (Cao et al., 2014), contrast-to-noise ratio (CNR) is the more valuable parameter for tumor delineation, patient position verification and tumor tracking. CNR is not directly correlated with $B_0$ but is dependent on the body site and can even be increased at lower field strength as compared to higher fields for certain sequences, such as the bSSFP pulse sequence, which is a promising candidate for real-time imaging at lower fields (Wachowicz et al., 2016).

Furthermore, many (but not all) low-field MRI systems are based on an open system design which features a better accessibility for objects or patients placed in the isocenter of the MRI scanner, as an open system offers at least one more free axis for beam delivery and patient setup as compared to a closed-bore design, which is the standard for high-field MRI scanners. For the integration of MRI and PT at least one free axis is required for the proton beam to enter the treatment isocenter, as the concept of irradiating through the cryostat, as is done for one of the clinical MRI-Linac systems in photon therapy (Friedel et al., 2019), would severely complicate the treatment planning with protons and therefore does not seem feasible. Therefore, either an open system, a double donut (Mislow et al., 2009) or split-bore design (Keall et al., 2014) or a bipolar system (Fallone, 2014) seems necessary. Combining all of these considerations, a low- to mid-field MRI system with one of the above named semi or fully open designs seems most promising.

**Beam delivery for MRiPT: Passive scattering or active scanning technique?**    Independent from the aspect of MRI integration, PBS is considered the state-of-the-art technique providing the better target dose conformality over what can be achieved with PS (Chuong et al., 2018). However, solid clinical evidence that this leads to a reduction of

normal-tissue toxicity is still lacking in the literature for most PT indications. The main physical benefit of PBS is the increased tumor dose conformality and therefore lower integral dose deposited in healthy tissue surrounding the tumor. For stationary targets, the above argument in favor of PBS is convincing, however when motion comes into consideration the interplay effect, which might degrade the applied target dose homogeneity, has to be considered (Meijers et al., 2020). Nevertheless, PS generally requires more treatment time due to low beam efficiencies caused by the scattering and collimation system (Paganetti, 2017) and further requires patient specific devices (i.e. apertures or compensators) which increase the cost of a treatment. In addition, PBS increases the flexibility in the treatment delivery, reduces patient exposure to secondary radiation (Paganetti, 2012a) and allows for dose weighting of each individual spot, enabling intensity modulated proton therapy (Langen & Mehta, 2015). Thus, an increasing number of PT centers change towards PBS delivery.

Regarding the integration of MR imaging and PT, for active scanning, the compensation of beam deflection due to the presence of the magnetic fields of the MRI scanner is well studied and seems straightforward (Burigo & Oborn, 2019; Padilla-Cabal et al., 2019). For each individual beam, the direction and energy has to be adapted to account for the deflection caused by the magnetic field (Hartman et al., 2015; Padilla-Cabal et al., 2020; Schellhammer & Hoffmann, 2017). For passive scattering however, it remains to be investigated in treatment planning studies, whether the beam deflections of a complete radiation field can be accounted for without severe compromises to plan quality. This seems complex, due to the multi-energetic beam and the resulting energy dependent beam deflection. Nevertheless, a comprehensive study of its feasibility is still missing to date and seems necessary, especially if future studies were to show that the magnetic decoupling of the PBS and MRI system for artefact-free imaging during PBS irradiation can not be technically achieved. In this case PS could serve as an alternative, which does not require the use of scanning magnets and therefore circumvents the dynamic electromagnetic interactions between the PBS scanning magnets and the MRI scanner.

However, as stated before, modern PT centers heavily turn towards PBS for the standard beam application. Thus, it remains questionable if PT centers would return to PS delivery solely for MRiPT.

**Gantry integration**   Another step towards a future in-beam MRiPT system is to consider the integration of an MRI scanner in a treatment room having an isocentric rotating gantry. Here, while most of the results obtained in the current study seem transferable, in addition, the influence of the, depending on the gantry design, one or more dipole bending magnets mounted on the gantry are expected to have a severe effect on the $B_0$ field and homogeneity. Modern superconducting bending magnets, despite already being actively shielded typically still have magnetic fringe fields of up to 0.5 mT at the treatment isocenter (Calzolaio et al., 2016) and thus add a dependency on the gantry angle. To put this into perspective, within this thesis, the maximum change in $B_0$ measured during operation of the horizontal scanning magnets was 5.5 µT, thus the effect of the fringe field of the bending magnet is expected to be much larger. As a result, additional active shimming coils in the MRI scanner may be necessary to adjust the $B_0$ field and homogeneity after each gantry rotation and potentially even for each proton energy setting. Furthermore, in the light of a gantry integration, the study performed here can be compared to the case of downstream scanning magnets, i.e., with the scanning magnets downstream of the bending magnets, close to the beam isocenter. The alternative, upstream scanning, where the scanning magnets are positioned further upstream the proton beamline, typically before the last dipole magnet, could increase the distance between the scanning magnets and the MRI scanner and therefore reduce the magnitude of the effect of the fringe fields of the scanning magnets on the $B_0$ field of the MRI scanner. This would simplify a magnetic shielding approach, as a lower shielding factor would suffice to achieve artefact-free MR image quality. Following from these considerations, computational modeling of a variety of potential designs including all involved magnetic fields seems to be absolutely necessary in order to identify the best possible design of a fully integrated MRI and gantry-based actively scanned PT system. Alternatively, especially if such computer simulations and experimental tests were to show that such an integration is not feasible, a gantry-less system, rotating the patient should be envisaged as well. Here, treatment planning studies are key to assess which tumor sites can be treated without a gantry but e.g. by either roll or yaw rotation of the patient couch. In a retrospective study Yan et al. (2016) have shown that the majority of proton therapy treatment delivered using a gantry, could in fact be realized with a gantry-less system when supported by limited beam bending and patient movements.

## 7.3 Conclusion

In conclusion, this thesis greatly improves the understanding of the origin and magnitude of perturbations of the static magnetic field of the MRI scanner due to the presence of static and dynamic fringe fields of the beamline and scanning magnets of the PT system. The work shows that these interactions result in a severe loss of image quality during simultaneous MR imaging and active proton beam delivery. Combining the knowledge obtained from magnetometry, imaging and theoretical considerations, solid evidence is provided to understand why this loss of image quality is observed for one scanning direction only. Furthermore, this work shows that the current method used for online MRI-based proton beam visualization is caused by buoyancy-driven convection and thus are not transferable to the patient. These results stimulate further research targeting both non-clinical research solutions and the development of a first prototype MRiPT system for clinical use.

# 8 Summary

Proton therapy (PT) is expected to greatly benefit from the integration with magnetic resonance imaging (MRI). This holds true especially for moving tumors, as the combination allows tumor motion tracking and subsequently a gated treatment or real-time treatment adaptation. At the time of starting the research work as described in this thesis, only one research-grade prototype 0.22 T MRiPT (MR integrated proton therapy) system existed at a static horizontal proton research beamline. The technical feasibility of imaging at that beamline has been presented previously (Schellhammer, 2019). However, a detailed magnetometric study of magnetic field interactions between the MRI scanner and all components of the proton therapy facility was missing so far. Furthermore, to bring the concept of MRiPT towards clinical application, active proton beam delivery seems essential (Oborn et al., 2017). Therefore, the aim of this thesis is to exploratively investigate the feasibility of integrating an MRI scanner with an actively scanned proton beam, focussing on the magnetic field interactions between the MRI and PT systems and their effects on MR image quality.

   In the first part of this thesis, a study is described which shows the effects of (1) different positions and rotation of the gantry in the nearby treatment room, (2) the operation of the static proton beamline in the research room, and (3) the operation of the treatment room beamline on the $B_0$ field of the in-beam MRI scanner. While the operation of the gantry was found to have negligible effect on the resonance frequency and magnetic field homogeneity of the in-beam MRI scanner, the operation of the two beamlines was found to result in a beam energy-dependent change in resonance frequency on the order of 0.5 µT (20 Hz). This measured change in resonance frequency results in an apparent shift of the MR images. This effect was observed in a previous image quality study during simultaneous imaging and static irradiation performed with the same setup (Gantz et al., 2021; Schellhammer, 2019). It is therefore mandatory to monitor all beamline activities and synchronize the MR image acquisition with the operation of both beamlines in order to guarantee artefact-free MR images and the correct spatial representation of objects in the MR images. Further-

more, a daily drift of the static magnetic field of the MRI scanner was observed and could be correlated to ambient temperature changes, indicating limitations in the heating and the thermal insulation of the permanent magnet material of the MRI scanner. However, this drift can be accounted for by an optimization of the MR frequency calibration prior to each image acquisition.

The second part of this thesis presents the combination of the in-beam MRI scanner with an actively scanned proton beam at a Pencil Beam Scanning (PBS) beamline. The investigation focusses on the influences of the magnetic fringe fields of the PT system onto the MR image quality. First, the suitability of the beam-stopper is shown. Moreover, the maximum radiation field of the beamline for operation with the MRI scanner at the beamline is theoretically presented and confirmed by radiochromic film measurements. In order to prevent a direct irradiation of the MRI scanner, it is shown that a reduction of the field size in vertical direction to 20 cm is required, while the full 40 cm field size is applicable in horizontal direction. Furthermore, a beam energy-dependent trapezoidal distortion of the rectangular radiation field induced by the $B_0$ field of the MRI scanner is, for the first time, experimentally quantified at the isocenter of the MRI scanner and confirms previously published computer simulation studies (Oborn et al., 2015). Additionally, a previously unknown proton beam spot rotation is observed for spot positions in the outer corners of the radiation field, with rotations relative to the main axis of up to 22°, which requires future studies to understand the observed effect.

Second, the feasibility of simultaneous imaging and dynamic PBS irradiation is investigated, by (1) a magnetometry study and (2) MR image quality experiments during simultaneous PBS irradiation. These measurements reveal that the operation of the horizontal scanning magnet results in a severe loss of image quality in the form of ghosting artefacts along the phase-encoding direction, whereas vertical beam scanning and proton beam energy variation is found to cause no visual degradation of image quality. The origin of the observed ghosting artefacts is unravelled by phase-offsets in the k-space information of the acquired images. A theoretical description of these artefacts is presented, which is capable to explain the experimentally observed image artefacts due to the $B_0$ field perturbations found in the magnetometry study. In order to eliminate the observed artefacts, two concepts for artefact-free imaging during PBS dose delivery are suggested, which include magnetic decoupling of the MRI scanner and PT system, and an online image correction strategy that accounts for the changes in the $B_0$ field caused by the operation of the horizontal

scanning magnet. Future studies are crucial to evaluate the feasibility and effectiveness of these approaches.

The third part of the thesis tests the hypothesis that a proton beam-induced signal change in MR images, which is indicative of effective proton dose delivery in fluid-filled phantom material, is caused by heat-induced convection (Schellhammer, 2019). It is clearly shown that the inhibition of water flow could fully suppress the beam-induced MRI signal loss that was observed in previous experiments. Furthermore, the introduction of an external flow condition using similar flow velocities as expected during proton irradiation produces similar MRI signal losses. The combination of both results suggests that the observed MRI signal loss is most likely caused by convection and is hence most likely not transferable to solid materials and tissues. However, the method holds potential for the coordinate system co-localization of the MRI scanner and PT system, as well as for verification of the proton beam range during machine quality control.

In conclusion, this thesis greatly improves the understanding of the origin and magnitude of perturbations of the static magnetic field of the MRI scanner due to the presence of static and dynamic fringe fields of the beamline and scanning magnets of the PT system. The work shows that these interactions result in a severe loss of image quality during simultaneous MR imaging and active proton beam delivery. Combining the knowledge obtained from magnetometry, imaging and theoretical considerations, solid evidence is provided to understand why this loss of image quality is observed for one scanning direction only. Furthermore, this work shows that the current method used for online MRI-based proton beam visualization is caused by buoyancy-driven convection. These results stimulate further research targeting both non-clinical research solutions and the development of a first prototype MRiPT system for clinical use.

# 9 Zusammenfassung

Es wird erwartet, dass die Protonentherapie (PT) stark von der Integration mit online Magnetresonanztomographie (MRT) Bildgebung profitiert. Dies gilt insbesondere bei sich bewegenden Tumoren, da die Kombination eine Verfolgung der Tumorbewegung und anschließend eine atmungsgetriggerte Bestrahlung oder eine Behandlungsanpassung in Echtzeit ermöglicht. Zu Beginn der Forschungsarbeiten, wie sie in dieser Arbeit beschrieben werden, existierte nur ein forschungsgerechtes 0,22 T MRiPT (MRT integrierte Protonentherapie) System an einer statischen horizontalen Protonenstrahlführung. Die technische Machbarkeit der MRT-Bildgebung an dieser Strahlführung wurde zuvor dargestellt (Schellhammer, 2019). Es fehlte jedoch eine detaillierte magnetometrische Untersuchung der Magnetfeldwechselwirkungen zwischen dem MRT-Gerät und allen Komponenten der Protonentherapieanlage. Um das Konzept der MRiPT in Richtung einer klinischen Anwendung zu bringen, scheint darüber hinaus eine aktive Protonenstrahlführung zwingend notwendig (Oborn et al., 2017). Ziel dieser Arbeit ist es daher, die Machbarkeit der Integration eines MRT-Gerätes mit einem aktiv abtastenden Protonenstrahl explorativ zu untersuchen, wobei der Fokus auf den Magnetfeldwechselwirkungen zwischen dem MRT-Gerät und dem PT-System und deren Auswirkungen auf die MRT-Bildqualität liegt.

Im ersten Teil dieser Arbeit wird eine Studie beschrieben, die die Auswirkungen von (1) verschiedenen Positionen und der Rotation der Gantry im nahe gelegenen Behandlungsraum, (2) dem Betrieb der statischen Protonenstrahlführung im Forschungsraum und (3) dem Betrieb der Strahlführung im Behandlungsraum auf das $B_0$-Feld des in-beam MRT-Gerätes zeigt. Während der Betrieb der Gantry einen vernachlässigbaren Einfluss auf die Resonanzfrequenz und die Magnetfeldhomogenität des in-beam MRT-Gerätes hat, wurde festgestellt, dass der Betrieb der beiden Strahlführungen zu einer strahlenergieabhängigen Änderung der Resonanzfrequenz in der Größenordnung von 0,5 μT (20 Hz) führt. Diese gemessene Änderung der Resonanzfrequenz führt zu einer scheinbaren Verschiebung der MRT-Bilder, die in einer früheren Studie zur Bildqualität bei gleichzeitiger Bildgebung und statischer Bestrahlung mit demselben Aufbau beobachtet wurde (Gantz et al., 2021;

Schellhammer, 2019). Es ist daher zwingend erforderlich, alle Aktivitäten der Strahlführungen zu überwachen und die MRT-Bildaufnahme mit dem Betrieb beider Strahlführungen zu synchronisieren, um artefaktfreie MRT-Bilder und die korrekte räumliche Darstellung der Objekte in den MRT-Bildern zu gewährleisten. Darüber hinaus wurde eine tägliche Änderung des statischen Magnetfeldes des MRT-Gerätes beobachtet, welche mit Änderungen der Umgebungstemperatur korreliert werden konnte, was auf technische Limitierungen bei der Heizung und der thermischen Isolierung des Permanentmagnetmaterials des MRT-Gerätes hinweist. Diese Änderungen können jedoch durch eine Optimierung der MR-Frequenzkalibrierung vor jeder Bildaufnahme berücksichtigt und minimiert werden.

Im zweiten Teil dieser Arbeit wird die Kombination des in-beam MRT-Gerätes mit einem aktiv abgetasteten Protonenstrahl an einer PBS-Strahlführung vorgestellt. Im Mittelpunkt der Untersuchung stehen die Einflüsse der magnetischen Streufelder des PT-Systems auf die MRT-Bildqualität. Dabei wird zunächst die Eignung des Strahlfängers gezeigt und das maximale Strahlungsfeld der Strahlführung für den Betrieb mit dem MRT-Gerät an der Strahlführung theoretisch dargestellt und durch Messungen mit radiochromen Filmen bestätigt. Um eine direkte Bestrahlung des MRT-Gerätes zu verhindern, wurded gezeigt, dass eine Reduzierung der Feldgröße in vertikaler Richtung auf 20 cm erforderlich ist, während in horizontaler Richtung die volle Feldgröße von 40 cm anwendbar ist. Weiterhin wird eine strahlenergieabhängige trapezförmige Verzerrung des rechteckigen Strahlungsfeldes, welche durch das $B_0$-Feld des MRT-Gerätes induziert wird, erstmals experimentell im Isozentrum des MRT-Gerätes quantifiziert. Diese Messungen bestätigen zuvor veröffentlichte Computersimulationsstudien (Oborn et al., 2015). Zusätzlich zeigt sich eine bisher unbekannte Rotation der einzelnen Protonenstrahlen für Strahlpositionen in den äußeren Ecken des Strahlungsfeldes, mit Rotationen relativ zur Hauptachse von bis zu 22°, was zukünftige Studien zum Verständnis des beobachteten Effekts erfordert. Im Weiteren wird die Machbarkeit der gleichzeitigen Bildgebung und dynamischen PBS-Bestrahlung untersucht. Hierzu wurden (1) eine Magnetometriestudie und (2) MRT-Bildqualitätsexperimente während der gleichzeitigen PBS-Bestrahlung durchgeführt. Diese Messergebnisse zeigen, dass der Betrieb des horizontal ablenkenden Magneten zu einem starken Verlust der MRT-Bildqualität in Form von Geisterbild-Artefakten entlang der Phasenkodierungsrichtung führt, wohingegen die vertikale Strahlablenkung und die Variation der Protonenstrahlenergie keine sichtbare Verschlechterung der Bildqualität verursacht. Der Ursprung der beobachteten Geister-Artefakte wird durch Phasenabweichungen in der

k-Raum Information der aufgenommenen Bilder entschlüsselt. Eine theoretische Beschreibung dieser Artefakte wird vorgestellt, die in der Lage ist, die experimentell beobachteten Bildartefakte aufgrund der in der Magnetometriestudie gemessenen $B_0$-Feldstörungen zu erklären. Um die beobachteten Artefakte zu eliminieren, werden zwei Konzepte für eine artefaktfreie Bildgebung während der PBS-Dosisverabreichung vorgeschlagen. Zum einen eine magnetische Entkopplung des MRT-Gerätes und des PT-Systems, zum anderen eine Echtzeit-Bildkorrekturstrategie, welche die durch den Betrieb des horizontalen Ablenkmagneten verursachten Änderungen im $B_0$-Feld berücksichtigt. Zukünftige Studien sind zwingend erforderlich, um die Machbarkeit und Effektivität dieser Ansätze zu evaluieren.

Im dritten Teil der Arbeit wird die Hypothese getestet, dass eine protonenstrahlinduzierte Signaländerung in MRT-Bildern, die auf eine effektive Protonendosisabgabe in flüssigkeitsgefülltem Phantommaterial hinweist, durch wärmeinduzierte Konvektion verursacht wird (Schellhammer, 2019). Die durchgeführten Messungen zeigen eindeutig, dass die Hemmung des Wasserflusses den strahleninduzierten MRT-Signalverlust, der in früheren Experimenten beobachtet wurde, vollständig unterdrücken konnte. Des Weiteren wird gezeigt, dass die Einführung einer externen Strömungsbedingung mit ähnlichen Strömungsgeschwindigkeiten, wie sie während der Protonenbestrahlung erwartet werden, ähnliche Signalverluste in den MRT-Bildern erzeugt. Die Kombination beider Ergebnisse deutet darauf hin, dass der beobachtete MRT-Signalverlust höchstwahrscheinlich durch Konvektion verursacht wird und daher höchstwahrscheinlich nicht auf feste Materialien und Gewebe übertragbar ist. Die vorgestellte Methode birgt jedoch Potenzial für die gleichzeitige Lokalisierung der Koordinatensysteme des MRT-Gerätes und des PT-Systems und für die Verifizierung der Protonenstrahlreichweite während der Qualitätskontrolle eines kombinierten MRiPT Gerätes.

Zusammenfassend ist festzustellen, dass diese Arbeit das Verständnis für den Ursprung und das Ausmaß von Störungen des statischen Magnetfeldes des MRT-Gerätes aufgrund des Vorhandenseins von statischen und dynamischen Streufeldern der Strahlführung und der Ablenkmagnete des PT-Systems erheblich verbessert. Die Arbeit zeigt, dass diese Wechselwirkungen zu einem starken Verlust der Bildqualität bei gleichzeitiger MRT-Bildgebung und aktiver Protonenstrahlabgabe führen. Durch die Kombination der Erkenntnisse aus Magnetometrie, Bildgebung und theoretischen Überlegungen wird ein solider Nachweis erbracht, um zu verstehen, warum dieser Verlust an Bildqualität nur für eine Ablenkrichtung beobachtet wird. Darüber hinaus zeigt diese Arbeit, dass die derzeitige Metho-

de, die für die Echtzeit MRT-basierte Protonenstrahlvisualisierung verwendet wird, durch bestrahlungsinduzierte Konvektion verursacht wird und damit nicht auf den Patienten übertragbar ist. Diese Ergebnisse regen weitere Forschungen an, die sowohl auf Lösungen für die nicht-klinische Forschung als auch auf die Entwicklung eines ersten Prototyps eines MRiPT-Systems für den klinischen Einsatz abzielen.

# Bibliography

Alshaikhi, J., Doolan, P. J., D'Souza, D., Holloway, S. M., Amos, R. A., & Royle, G. (2019). Impact of varying planning parameters on proton pencil beam scanning dose distributions in four commercial treatment planning systems. *Medical Physics*, *46*(3), 1150–1162. https://doi.org/10.1002/mp.13382

American College of Radiology. (2008). *Phantom Test Guidance of Use of the Small MRI Phantom for the MRI Accreditation Program*. https://www.acraccreditation.org/-/media/ACRAccreditation/Documents/MRI/SmallPhantomGuidance.pdf

Axel, L. (1984). Blood flow effects in magnetic resonance imaging. *American Journal of Roentgenology*, *143*(6), 1157–1166. https://doi.org/10.2214/ajr.143.6.1157

Bäck, S. (1998). *Implementation of MRI gel dosimetry in radiation therapy*. Malmö University Hospital Lund University.

Bandettini, W. P., Shanbhag, S. M., Mancini, C., McGuirt, D. R., Kellman, P., Xue, H., Henry, J. L., Lowery, M., Thein, S. L., Chen, M. Y., & Campbell-Washburn, A. E. (2020). A comparison of cine CMR imaging at 0.55 T and 1.5 T. *Journal of Cardiovascular Magnetic Resonance*, *22*(1). https://doi.org/10.1186/s12968-020-00618-y

Barnes, B., Kraywinkel, K., Nowossadeck, E., Schönfeld, I., Starker, A., Wienecke, A., & Wolf, U. (2016). *Berichts zum Krebsgeschehen in Deutschland 2016*. Robert Koch-Institut. https://doi.org/10.17886/RKIPUBL-2016-014

Baumann, M., Krause, M., Overgaard, J., Debus, J., Bentzen, S. M., Daartz, J., Richter, C., Zips, D., & Bortfeld, T. (2016). Radiation oncology in the era of precision medicine. *Nature Reviews Cancer*, *16*(4), 234–249. https://doi.org/10.1038/nrc.2016.18

Bercher, R., Büchli, C., & Zumkeller, L. (2001). *Scientific and Technical Report 2001, Volume VI, Large Research Facilities* (Report). Paul Scherer Institut, Villigen, Switzerland. https://inis.iaea.org/collection/NCLCollectionStore/_Public/33/045/33045328.pdf

Bernstein, M. A., King, K. F., & Zhou, X. J. (2004). *Handbook of MRI pulse sequences*. Elsevier. https://doi.org/10.1016/b978-0-12-092861-3.x5000-6

Blasche, M., & Fischer, D. (2017). *Magnet Homogeneity and Shimming* (Report). Siemens Healthcare GmbH. https://cdn0.scrvt.com/39b415fb07de4d9656c7b516d8e2d907/ 1800000003946047 / b36c69893983 / mreadings _ mr - in - rt_3rd - edition _ magnet - homogeneity-and-shimming_blasche_v2_1800000003946047.pdf

Bloch, F. (1933). Zur Bremsung rasch bewegter Teilchen beim Durchgang durch Materie. *Annalen der Physik*, *408*(3), 285–320. https://doi.org/10.1002/andp.19334080303

Bloch, F. (1946). Nuclear induction. *Physical Review*, *70*(7-8), 460–474. https://doi.org/10. 1103/physrev.70.460

Bortfeld, T. (1997). An analytical approximation of the Bragg curve for therapeutic proton beams. *Medical Physics*, *24*(12), 2024–2033. https://doi.org/10.1118/1.598116

Broche, L. M., Ross, P. J., Davies, G. R., & Lurie, D. J. (2017). Simple algorithm for the correction of MRI image artefacts due to random phase fluctuations. *Magnetic Resonance Imaging*, *44*, 55–59. https://doi.org/10.1016/j.mri.2017.07.023

Burigo, L. N., & Oborn, B. M. (2019). MRI-guided proton therapy planning: Accounting for an inline MRI fringe field. *Physics in Medicine & Biology*, *64*(21), 215015. https: //doi.org/10.1088/1361-6560/ab436a

Burke, B., Fallone, B. G., & Rathee, S. (2010). Radiation induced currents in MRI RF coils: Application to linac/MRI integration. *Physics in Medicine & Biology*, *55*(3), 735–746. https://doi.org/10.1088/0031-9155/55/3/013

Burke, B., Ghila, A., Fallone, B. G., & Rathee, S. (2012). Radiation induced current in the RF coils of integrated linac-MR systems: The effect of buildup and magnetic field. *Medical Physics*, *39*(8), 5004–5014. https://doi.org/10.1118/1.4737097

Butts, K., Riederer, S. J., Ehman, R. L., Thompson, R. M., & Jack, C. R. (1994). Interleaved echo planar imaging on a standard MRI system. *Magnetic Resonance in Medicine*, *31*(1), 67–72. https://doi.org/10.1002/mrm.1910310111

Calzolaio, C., Sanfilippo, S., Calvi, M., Gerbershagen, A., Negrazus, M., Schippers, M., & Seidel, M. (2016). Preliminary Magnetic Design of a Superconducting Dipole for Future Compact Scanning Gantries for Proton Therapy. *IEEE Transactions on Applied Superconductivity*, *26*(3), 1–5. https://doi.org/10.1109/tasc.2016.2524448

Cao, Z., Park, J., Cho, Z.-H., & Collins, C. M. (2014). Numerical evaluation of image homogeneity, signal-to-noise ratio, and specific absorption rate for human brain imaging at 1.5, 3, 7, 10.5, and 14 T in an 8-channel transmit/receive array. *Journal of Magnetic Resonance Imaging*, *41*(5), 1432–1439. https://doi.org/10.1002/jmri.24689

Chandarana, H., Wang, H., Tijssen, R., & Das, I. J. (2018). Emerging role of MRI in radiation therapy. *Journal of Magnetic Resonance Imaging*, *48*(6), 1468–1478. https://doi.org/10.1002/jmri.26271

Chuong, M., Badiyan, S. N., Yam, M., Li, Z., Langen, K., Regine, W., Morris, C., III, J. S., Mehta, M., Huh, S., Rutenberg, M., & Nichols, R. C. (2018). Pencil beam scanning versus passively scattered proton therapy for unresectable pancreatic cancer. *Journal of Gastrointestinal Oncology*, *9*(4), 687–693. https://doi.org/10.21037/jgo.2018.03.14

Cooper, J. R. (2008). *Release on the IAPWS Formulation 2008 for the Viscosity of Ordinary Water Substance* (Report). International Association for the Properties of Water and Steam. http://www.iapws.org/relguide/visc.pdf

Crescentini, M., Marchesi, M., Romani, A., Tartagni, M., & Traverso, P. A. (2017). Bandwidth limits in hall effect-based current sensors. *ACTA IMEKO*, *6*(4), 17. https://doi.org/10.21014/acta_imeko.v6i4.478

Demtröder, W. (2015). *Experimentalphysik 1*. Springer Berlin Heidelberg. https://doi.org/10.1007/978-3-662-46415-1

Durand, E., van de Moortele, P.-F., Pachot-Clouard, M., & Bihan, D. L. (2001). Artifact due to $B_0$ fluctuations in fMRI: Correction using the k-space central line. *Magnetic Resonance in Medicine*, *46*(1), 198–201. https://doi.org/10.1002/mrm.1177

Eilers, P. H. C., & Boelens, H. F. M. (2005). *Baseline correction with asymmetric least squares smoothing* (Report). Leiden University Medical Centre.

Engelsman, M., Lu, H.-M., Herrup, D., Bussiere, M., & Kooy, H. M. (2009). Commissioning a passive-scattering proton therapy nozzle for accurate SOBP delivery. *Medical Physics*, *36*(6), 2172–2180. https://doi.org/10.1118/1.3121489

Engelsman, M., Schwarz, M., & Dong, L. (2013). Physics controversies in proton therapy. *Seminars in Radiation Oncology*, *23*(2), 88–96. https://doi.org/10.1016/j.semradonc.2012.11.003

European Commission. (2020). *Causes of death - standardised death rate by NUTS 2 region of residence*. European Commission. https://ec.europa.eu/eurostat/databrowser/view/hlth_cd_asdr2/default/table?lang=en

Fallone, B. G. (2014). The Rotating Biplanar Linac–Magnetic Resonance Imaging System. *Seminars in Radiation Oncology*, *24*(3), 200–202. https://doi.org/10.1016/j.semradonc.2014.02.011

Farr, J. B., Dessy, F., Wilde, O. D., Bietzer, O., & Schönenberg, D. (2013). Fundamental radiological and geometric performance of two types of proton beam modulated discrete scanning systems. *Medical Physics*, *40*(7), 072101. https://doi.org/10.1118/1.4807643

Faßbender, M., Shubin, Y., Lunev, V., & Qaim, S. (1997). Experimental studies and nuclear model calculations on the formation of radioactive products in interactions of medium energy protons with copper, zinc and brass: Estimation of collimator activation in proton therapy facilities. *Applied Radiation and Isotopes*, *48*(9), 1221–1230. https://doi.org/10.1016/s0969-8043(97)00102-4

Friedel, M., Nachbar, M., Mönnich, D., Dohm, O., & Thorwarth, D. (2019). Development and validation of a 1.5 T MR-Linac full accelerator head and cryostat model for Monte Carlo dose simulations. *Medical Physics*, *46*(11), 5304–5313. https://doi.org/10.1002/mp.13829

Fuchs, H., Moser, P., Gröschl, M., & Georg, D. (2017). Magnetic field effects on particle beams and their implications for dose calculation in MR-guided particle therapy. *Medical Physics*, *44*(3), 1149–1156. https://doi.org/10.1002/mp.12105

Gantz, S., Hietschold, V., & Hoffmann, A. L. (2020). Characterization of magnetic interference and image artefacts during simultaneous in-beam MR imaging and proton pencil beam scanning. *Physics in Medicine & Biology*, *65*(21), 215014. https://doi.org/10.1088/1361-6560/abb16f

Gantz, S., Schellhammer, S. M., & Hoffmann, A. L. (2021). Image performance characterization of an in-beam low-field magnetic resonance imaging system during static proton beam irradiation [accepted for publication: 22-May-2021]. *IEEE Transactions on Radiation and Plasma Medical Sciences*. https://doi.org/10.1109/TRPMS.2021.3085991

Haacke, E. M., Brown, R. W., Thompson, M. R., & Venkatesan, R. (1999). *Magnetic Resonance Imaging: Physical Principles and Sequence Design*. Wiley-Liss. https://doi.org/10.1002/9781118633953

Hartman, J., Kontaxis, C., Bol, G. H., Frank, S. J., Lagendijk, J. J. W., van Vulpen, M., & Raaymakers, B. W. (2015). Dosimetric feasibility of intensity modulated proton therapy in a transverse magnetic field of 1.5 T. *Physics in Medicine & Biology*, *60*(15), 5955–5969. https://doi.org/10.1088/0031-9155/60/15/5955

Hidalgo-Tobon, S. S. (2010). Theory of gradient coil design methods for magnetic resonance imaging. *Concepts in Magnetic Resonance Part A*, *36A*(4), 223–242. https://doi.org/10.1002/cmr.a.20163

Hitachi. (2019). *Neodymium-iron-boron magnets neomax magnetic characteristics* (Report). Hitachi Metals, Ltd. https://www.hitachimetals.com/materials-products/permanent-magnets/documents/Permanent_Magnets.pdf

Hoffmann, A., Oborn, B., Moteabbed, M., Yan, S., Bortfeld, T., Knopf, A., Fuchs, H., Georg, D., Seco, J., Spadea, M. F., Jäkel, O., Kurz, C., & Parodi, K. (2020). MR-guided proton therapy: A review and a preview. *Radiation Oncology*, *15*(1). https://doi.org/10.1186/s13014-020-01571-x

Hofman, M. B. M., Kuijer, J. P. A., de Ridder, J. W., Perk, L. R., & Verdaasdonk, R. M. (2013). Technical Note: Building a combined cyclotron and MRI facility: Implications for interference. *Medical Physics*, *40*(1), 012303. https://doi.org/10.1118/1.4772188

Holthusen, H. (1936). Erfahrungen über die Verträglichkeitsgrenze für Röntgenstrahlen und deren Nutzanwendung zur Verhütung von Schäden. *Strahlentherapie 57:254–269*.

Huang, S. Y., Ren, Z. H., Obruchkov, S., Gong, J., Dykstra, R., & Yu, W. (2018). Portable Low-cost MRI System based on Permanent Magnets/Magnet Arrays.

Ito, Y., Yasuda, K., Ishigami, R., Hatori, S., Okada, O., Ohashi, K., & Tanaka, S. (2001). Magnetic flux loss in rare-earth magnets irradiated with 200 MeV protons. *Nuclear Instruments and Methods in Physics Research Section B: Beam Interactions with Materials and Atoms*, *183*(3-4), 323–328. https://doi.org/10.1016/s0168-583x(01)00725-x

Jackson, E., Bronskill, M., Drost, D., Och, J., Pooley, R., Sobol, W., & Clarke, G. (2010). *Report no. 100 - acceptance testing and quality assurance procedures for magnetic resonance imaging facilities* (Report). The American Association of Physicists in Medicine. https://doi.org/10.37206/101

Jäkel, O. (2009). Medical physics aspects of particle therapy. *Radiation Protection Dosimetry*, *137*(1-2), 156–166. https://doi.org/10.1093/rpd/ncp192

James, S. S., Grassberger, C., & Lu, H.-M. (2018). Considerations when treating lung cancer with passive scatter or active scanning proton therapy. *Translational Lung Cancer Research*, *7*(2), 210–215. https://doi.org/10.21037/tlcr.2018.04.01

Jou, L.-D. (2002). Magnetic Resonance signal loss in turbulent shear flow. *Biomedical Engineering: Applications, Basis and Communications*, *14*(01), 1–11. https://doi.org/10.4015/s1016237202000024

Keall, P. J., Barton, M., & Crozier, S. (2014). The Australian Magnetic Resonance Imaging–Linac Program. *Seminars in Radiation Oncology*, *24*(3), 203–206. https://doi.org/10.1016/j.semradonc.2014.02.015

Keeler, J. K. (2010, May 12). *Understanding NMR Spectroscopy 2nd Edition*. John Wiley & Sons.

Keller, P. (2007). *Technologies for Precision Magnetic Field Mapping* (Report). Metrolab Instruments, Geneva Switzerland. https://www.metrolab.com/wp-content/uploads/2015/07/General_tech_note_Technologies_for_Precision_Magnetic_Field_Mapping.pdf

Keller, P. (2011). NMR magnetometers. *Magnetics Technology International*, p68–71. https://www.metrolab.com/wp-content/uploads/2015/07/PT2025_tech_note_NMR-Magnetometers-published-in-Magnetics-Technology-International.pdf

Kellnberger, S., Assmann, W., Lehrack, S., Reinhardt, S., Thirolf, P., Queirós, D., Sergiadis, G., Dollinger, G., Parodi, K., & Ntziachristos, V. (2016). Ionoacoustic tomography of the proton bragg peak in combination with ultrasound and optoacoustic imaging. *Scientific Reports*, *6*(1). https://doi.org/10.1038/srep29305

Klüter, S. (2019). Technical design and concept of a 0.35 T MR-Linac. *Clinical and Translational Radiation Oncology*, *18*, 98–101. https://doi.org/10.1016/j.ctro.2019.04.007

Knopf, A.-C., & Lomax, A. (2013). In vivo proton range verification: A review. *Physics in Medicine & Biology*, *58*(15), R131–R160. https://doi.org/10.1088/0031-9155/58/15/r131

Kose, K., & Haishi, T. (2011). High resolution NMR imaging using a high field yokeless permanent magnet. *Magnetic Resonance in Medical Sciences*, *10*(3), 159–167. https://doi.org/10.2463/mrms.10.159

Küstner, T., Armanious, K., Yang, J., Yang, B., Schick, F., & Gatidis, S. (2019). Retrospective correction of motion-affected MR images using deep learning frameworks. *Magnetic Resonance in Medicine*, *82*(4), 1527–1540. https://doi.org/10.1002/mrm.27783

Langen, K., & Mehta, M. (2015). Proton beam therapy basics. *Journal of the American College of Radiology*, *12*(11), 1204–1206. https://doi.org/10.1016/j.jacr.2015.08.002

Li, J., Wang, Y., Jiang, Y., Xie, H., & Li, G. (2009). Image correction during large and rapid $B_0$ variations in an open MRI system with permanent magnets using navigator echoes and phase compensation. *Magnetic Resonance Imaging*, *27*(7), 988–993. https://doi.org/10.1016/j.mri.2009.01.022

Lipton, M. L. (2008). *Totally accessible MRI*. Springer New York. https://doi.org/10.1007/978-0-387-48896-7

Lopes, P. C., Bauer, J., Salomon, A., Rinaldi, I., Tabacchini, V., Tessonnier, T., Crespo, P., Parodi, K., & Schaart, D. R. (2016). First in-situ TOF-PET study using digital photon counters for proton range verification. *Physics in Medicine & Biology*, *61*(16), 6203–6230. https://doi.org/10.1088/0031-9155/61/16/6203

Lühr, A., Burigo, L. N., Gantz, S., Schellhammer, S. M., & Hoffmann, A. L. (2019). Proton beam electron return effect: Monte Carlo simulations and experimental verification. *Physics in Medicine & Biology*, *64*(3), 035012. https://doi.org/10.1088/1361-6560/aafab4

Maier, J. K. (1989). *Automatic RF Frequency Adjustment For Magnetic Resonance Scanner* (No. 4,806,866) [US Patent].

Marques, J. P., Simonis, F. F., & Webb, A. G. (2019). Low-field MRI: An MR physics perspective. *Journal of Magnetic Resonance Imaging*, *49*(6), 1528–1542. https://doi.org/10.1002/jmri.26637

McGee, K. P., Felmlee, J. P., Manduca, A., Riederer, S. J., & Ehman, R. L. (2000). Rapid autocorrection using prescan navigator echoes. *Magnetic Resonance in Medicine*, *43*(4), 583–588. https://doi.org/10.1002/(sici)1522-2594(200004)43:4<583::aid-mrm13>3.0.co;2-b

Meijers, A., Knopf, A.-C., Crijns, A. P., Ubbels, J. F., Niezink, A. G., Langendijk, J. A., Wijsman, R., & Both, S. (2020). Evaluation of interplay and organ motion effects by means of 4D dose reconstruction and accumulation. *Radiotherapy and Oncology*, *150*, 268–274. https://doi.org/10.1016/j.radonc.2020.07.055

Mislow, J. M., Golby, A. J., & Black, P. M. (2009). Origins of intraoperative MRI. *Neurosurgery Clinics of North America*, *20*(2), 137–146. https://doi.org/10.1016/j.nec.2009.04.002

Moliere, G. (1947). Theorie der Streuung schneller geladener Teilchen I. Einzelstreuung am abgeschirmten Coulomb-Feld. *Zeitschrift für Naturforschung A*, *2*(3), 133–145. https://doi.org/10.1515/zna-1947-0302

Moteabbed, M., Schuemann, J., & Paganetti, H. (2014). Dosimetric feasibility of real-time MRI-guided proton therapy. *Medical Physics*, *41*(11), 111713. https://doi.org/10.1118/1.4897570

Nayak, K. S., Rivas, P. A., Pauly, J. M., Scott, G. C., Kerr, A. B., Hu, B. S., & Nishimura, D. G. (2001). Real-time black-blood MRI using spatial presaturation. *Journal of Magnetic Resonance Imaging*, *13*(5), 807–812. https://doi.org/10.1002/jmri.1112

Oborn, B. M., Dowdell, S., Metcalfe, P. E., Crozier, S., Guatelli, S., Rosenfeld, A. B., Mohan, R., & Keall, P. J. (2016). MRI guided proton therapy: Pencil beam scanning in an MRI fringe field. *Radiotherapy and Oncology*, *118*, S78–S79. https://doi.org/10.1016/s0167-8140(16)30160-8

Oborn, B. M., Dowdell, S., Metcalfe, P. E., Crozier, S., Mohan, R., & Keall, P. J. (2015). Proton beam deflection in MRI fields: Implications for MRI-guided proton therapy. *Medical Physics*, *42*(5), 2113–2124. https://doi.org/10.1118/1.4916661

Oborn, B. M., Dowdell, S., Metcalfe, P. E., Crozier, S., Mohan, R., & Keall, P. J. (2017). Future of medical physics: Real-time MRI-guided proton therapy. *Medical Physics*, *44*(8), e77–e90. https://doi.org/10.1002/mp.12371

Oborn, B., Gantz, S., Schellhammer, S. M., Lühr, A., van der Kraaij, E., & Hoffmann, A. L. (2020). PTC58-0522: Integrated MRI and proton therapy: Modeling and experiments of pencil beam scanning in an MRI field. *Proceedings to the 58th Annual Conference of the Particle Therapy Cooperative Group (PTCOG58). International Journal of Particle Therapy*, *6*(4), 45–491. https://doi.org/10.14338/ijpt.19-ptcog-6.4

Oglesby, R. T., Lam, W. W., & Stanisz, G. J. (2021). A strategy to prevent a temperature-induced MRI artifact in warm liquid phantoms due to convection currents. *NMR in Biomedicine*. https://doi.org/10.1002/nbm.4494

Padilla-Cabal, F., Fragoso, J. A., Resch, A. F., Georg, D., & Fuchs, H. (2019). Benchmarking a GATE/Geant4 Monte Carlo model for proton beams in magnetic fields. *Medical Physics*, *47*(1), 223–233. https://doi.org/10.1002/mp.13883

Padilla-Cabal, F., Resch, A. F., Georg, D., & Fuchs, H. (2020). Implementation of a dose calculation algorithm based on Monte Carlo simulations for treatment planning towards MRI guided ion beam therapy. *Physica Medica*, *74*, 155–165. https://doi.org/10.1016/j.ejmp.2020.04.027

Paganetti, H. (Ed.). (2011). *Proton Therapy Physics*. Taylor & Francis Inc.

Paganetti, H. (2012a). Assessment of the Risk for Developing a Second Malignancy From Scattered and Secondary Radiation In Radiation Therapy. *Health Physics*, *103*(5), 652–661. https://doi.org/10.1097/hp.0b013e318261113d

Paganetti, H. (2012b). Range uncertainties in proton therapy and the role of Monte Carlo simulations. *Physics in Medicine & Biology*, *57*(11), R99–R117. https://doi.org/10.1088/0031-9155/57/11/r99

Paganetti, H. (2017). *Proton beam therapy*. IOP Publishing. https://iopscience.iop.org/book/978-0-7503-1370-4.pdf

Paganetti, H., & Fakhri, G. E. (2015). Monitoring proton therapy with PET. *The British Journal of Radiology*, *88*(1051), 20150173. https://doi.org/10.1259/bjr.20150173

Parodi, K., & Polf, J. C. (2018). In vivo range verification in particle therapy. *Medical Physics*, *45*(11). https://doi.org/10.1002/mp.12960

PTCOG. (2018). *Particle therapy facilities in operation.* (Report). Particle Therapy Co-Operative Group. https://www.ptcog.ch/index.php

Raaymakers, B. W., Jürgenliemk-Schulz, I. M., Bol, G. H., Glitzner, M., Kotte, A. N. T. J., van Asselen, B., de Boer, J. C. J., Bluemink, J. J., Hackett, S. L., Moerland, M. A., Woodings, S. J., Wolthaus, J. W. H., van Zijp, H. M., Philippens, M. E. P., Tijssen, R., Kok, J. G. M., de Groot-van Breugel, E. N., Kiekebosch, I., Meijers, L. T. C., . . . Lagendijk, J. J. W. (2017). First patients treated with a 1.5 T MRI-Linac: Clinical proof of concept of a high-precision, high-field MRI guided radiotherapy treatment. *Physics in Medicine & Biology*, *62*(23), L41–L50. https://doi.org/10.1088/1361-6560/aa9517

Raaymakers, B. W., Raaijmakers, A. J. E., & Lagendijk, J. J. W. (2008). Feasibility of MRI guided proton therapy: Magnetic field dose effects. *Physics in Medicine & Biology*, *53*(20), 5615–5622. https://doi.org/10.1088/0031-9155/53/20/003

Rashid, S., Han, F., Gao, Y., Sung, K., Cao, M., Yang, Y., & Hu, P. (2018). Cardiac balanced steady-state free precession MRI at 0.35 T: A comparison study with 1.5 T. *Quantitative Imaging in Medicine and Surgery*, *8*(7), 627–636. https://doi.org/10.21037/qims.2018.08.09

Reeder, S. B., & McVeigh, E. R. (1994). The effect of high performance gradients on fast gradient echo imaging. *Magnetic Resonance in Medicine*, *32*(5), 612–621. https://doi.org/10.1002/mrm.1910320510

Richter, C., Pausch, G., Barczyk, S., Priegnitz, M., Keitz, I., Thiele, J., Smeets, J., Stappen, F. V., Bombelli, L., Fiorini, C., Hotoiu, L., Perali, I., Prieels, D., Enghardt, W., & Baumann, M. (2016). First clinical application of a prompt gamma based in vivo proton range verification system. *Radiotherapy and Oncology*, *118*(2), 232–237. https://doi.org/10.1016/j.radonc.2016.01.004

Rumble, J. R. (Ed.). (2020). *CRC Handbook of Chemistry and Physics*. Taylor & Francis Ltd.

Saloner, D. (1995). The AAPM/RSNA physics tutorial for residents. an introduction to MR angiography. *RadioGraphics*, *15*(2), 453–465. https://doi.org/10.1148/radiographics.15.2.7761648

Sarosiek, C., DeJongh, E. A., Coutrakon, G., DeJongh, D. F., Duffin, K. L., Karonis, N. T., Ordoñez, C. E., Pankuch, M., Rykalin, V., Winans, J. R., & Welsh, J. S. (2021). Analysis of characteristics of images acquired with a prototype clinical proton radiography system. *Medical Physics*, *48*(5), 2271–2278. https://doi.org/10.1002/mp.14801

Scheffler, K., & Lehnhardt, S. (2003). Principles and applications of balanced SSFP techniques. *European Radiology*, *13*(11), 2409–2418. https://doi.org/10.1007/s00330-003-1957-x

Schellhammer, S. (2019). *Technical feasibility of MR-integrated proton therapy: Beam deflection and image quality* [Dissertation, Technische Universität Dresden]. Qucosa. https://nbn-resolving.org/urn:nbn:de:bsz:14-qucosa2-341326

Schellhammer, S. M., Gantz, S., Lühr, A., Oborn, B. M., Bussmann, M., & Hoffmann, A. L. (2018a). Technical Note: Experimental verification of magnetic field-induced beam deflection and Bragg peak displacement for MR-integrated proton therapy. *Medical Physics*, *45*(7), 3429–3434. https://doi.org/10.1002/mp.12961

Schellhammer, S. M., & Hoffmann, A. L. (2017). Prediction and compensation of magnetic beam deflection in MR-integrated proton therapy: A method optimized regarding accuracy, versatility and speed. *Physics in Medicine & Biology*, *62*(4), 1548–1564. https://doi.org/10.1088/1361-6560/62/4/1548

Schellhammer, S. M., Hoffmann, A. L., Gantz, S., Smeets, J., van der Kraaij, E., Quets, S., Pieck, S., Karsch, L., & Pawelke, J. (2018b). Integrating a low-field open MR scanner with a static proton research beam line: Proof of concept. *Physics in Medicine & Biology*, *63*(23), 23LT01. https://doi.org/10.1088/1361-6560/aaece8

Schippers, J. M. (2009). Beam delivery systems for particle radiation therapy: Current status and recent developments. *Reviews of Accelerator Science and Technology*, *02*(01), 179–200. https://doi.org/10.1142/s1793626809000211

Schippers, J. M., & Lomax, A. J. (2011). Emerging technologies in proton therapy. *Acta Oncologica*, *50*(6), 838–850. https://doi.org/10.3109/0284186x.2011.582513

Seco, J., Robertson, D., Trofimov, A., & Paganetti, H. (2009). Breathing interplay effects during proton beam scanning: Simulation and statistical analysis. *Physics in Medicine & Biology*, *54*(14), N283–N294. https://doi.org/10.1088/0031-9155/54/14/n01

Seltzer, S., & Bergstrom, P. (1993). *Stopping-Powers and Range Tables for Electrons, Protons, and Helium Ions, NIST Standard Reference Database 124*. National Institute of Standards; Technology. https://doi.org/10.18434/T4NC7P

Shen, J., Tryggestad, E., Younkin, J. E., Keole, S. R., Furutani, K. M., Kang, Y., Herman, M. G., & Bues, M. (2017). Technical Note: Using experimentally determined proton spot scanning timing parameters to accurately model beam delivery time. *Medical Physics*, *44*(10), 5081–5088. https://doi.org/10.1002/mp.12504

Stapf, S., & Han, S.-I. (Eds.). (2005). *NMR imaging in chemical engineering*. Wiley. https://doi.org/10.1002/3527607560

Takayanagi, T., Uesaka, T., Nakamura, Y., Unlu, M. B., Kuriyama, Y., Uesugi, T., Ishi, Y., Kudo, N., Kobayashi, M., Umegaki, K., Tomioka, S., & Matsuura, T. (2020). On-line range verification for proton beam therapy using spherical ionoacoustic waves with resonant frequency. *Scientific Reports*, *10*(1). https://doi.org/10.1038/s41598-020-77422-2

Tyler, D., Hudsmith, L., Petersen, S., Francis, J., Weale, P., Neubauer, S., Clarke, K., & Robson, M. (2006). Cardiac cine MR-imaging at 3 T: FLASH vs SSFP. *Journal of Cardiovascular Magnetic Resonance*, *8*(5), 709–715. https://doi.org/10.1080/10976640600723797

Urchuk, S. N., & Plewes, D. B. (1992). Mechanisms of flow-induced signal loss in MR angiography. *Journal of Magnetic Resonance Imaging*, *2*(4), 453–462. https://doi.org/10.1002/jmri.1880020415

Verburg, J. M., & Seco, J. (2014). Proton range verification through prompt gamma-ray spectroscopy. *Physics in Medicine & Biology*, *59*(23), 7089–7106. https://doi.org/10.1088/0031-9155/59/23/7089

Wachowicz, K., Zanche, N. D., Yip, E., Volotovskyy, V., & Fallone, B. G. (2016). CNR considerations for rapid real-time MRI tumor tracking in radiotherapy hybrid devices: Effects of $B_0$ field strength. *Medical Physics*, *43*(8Part1), 4903–4914. https://doi.org/10.1118/1.4959542

Werner, T., Berthold, J., Hueso-González, F., Koegler, T., Petzoldt, J., Roemer, K., Richter, C., Rinscheid, A., Straessner, A., Enghardt, W., & Pausch, G. (2019). Processing of prompt gamma-ray timing data for proton range measurements at a clinical beam delivery. *Physics in Medicine & Biology*, *64*(10), 105023. https://doi.org/10.1088/1361-6560/ab176d

Whelan, B., Kolling, S., Oborn, B. M., & Keall, P. (2018). Passive magnetic shielding in MRI-linac systems. *Physics in Medicine & Biology*, *63*(7), 075008. https://doi.org/10.1088/1361-6560/aab138

Yan, S., Lu, H.-M., Flanz, J., Adams, J., Trofimov, A., & Bortfeld, T. (2016). Reassessment of the Necessity of the Proton Gantry: Analysis of Beam Orientations From 4332 Treatments at the Massachusetts General Hospital Proton Center Over the Past 10 Years. *International Journal of Radiation Oncology, Biology, Physics*, *95*(1), 224–233. https://doi.org/10.1016/j.ijrobp.2015.09.033

Yuan, Y., Andronesi, O. C., Bortfeld, T. R., Richter, C., Wolf, R., Guimaraes, A. R., Hong, T. S., & Seco, J. (2013). Feasibility study of in vivo MRI based dosimetric verification of proton end-of-range for liver cancer patients. *Radiotherapy and Oncology*, *106*(3), 378–382. https://doi.org/10.1016/j.radonc.2013.01.016

Zanche, N. D., Barmet, C., Nordmeyer-Massner, J. A., & Pruessmann, K. P. (2008). NMR probes for measuring magnetic fields and field dynamics in MR systems. *Magnetic Resonance in Medicine*, *60*(1), 176–186. https://doi.org/10.1002/mrm.21624

Zhang, R., & Newhauser, W. (2009). Calculation of water equivalent thickness of materials of arbitrary density, elemental composition and thickness in proton beam irradiation. *Physics in Medicine & Biology*, *54*, 1383–95. https://doi.org/10.1088/0031-9155/54/6/001

Zhuo, J., & Gullapalli, R. P. (2006). MR Artifacts, Safety, and Quality Control. *RadioGraphics*, *26*(1), 275–297. https://doi.org/10.1148/rg.261055134

# Appendix

## A  Results of film measurements at MR isocenter

**Table A.1:** Measured spot coordinates $(X_{Film}, Y_{Film})$, $\sigma$ spot width, tilt angle $\theta$ and peak dose as measured with EBT3 film at the MR isocenter plane.

| Energy | $(X,Y)_{PBSiso}$ | $X_{Film}$ / cm | $Y_{Film}$ / cm | $\sigma_x$ / cm | $\sigma_y$ / cm | $\theta$ / ° | $D_{max}$ / Gy |
|--------|------------------|-----------------|-----------------|-----------------|-----------------|--------------|----------------|
| 70 MeV | | | | | | | |
| | (-20,-10) | -21.5 | -11.2 | 0.84 | 0.90 | 11 | 10.6 |
| | (0,-10) | 2.6 | -11.8 | 0.79 | 0.91 | -2 | 11.5 |
| | (20,-10) | 26.1 | -12.3 | 0.75 | 0.94 | -10 | 11.9 |
| | (-20,0) | -21.5 | 0.2 | 0.87 | 0.93 | 1 | 8.1 |
| | (0,0) | 2.6 | 0.1 | 0.84 | 0.96 | 1 | 8.4 |
| | (20,0) | 26 | 0.0 | 0.81 | 0.99 | 0 | 8.3 |
| | (-20,10) | -21.4 | 11.6 | 0.82 | 0.88 | -10 | 11.6 |
| | (0,10) | 2.6 | 12.0 | 0.79 | 0.90 | 4 | 12 |
| | (20,10) | 26.0 | 12.2 | 0.75 | 0.94 | 10 | 12.2 |
| 125 MeV | | | | | | | |
| | (-20,-10) | -22.7 | -11.3 | 0.52 | 0.58 | 15 | 10.6 |
| | (0,-10) | 1.9 | -11.8 | 0.50 | 0.59 | -1 | 11.5 |
| | (20,-10) | 26.0 | -12.2 | 0.48 | 0.60 | -11 | 11.7 |
| | (-20,0) | -22.7 | 0.1 | 0.55 | 0.60 | 0 | 8.1 |
| | (0,0) | 1.9 | 0.0 | 0.57 | 0.57 | – | 8.3 |
| | (20,0) | 25.9 | -0.0 | 0.52 | 0.64 | 0 | 8.3 |
| | (-20,10) | -22.7 | 11.6 | 0.51 | 0.57 | -14 | 12.1 |
| | (0,10) | 1.9 | 11.9 | 0.54 | 0.53 | – | 12.5 |
| | (20,10) | 25.9 | 12.1 | 0.48 | 0.60 | 11 | 12.1 |
| 220 MeV | | | | | | | |
| | (-20,-10) | -23.2 | -11.3 | 0.30 | 0.34 | 21 | 8.9 |
| | (0,-10) | 1.4 | -11.7 | 0.31 | 0.34 | -5 | 8.3 |
| | (20,-10) | 25.5 | -12.0 | 0.29 | 0.36 | -22 | 8.7 |
| | (-20,0) | -23.1 | 0.3 | 0.31 | 0.34 | -1 | 7 |
| | (0,0) | 1.4 | 0.2 | 0.32 | 0.35 | -1 | 6.6 |
| | (20,0) | 25.5 | 0.0 | 0.31 | 0.36 | 0 | 6.7 |
| | (-20,10) | -23.1 | 11.9 | 0.30 | 0.34 | -22 | 9.8 |
| | (0,10) | 1.4 | 12.0 | 0.31 | 0.34 | 6 | 8.9 |
| | (20,10) | 25.5 | 12.0 | 0.29 | 0.36 | 22 | 9.3 |

# B  Angio TOF MRI pulse sequence parameters

**Table B.2:** MRI sequence parameters for the ANGIO TOF MRI pulse sequence.

| Sequence | ANGIO TOF |
|---|---|
| Field-of-view (FOV) / mm$^2$ | 180×180 |
| Slice Thickness / mm | 10 |
| Echo Time (TE) / ms | 7 |
| Repetition Time (TR) / ms | 19.2 |
| Flip Angle (FA) / ° | 60 |
| Number of Samples | 152 |
| Number of Encodings | 167 |
| Scan Time / s | 3.3 |
| Image Rows x Columns | 334×228 |
| Pixel Spacing / mm | 0.54×0.79 |
| Presaturation Band Width / mm | 40 |

## Acknowledgement

**Erklärungen zur Eröffnung des Promotionsverfahrens**

1. Hiermit versichere ich, dass ich die vorliegende Arbeit ohne unzulässige Hilfe Dritter und ohne Benutzung anderer als der angegebenen Hilfsmittel angefertigt habe; die aus fremden Quellen direkt oder indirekt übernommenen Gedanken sind als solche kenntlich gemacht.

2. Bei der Auswahl und Auswertung des Materials sowie bei der Herstellung des Manuskripts habe ich Unterstützungsleistungen von folgenden Personen erhalten:
   Aswin Hoffmann, Sonja Schellhammer, Volker Hietschold und Layla Riemann.

3. Weitere Personen waren an der geistigen Herstellung der vorliegenden Arbeit nicht beteiligt. Insbesondere habe ich nicht die Hilfe eines kommerziellen Promotionsberaters in Anspruch genommen. Dritte haben von mir weder unmittelbar noch mittelbar geldwerte Leistungen für Arbeiten erhalten, die im Zusammenhang mit dem Inhalt der vorgelegten Dissertation stehen.

4. Die Arbeit wurde bisher weder im Inland noch im Ausland in gleicher oder ähnlicher Form einer anderen Prüfungsbehörde vorgelegt.

5. Die Inhalte dieser Dissertation wurden in folgender Form veröffentlicht:

   - Gantz, S., Hietschold, V. & Hoffmann, A. L. (2020). Characterization of magnetic interference and image artefacts during simultaneous in-beam MR imaging and proton pencil beam scanning. *Physics in Medicine & Biology*, *65*(21), 215014. https://doi.org/10.1088/1361-6560/abb16f

   - Gantz, S., Schellhammer, S. M. & Hoffmann, A. L. (2021). Image performance characterization of an in-beam low-field magnetic resonance imaging system during static proton beam irradiation [accepted for publication: 22-May-2021]. *IEEE Transactions on Radiation and Plasma Medical Sciences*. https://doi.org/10.1109/TRPMS.2021.3085991

6. Ich bestätige, dass es keine zurückliegenden erfolglosen Promotionsverfahren gab.

7. Ich bestätige, dass ich die Promotionsordnung der Medizinischen Fakultät Carl Gustav Carus der Technischen Universität Dresden anerkenne.

8. Ich habe die Zitierrichtlinien für Dissertationen an der Medizinischen Fakultät der Technischen Universität Dresden zur Kenntnis genommen und befolgt.

Dresden, 4. März 2022        _____

**Erklärung über die Einhaltung der gesetzlichen Bestimmungen**

Hiermit bestätige ich die Einhaltung der folgenden aktuellen gesetzlichen Vorgaben im Rahmen meiner Dissertation

☐ ~~das zustimmende Votum der Ethikkommission bei Klinischen Studien, epidemiologischen Untersuchungen mit Personenbezug oder Sachverhalten, die das Medizinproduktegesetz betreffen~~
*nicht zutreffend*

☐ ~~die Einhaltung der Bestimmungen des Tierschutzgesetzes~~
*nicht zutreffend*

☐ ~~die Einhaltung des Gentechnikgesetzes~~
*nicht zutreffend*

☐ die Einhaltung von Datenschutzbestimmungen der Medizinischen Fakultät und des Universitätsklinikums Carl Gustav Carus.

Dresden, 4. März 2022 _____